A MEMS Current Sensor Utilizing NdFeB Magnets

by

John Tatarchuk

A dissertation submitted to the Graduate Faculty of
Auburn University
in partial fulfillment of the
requirements for the Degree of
Doctor of Philosophy

Auburn, Alabama
December 12, 2015

Keywords: MEMS, magnetic MEMS, current sensor, magnetometer

Copyright 2015 by John Tatarchuk

Approved by

Robert Dean, Committee Chair, Associate Professor of Electrical and Computer Engineering
Thomas Baginski, Committee Member, Professor of Electrical and Computer Engineering
Michael Hamilton, Committee Member, Assistant Professor of Electrical and Computer Engineering
Lloyd Riggs, Committee Member, Professor of Electrical and Computer Engineering
W. Robert Ashurst, Dissertation Reader, Associate Professor of Chemical Engineering
George Flowers, Dean of Graduate School, Professor of Mechanical Engineering

Abstract

The need for a current sensor in a 12V-1V DC-DC converter is discussed. Background topics of current sensing in DC-DC converters and magnetic MEMS are discussed. An iterative design process for a MEMS current sensor utilizing permanent magnets is detailed, which results in two working prototype designs and a working final improved design. The final design is a 5.6 mm X 5.6 mm silicon MEMS DC current sensor that utilizes a miniature NdFeB rare earth magnet attached to a silicon platform suspended by a two silicon torsion springs. An external out-of-plane magnetic field, such as that produced by a nearby DC current, will result in a torque being produced due to the interaction of the external field and the NdFeB magnet, creating a deflection of the platform, which can be sensed capacitively. The variable capacitance is converted into a variable frequency by a CMOS relaxation oscillator. Theoretical predictions of device performance are made and verified with ANSYS simulations. Bulk silicon micromachining processes used to fabricate the silicon MEMS components, cap, and mechanical stop are examined, and resolutions to fabrication issues such as etch uniformity are discussed and demonstrated. Microassembly techniques compatible with the high strength NdFeB magnet are developed and presented. Methods for testing the devices are detailed, and test results showing that the devices perform similarly to predictions are given. A discussion of irregularities in the test results is made, and is attributed to non-uniformity in the fabrication process. The device is also tested as a magnetometer and found to compare favorably in terms of sensitivity to commercially-available Hall-effect magnetometers.

Acknowledgments

The author would like to thank his major professor Dr. Robert Dean for his role as a mentor throughout this project. Additionally, the author would like to acknowledge the role of Dr. Wayne Johnson for his role in securing funding for the project, Dr. Thomas Baginski, Dr. Michael Hamilton, and Dr. Lloyd Riggs for their support and roles on the Author's Ph.D. committee, and Dr. Robert Ashurst for his role as dissertation reader. Finally, the Author would like to thank Dr. Colin Stevens, who assisted in initial research on this project and instructed the Author in silicon microfabrication techniques.

Table of Contents

List of Figures

Chapter 1

Introduction and Background

1.1 Purpose

A high efficiency, 12 V to 1 V DC-DC point-of-load (POL) converter was developed at Auburn University as part of an effort in cooperation with the University of Tennessee in Knoxville with the goal of creating a high efficiency power supply for servers/data centers [1–14]. The system requires multiple phases of 12 V - 1 V buck converters in parallel to meet the power requirements. With multiple phases paralleled together, variations in device characteristics will frequently lead to one phase carrying more current than the other. Characterization of the buck converter stages showed that at higher currents, there is an efficiency decrease, so to maximize efficiency it is desirable to ensure that all converter stages are operating at a similar load [7]. This requires that a current-sensing method exist to determine output power of each parallel stage so that switching characteristics can be individually adjusted to balance output power.

Initially, conventional current-sensing methods such as current-sense resistors and Hall effect devices were investigated. These were found to be unacceptable, as in the case of the current sense resistor, power is deliberately dissipated, and both methods require that the current be concentrated into a current sensing element, which leads to higher conduction losses. As a result, another method was sought for sensing current, leading to the development of the device presented in this document, a MEMS DC current sensor utilizing a neodymium-iron-boron (NdFeB) magnet suspended by dual torsion springs. The purpose of this document is to detail the design, fabrication techniques, and performance of this device.

1.2 Current Sensing Methods

A review of current-sensing methods is provided in this section. Current-sensing methods applicable to DC-DC converters can be roughly grouped into three categories: resistive loss, magnetic or inductive sensing, and methods utilizing transistors or transistor properties [15, 16].

1.2.1 Resistive Current Sensing

The simplest method for current sensing is the current-sense resistor, a small-valued precision resistor placed in series with the load. This method has advantages in that it is relatively simple and that it can sense both DC and AC currents, but it requires the use of analog signal conditioning (an op-amp or instrumentation amplifier). Most significantly, at least for the purpose of creating a low-loss DC-DC POL converter, the current sense resistor introduces loss into the system, both through the resistive drop across the resistor itself and through the need to concentrate all the output current into a small area, leading to significant resistive losses in the traces leading up to and following the current-sense resistor.

A second method using resistive losses is reported in [17], where the voltage across the inductor in a DC-DC converter is filtered with a low pass filter. When this is done, the voltage drop due to the equivalent series resistance (ESR) can be extracted. However, the ESR is a function of frequency and highly dependent on the specific inductor used in the converter. Additionally, the low pass filter may require a very low frequency pole- or perhaps be a second order or higher LPF- to suppress the switching frequency and its harmonics enough to easily detect the ESR loss. That said, this method does not introduce any additional significant loss to the circuit [18].

1.2.2 Magnetic-Based Current Sensing Methods

Other current-sensing methods are based on utilizing the magnetic effects of current flow. One example is to use a magnetometer to determine the value of the magnetic field

around a current-carrying trace. Biot-Savart's law, solved for an infinitely long, straight current trace gives a magnetic field (in cylindrical coordinates) of

$$\mathbf{H} = \frac{I}{2\pi r}\hat{\phi} \tag{1.1}$$

where I is a $\hat{z}$-directed current occurring only the z-axis, and r is the radial distance from the line current. Obviously, in a real-world case, the line current would not be infinitely long, but as the magnetometer comes closer and closer to the line current, the relationship between the current and the magnetic field seen by the magnetometer approaches the solution for an infinitely long wire. Regardless, in any configuration of current elements that are varying in a proportionally uniform manner, there will be a linear relationship between the magnetic field produced at any particular point and the value of the current. Thus, once the scalar relationship between the current and the magnetic field value is ascertained, a magnetometer can be used to non-invasively sense the value of the current flow. Obviously, the relationship used to estimate the current from the magnetometer's output will have to be adjusted every time the current trace geometry or magnetometer position changes.

When used as a current sensor, a magnetometer will frequently incorporate ferromagnetic elements to concentrate the magnetic field across the sensor. For surface mount current sensors, this may just be a ferromagnetic strip to serve as a concentrator [19], or the magnetometer may be located in a narrow gap in a ferromagnetic core, as shown in Figure 1.1.

A key benefit of having the measured current flow through the core is that the magnetic field induced in the core becomes insensitive to the position of the wire within the core, as follows from Ampere's Circuital Law,

$$\oint_C H \cdot dL = I_{enc} \tag{1.2}$$

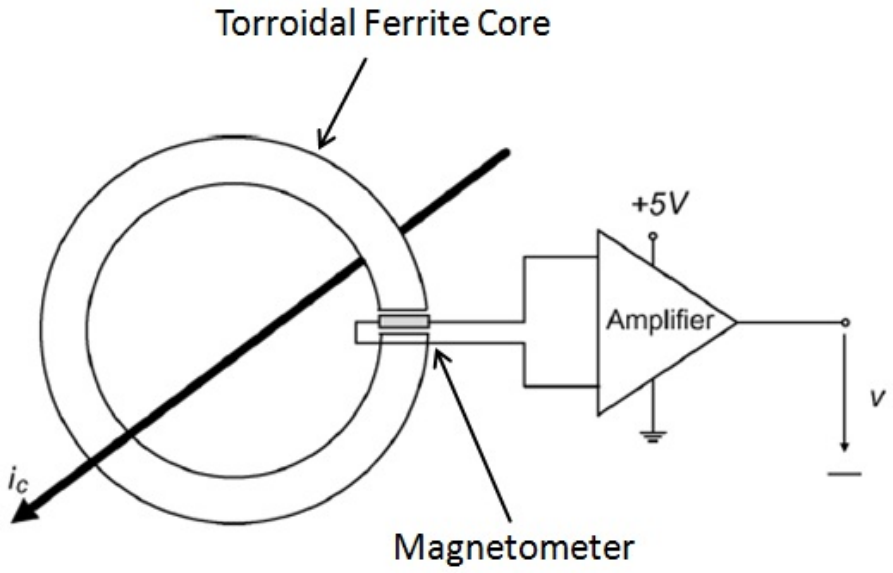

Figure 1.1: A magnetometer located in the gap of a torriodal ferrite core [16].

where H is the H-field, which when integrated around a closed loop is equal to (direction set by right-hand-rule) the current enclosed by that loop. Obviously, this implies that the magnetic field in the core is insensitive to the location that the current passes through the core, which, when combined with the core's high permeability, gives a current sensor of this configuration a great advantage. However, such a current sensor has the disadvantage that it is now vulnerable to magnetization of the core and the non-linear behavior of magnetic permeability.

A common type of magnetometer used for current sensing is the Hall-Effect magnetometer. The force on a charge is given by the Lortenz force equation,

$$F = q(E + v \times B) \tag{1.3}$$

where q is the charge, E is the electric field vector, v is the velocity vector, and B is the magnetic flux density vector. As shown in Figure 1.2, if charges are moving through a conductor and subjected to a non-zero magnetic field B, then the moving charges will experience a force that is perpendicular to both their direction of movement and the direction of the magnetic field. This will force the moving charge to concentrate towards one side

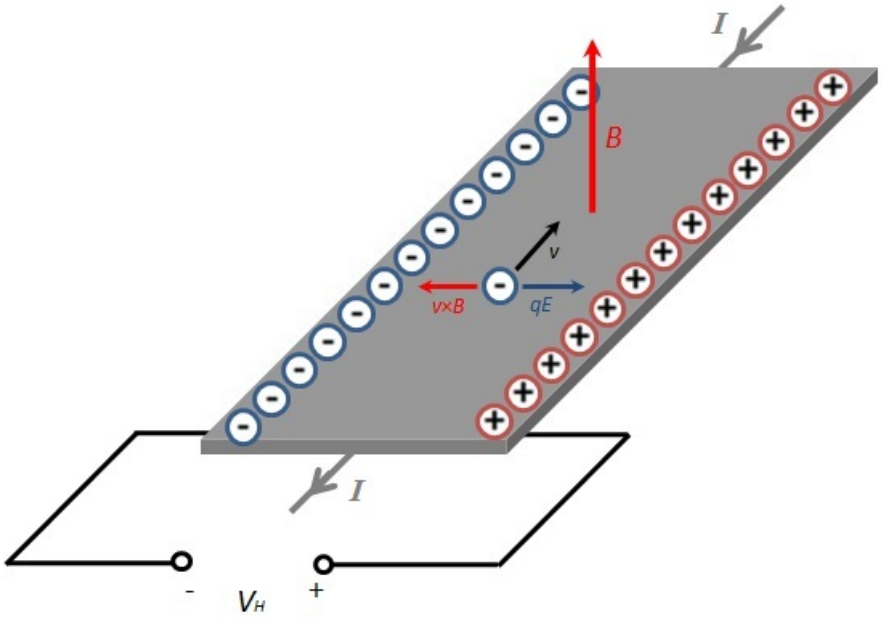

Figure 1.2: The physical mechanism by which the Hall Voltage is produced. Electrons moving through the conductive strip experience a force towards the left through the cross product of their velocity and the magnetic field, $\boldsymbol{B}$. Negative charges build up on the left side of the conductor until enough negative charge accumulates to electrostatically repel any further charge accumulation. A potential is developed between the right and left sides of the conductor.

of the conductor, creating a potential difference across the conductor known as the Hall voltage. Further charge concentration will be prevented by the built-up charge. A Hall Effect magnetometer contains a current-carrying trace (typically a semiconductor material) and outputs an amplified version of the Hall voltage.

Hall-effect magnetometers are frequently used in a ferrite core as shown in Figure 1.1. In this configuration, the current sensor would be called an "open-loop Hall-effect current sensor". However, the Hall voltage is particularly sensitive to temperature effects, and so partly for this reason a second coil is often placed around the core. The amplifier is set to a very high gain, and the output is used to drive a current through this secondary coil which cancels out the magnetic field generated by the sensed current. In this manner, the temperature depedence of the Hall-Effect magnetometer, is removed. This is known as a "closed-loop Hall-effect current sensor".

The Hall-effect magnetometer is simply the most commonly encountered magnetometer used in current sensing; many other types of magnetometers are suitable (as this document will show with a MEMS magnetometer/current sensor).

Also frequently encountered in the field of current sensing is the current transformer, in which the current to be sensed shares a ferromagnetic core with a secondary coil. The secondary coil is lightly loaded and is used to sense the current on the primary. However, as transformers do not function at DC, and the purpose of this research is to provide a DC current sensor, this technology is inapplicable to the problem at hand.

1.2.3 Transistor or Transistor Properties-Based Current Sensing Methods

Methods for current sensing in DC-DC converters have been devised that utilize transistor properties. One of the more conceptually simple methods is to determine the current by measuring the drain-to-source voltage of the transistor (when it is turned on) and dividing it by the drain to source resistance, $R_{DS(ON)}$. This method works because a transistor used in a DC-DC converter, when turned on, will be operated at a high enough gate-to-source voltage to be in the linear region and behave as a (small-valued) resistor. In the linear region, the drain current in a NMOS transistor is given as

$$I_D = \mu C_{OX} \frac{W}{L}(V_{GS} - V_{TH} - \frac{V_{DS}}{2})V_{DS} \tag{1.4}$$

where μ is the majority carrier mobility, C_{OX} is the gate capacitance per unit area, W is the gate width, L is the gate length, V_{GS} is the gate-to-source voltage, V_{TH} is the gate threshold voltage, and V_{GS} is the gate-to-source voltage. Assuming that V_{DS} is small compared to $V_{GS} - V_{TH}$, then the on-state resistance $R_{DS(ON)}$ is simply V_{DS}/I_D:

$$R_{DS(ON)} = \frac{1}{\mu C_{OX} \frac{W}{L}(V_{GS} - V_{TH})} \tag{1.5}$$

However, as μ and V_{TH} are functions of temperature, this approach is not very accurate.

Another method to sense current is reported in [20] and [21] where a current mirror is built into a power MOSFET. The current-mirror MOSFET is in parallel with the power MOSFET and shares all the same characteristics of the power MOSFET except for having a very small W/L ratio. Recalling Equation 1.4, this implies that the current through the SENSEFET will mirror the value of the current through the larger power MOSFET, except for being smaller by a factor of the power transistor's W/L ratio divided by the SENSEFET transistor's W/L ratio. This small current can thus be used to sense the current through the large power MOSFET in parallel.

1.3 Magnetic MEMS

A review of MEMS devices will show that typical devices are actuated through electrostatic forces as opposed to magnetic actuation. This is due to the scaling laws of electrostatic and magnetostatic forces; electrostatic forces are typically applied by an electrode surface, resulting in forces that are proportional to surface area, while magnetostatic forces tend to be proportional to volume. Thus, on large scales, magnetic forces will dominate, while on the micro scales, electrostatic forces will be dominant. In between these extremes is a cross-over region, with critical dimensions very roughly around the scale of 1mm to 1 µm where electrostatic or magnetic forces are both significant enough to be practically used [22, 23]. However, it is important to note that electrostatic actuation will tend to consume less power as the creation of strong variable magnetic fields requires a significant amount of electric current and therefore, power. That aside, for some applications, this is acceptable, or the variable actuation force is externally generated (such as in a magnetometer or current sensor). As the scale in which magnetic forces are still strong enough to be practically used overlaps the scale of most MEMS devices, MEMS devices utilizing magnetic forces have received considerable attention, and are used for tasks such as magnetic field sensing, current sensing, energy harvesting, and mechanical actuation.

1.3.1 MEMS Magnetic Actuation Examples

While all methods for actuation and sensing in magnetic MEMS are just different aspects of the same phenomenon, they can be conceptually separated into groups. Examples include utilizing the Lorentz force on moving charge (currents), magnetostrictive films and materials, magnetic torque, and induction.

Lorentz Force

The Lorentz force on a current-carrying wire is given by

$$F = \int I \cdot dL \times B \tag{1.6}$$

where I is the current, dL is the length element, and B is the external field. This force is utilized in a number of magnetometer designs, an example of which is given in [24], and is shown in Figure 1.3. This magnetometer utilizes current traces on a resonant silicon MEMS device. A sinusoidal current is passed through the traces at the mechanical resonant frequency of the silicon MEMS structure. When an external magnetic field exists, the Lorentz force induced on the current traces and structure causes it to resonate at the mechanical resonant frequency. This motion is detected with piezoresistors.

Magnetostriction

Another method for magnetic sensing and actuation involves the use of the phenomenon of magnetostriction. Magnetostriction is a change in the length of a material under an applied magnetization. If the material increases in length, magnetostriction is positive, while if the material decreases in length, it is negative. Many common magnetic materials exhibit small magnetostrictive effects, but some alloys (such as "Metglas") or composite materials have been fabricated with greatly enhanced magnetostrictive properties. In [25], a MEMS magnetometer is presented that utilizes a magnetostrictive film deposited on a

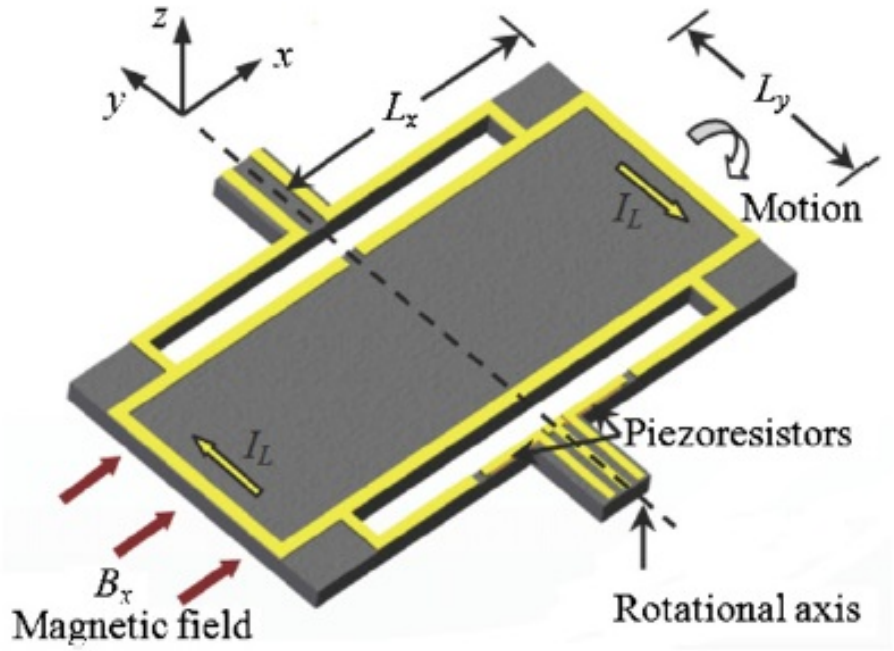

Figure 1.3: A MEMS magnetometer based on the Lorentz force on conducting traces in a magnetic field [24].

silicon membrane. As shown in Figure 1.4, when the film becomes magnetized, it causes a strain on the membrane, resulting in an inward or outward displacement, which is sensed with piezoresistors.

Magnetic Torque

Many devices, such a magnetometers or tilt-based magnetic actuators utilize the torque of mis-aligned magnetic fields to sense or actuate. Assuming a uniform external magnetic field B, the torque exerted on a magnetic field with magnetic dipole moment m is given by

$$T = m \times B \tag{1.7}$$

Typically, the magnetic dipole moment is realized in a magnetic material or micro coil that is affixed to the moving MEMS component. An example of a magnetometer utilizing this magnetic torque concept can be found in [26]. As shown in Figure 1.5, the magnetometer

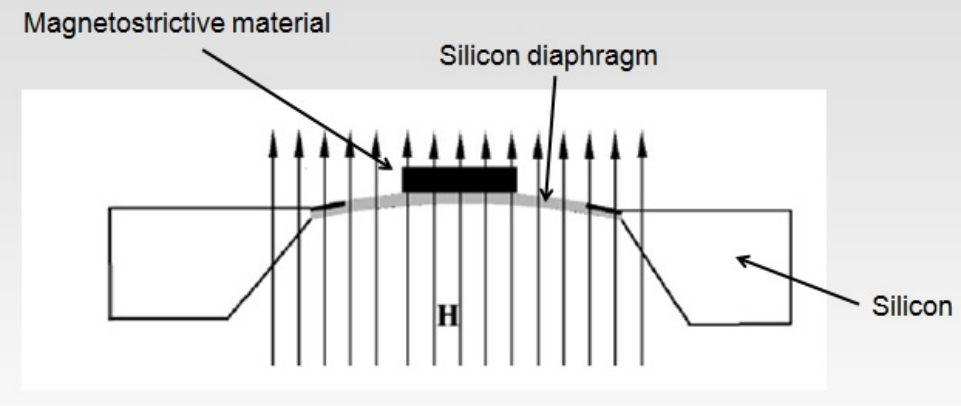

Figure 1.4: A MEMS magnetometer based on a magnetostrictive material that deforms a silicon membrane [25].

utilizes a thin layer of magnetized magnetic materials that is deposited on the surface of a moving silicon platform that is suspended by torsion beams. When an external, out-of-plane magnetic field is present, the suspended MEMS components attempt to align with the field, causing a deflection which can be sensed.

Induction

Magnetic MEMS may also use electromagnetic induction to induce a voltage across and current through a coil. The voltage induced across a coil through which a changing magnetic flux is passing is given by

$$V = -N\frac{d\Phi}{dt} \tag{1.8}$$

where N is the number of turns in the coil and Φ is the flux passing through the coil. The mechanical energy harvester presented in [27] utilizes a magnet suspended on a flexible membrane. As shown in Figure 1.6, copper coils surround the membrane. When the membrane and magnet are displaced by vibrations, the flux passing through the copper coil changes, inducing a voltage and harvesting energy.

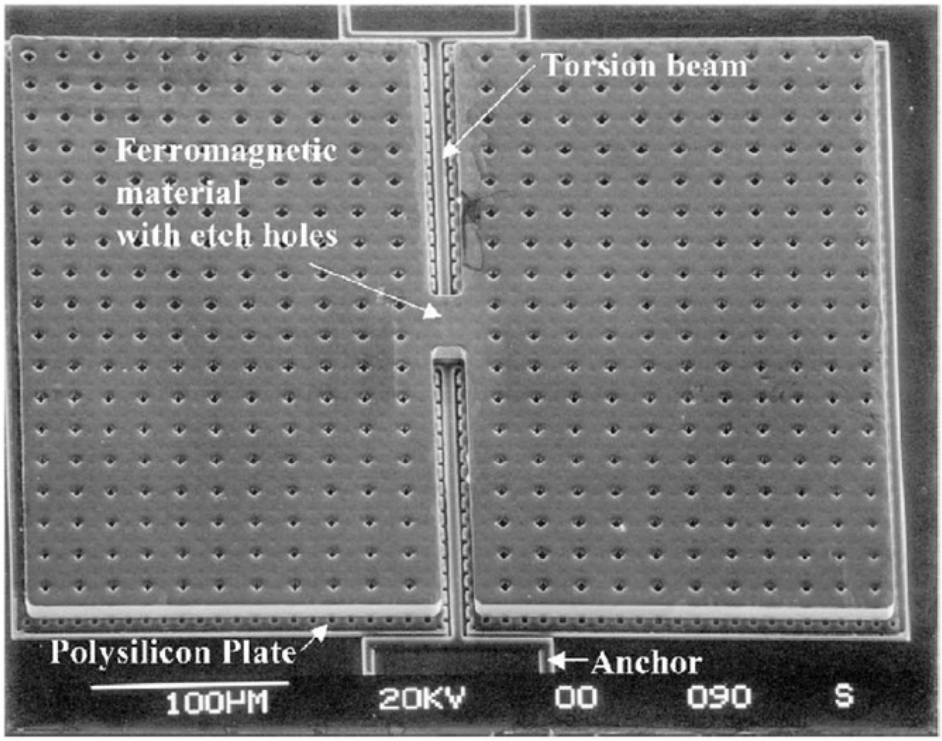

Figure 1.5: A MEMS magnetometer based on a the magnetic torque produced between an external field and a magnetized, torsionally-suspended magnetic material on a silicon substrate [26].

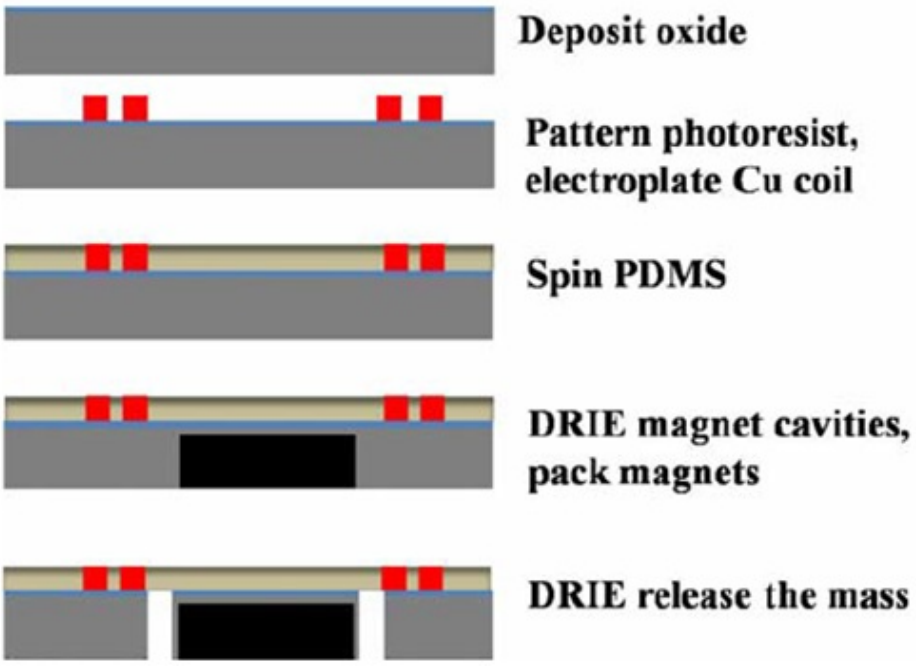

Figure 1.6: The process flow for a MEMS vibrational energy harvester which utilizes the electromagnetic induction of a voltage on a copper coil by a suspended magnet moving due to stray vibrational energy [27].

1.4 Incorporating Magnetic Materials into MEMS

Many magnetic MEMS require ferromagnetic materials that are permanently magnetized. Many approaches exist for integrating permanent magnet components into MEMS devices. The most straightforward method is microassembly- the placing and bonding of a prefabricated magnetic component onto a MEMS structure [23]. Typically, the MEMS structure is created through silicon microfabrication techniques, but this may not always be the case [28]. This method has the advantage of utilizing existing magnet manufacturing methods that are capable of creating thick magnetic structures with the highest possible permanent magnet strengths, but comes with a few disadvantages. First, microassembly does not integrate very well with traditional silicon microfabrication process flows, adding to the costs of packaging. Second, the magnets placed by microassembly cannot be shrunk indefinitely without greatly increasing the difficulty of magnet manufacture and/or placement [29].

A second class of methods for integrating hard magnetic materials into MEMS devices is through surface deposition a magnetic material directly onto the MEMS device, thereby fabricating the magnet as an integrated part of the device's process flow. This approach is far more commonly encountered in literature, as it integrates better with the microfabrication and packaging process. Several methods exist to deposit the permanent magnetic material to be used in the device, including sputtering [30,31], screen printing [32], electroless deposition [33], and electroplating/electrodeposition [29, 34–38]. However these approaches suffer from the inability to make thick permanent magnet layers significantly in excess of a few hundred microns, with screen printing offering the highest thicknesses. Additionally, the reported remnant flux densities and coercivites of these deposited layers tends to only be a fraction of that available in the highest strength pre-fabricated hard magnetic materials.

Another method for depositing hard magnetic materials is demonstrated in [27], which addresses some of the problems inherent in both microassembly and surface deposition/screen printing. A cavity is created in silicon using Deep Reactive Ion Etching (DRIE) which is then filled with a mixture of powered NdFeB and binding wax. This mixture is cured, magnetized, and then released in a second DRIE etch step to create a high volume, hard magnetic structure. However, despite the NdFeB magnet composition, which has the highest remnant flux density of the rare-earth hard magnetic materials, these magnets are reported to only have a remnant flux density of 0.25 T, about a fifth of what is possible with commercial NdFeB magnets.

Chapter 2

Current Sensor Development and Theory

The final design selected for the current sensor in each 12 V - 1 V POL converter stage could not be allowed to reduce the efficiency of the DC-DC converter. Any current sensing method that required the current to be channeled into some kind of sensing element was immediately ruled out as being too inefficient; even if a small-value, current sense resistor is not used (and instead, some kind of Hall-effect current sensor is used), the PCB topology of the DC-DC converter deliberately avoids concentrating current as much as possible, as this leads to higher resistive losses. Thus, sensing the current through measuring the magnetic field it produces was seen as the best option.

Several different MEMS methods for sensing the magnetic field surrounding a DC current trace were investigated early in the design process (these methods included some not detailed in the following sections). Eventually however, it was found that designs that contained a magnetic material that caused a MEMS structure to flex when the material attempted to align with an external magnetic field were the best approach, as a design based on this is relatively simple and easy to fabricate. Two basic designs are examined in the following sections, the first, a device utilizing a magnetic material deposited on a suspended cantilever, and the second, a device utilizing a torsionally-suspended magnetized element. The second was found to be more promising and was ultimately further developed into a working device.

2.1 Cantilever Beam Suspension

Many ways exist to realize a MEMS current sensor. Perhaps the simplest method is to use a structure that experiences a torque and accompanying displacement or deflection

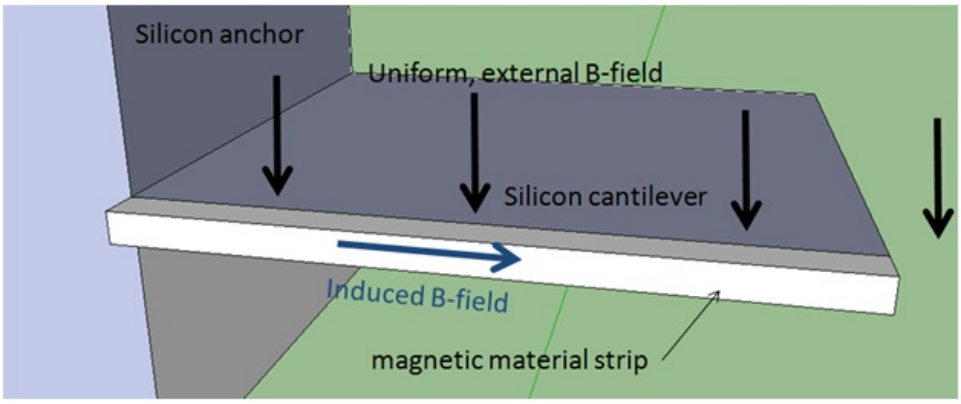

Figure 2.1: MEMS cantilever with magnetic materials plating.

when subjected to an external magnetic field, much as a compass aligns to north in Earth's magnetic field, as already discussed in Section 1.3.1. One of the first designs considered is shown in Figure 2.1. It consists of a MEMS cantilever that has one side plated with a magnetic material.

We will treat the magnetic material on the cantilever as a hard magnetic material (permanent magnet) whose magnetization direction and magnitude is thus unaffected by the comparatively weak external field. When placed in such an external field, the magnetic strip, magnetized in the long dimension, experiences a torque due to the angle between its magnetization and the external magnetic field. This torque acts on the silicon cantilever, causing the end of the cantilever to deflect. This physical displacement can be sensed capacitively by a plate parallel to the silicon cantilever (not shown).

In the presence of a uniform external magnetic field, a magnet experiences a torque if its magnetization direction is not aligned with the external field. This torque is given by

$$\vec{T} = \vec{m} \times \vec{B} \tag{2.1}$$

where T is the torque, m is the magnetic moment of the permanent magnet, and B is the external magnetic field flux density. For the application of a current sensor, we will assume that the sensor is placed so that the field is roughly perpendicular to the magnetization of

the permanent magnet. This reduces the magnitude of the torque given in 2.1 to simply

$$| \vec{T} | = | \vec{m} | \cdot | \vec{B} | \tag{2.2}$$

The magnitude of the magnetic moment of a permanent magnetic can be given as approximately

$$m = M \cdot V \tag{2.3}$$

where M is the magnetization of the magnetic material, and V is the volume of the magnet. For materials with a relative permeability much greater than 1 (as in all strong ferromagnetic materials), then the magnetization of the material is roughly

$$M = \frac{B_{\mathrm{r}}}{\mu_{\mathrm{o}}} \tag{2.4}$$

where B_{r} is the remnant flux density of the magnet and μ_{o} is the free-space permeability.

An approximation for the magnetic field the device will be subjected to is also required. Assume that the device is placed very close to a wide current carrying trace of width w_t and current I. If it is assumed that the device is very close to the trace, the trace approximates to an infinite sheet current, and the expression for the magnetic field becomes

$$H = \frac{J_s}{2} = \frac{I}{2w_t} \tag{2.5}$$

where J_s is the sheet current density (A/m). Assuming that the trace is 6 mm wide, then the magnetic field very close to the trace would be 83 A/m per A. While this number is only accurate for specific geometries, it is reasonable as a represenative case. We can multiply this number by μ_{o} to find B, and using equations 2.1 and 2.3 and the parameters of the

magnetic material, find an approximation of the torque induced on the structure due to the interaction of the external magnetic field and the magnetization of the magnetic material.

Now, the mechanical characteristics of the silicon cantilever must be considered. The displacement of a linear spring, x, under force F is given by Hooke's Law

$$F = -kx \tag{2.6}$$

where k is the spring constant. The spring constant of a cantilever for small displacements (i.e., small enough so that the spring's response is approximately linear) is given by

$$k = \frac{Ewt^3}{4L^3} \tag{2.7}$$

where E is Young's modulus, w is the width of the cantilever (defined to be perpendicular to the cantilever's motion), t is the thickness of the cantilever (defined to be parallel to the cantilever's motion), and L is the length of the cantilever.

To utilize equations 2.7 and 2.6, recognize that a torque on the cantilever is equal to a force F applied at the end of the cantilever, L. Now, we can combine equations 2.2, 2.3, 2.4, 2.6 and 2.7 to obtain an expression for the magnitude of the displacement of the end of the silicon cantilever beam:

$$x = \frac{4L^2 V B_r H_{ext}}{Ewt^3} \tag{2.8}$$

where B_r is the remnant flux density in the magnetic material, V is the volume of that material, and H_{ext} is the external magnetic field. Now, reasonable numbers can be assumed to compute an approximate displacement. First, assuming that the magnetic field is created in the manner as given in Equation 2.5, then for a trace current of 15 A and a width of 6mm, a magnetic field H_{ext} of 1250 A/m can be expected. Secondly, assume that the magnetic material is deposited across the entire side of the cantilever, has a thickness of 10 µm, and a

remnant magnetization B_r of 0.3 T. Assuming a cantilever length L of 1000 µm, a cantilever width w of 250 µm, a cantilever thickness t of 30 µm, and a Young's modulus for silicon of 150 GPa, then we calculate a displacement of 0.44 nm. This is a very low displacement, on the order of the lattice constant of silicon, and represents a sensitivity (in terms of deflection over excitation current) of about 0.03 nm/A, which is far too low to be practical.

While the structure in Figure 2.1 proves to be insufficient for current sensing methods, it proves illuminating in terms of what kind of structures would be sufficient. First, the tiny volume of the magnetic material, probably surface deposited directly on the silicon, severely limits the magnetic moment and thus the amount of torque produced. Two simple ways exist to increase this magnetic moment- increase the volume, and/or increase the remnant magnetization. As discussed earlier, surface deposition of magnetic materials is severely limited in depth (and hence, volume), and typically also cannot approach the remnant magnetization that a traditional magnet can. If the surface deposition approach is abandoned in favor of larger, commercially-fabricated permanent magnetic materials, we can increase both the remnant magnetization and the volume, the latter by several orders of magnitude. In contrast, the remnant magnetization can never exceed about 1.5 T or so in any known magnetic material, and so increasing the magnetization will not be sufficient by itself to create a structure that responds more strongly to external fields. Unfortunately, it is not easy to see where such a large magnet could be mounted on this structure.

A second consideration is the structure's sensitivity to inertial motions. Any structure compliant enough to significantly flex in response to a magnetic field will also measurably flex in response to acceleration and rotation. However, as the device is intended for use in a fixed location, only flexure under gravitational force is a concern (as long as background vibrations remain low, and the structure is sufficiently damped). Unfortunately, as the cantilever-suspended structure shown in Figure 2.1 is not balanced, it will flex significantly under gravity. This problem cannot be resolved using a cantilever structure, as magnetic

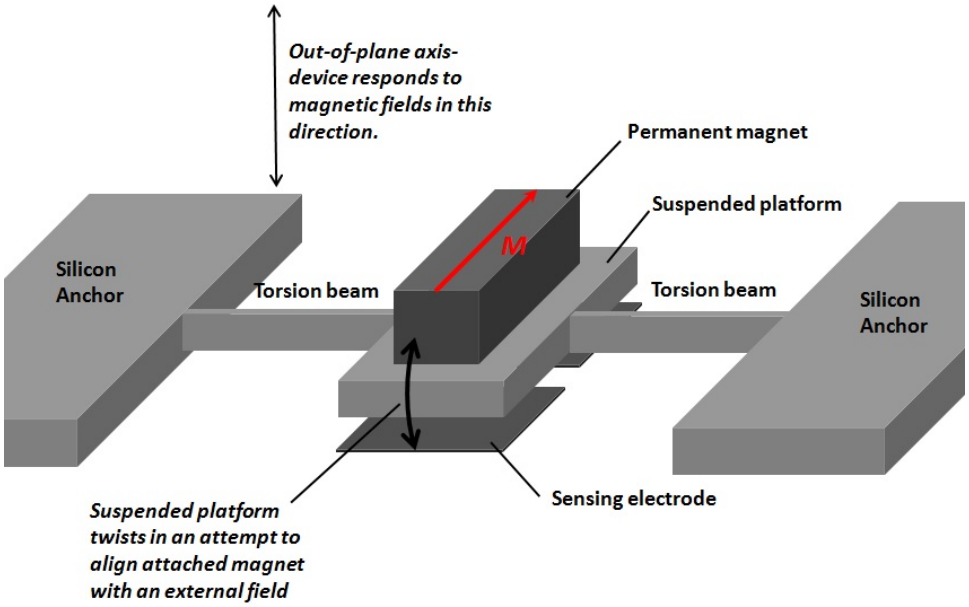

Figure 2.2: Torsionally suspended MEMS current sensor design. Magnetized magnetic materials are placed on a platform suspended by torsion beams. Out-of-plane magnetic fields cause the structure to twist in an attempt to align the magnetic field of the magnetized materials with the external field. This twist is sensed by electrodes which detect the variable capacitance between the suspended structure and the electrode.

materials cannot be made light and with a high enough remnant magnetization to overwhelm gravity when sensing realistic external magnetic field levels.

2.2 Torsion Beam Suspension

In light of the inherent flaws of the cantilever approach for this application, a different structure was evaluated. By placing magnetic material on a platform that is suspended by torsion beams and is allowed to rotate about the torsion beam axis under externally applied magnetic fields, as shown in Figure 2.2, the center of mass is moved very near the torsion beam axis, significantly reducing its flexure due to gravity. The structure can be capacitively sensed by placing electrodes under the moving platform so that a rotation about the torsion beam axis results in a change in the gap distance and hence, in the capacitance between the moving platform and the fixed electrodes.

The structure given in Figure 2.2 remains highly compliant about the torsion beam axis, but either insensitive or non-compliant to motion in other directions. The torsional stiffness of a rectangular torsion spring is proportional to the long cross-sectional dimension times the cube of the short cross-sectional dimension, at least when the two dimensions are significantly different (see equations 2.10 and 2.13). Considering this, the out-of-plane direction (with the plane being the surface of the suspended platform) was chosen as the torsion spring's long cross sectional dimension, and the in-plane direction was chosen as the spring's short cross-sectional dimension. This provides some resistance to undesired out-of-plane motion, as in the out-of-plane direction the torsion springs can be made relatively thick, with any increased stiffness in the torsion spring being offset by a comparatively small decrease in the width of the torsion spring in the in-plane direction.

With the torsion springs relatively thin in the in-plane direction, a considerable amount of cantilever motion in the in-plane direction is allowed. However, as in-plane motion of the silicon plate does not change the spacing between the parallel plate electrodes, this motion can be largely ignored. Similarly, rotation about the out-of-plane axis also does not change the parallel plate spacing. Thus, the structure, if properly balanced, is only susceptible to undesired angular rotation about the torsion spring axis. (The structure pictured in Figure 2.2 is not fully balanced, however, as the magnet material is only located on one side of the platform.) Indeed, the advantages of this basic mechanical configuration for a MEMS magnetometer have been noted and utilized before [26].

The angular deflection of torsion springs is a well studied area [39]. For the structure presented in Figure 2.2, the angular deflection for small deflections can be found with the torsional equivalent of Hooke's Law:

$$\theta = \frac{T}{k_\phi} \tag{2.9}$$

where T is the axial torque, and K_ϕ is the torsional stiffness, which for small angular deflections is given by

$$k_\phi = \frac{2K_{\text{beam}}G}{L} \tag{2.10}$$

where L is the length of the beam, K_{beam} is a cross-section dependent factor, the factor of two comes from the fact that two torsion springs are utilized in this device geometry, and G is the shear modulus of elasticity, which is given by

$$G = \frac{E}{2(1+\nu)} \tag{2.11}$$

where E is Young's modulus and ν is Poisson's ratio (about 150 GPa and 0.25 for silicon, respectively), which works out to be roughly around 60 GPa, with relatively minor variations that are dependent on crystal plane orientation, which we will ignore.

The cross-section dependent factor K_{beam} is given by

$$K_{\text{beam}} = \frac{w^3 t}{3}\left[1 - \frac{192}{\pi^5}\frac{w}{t}\cdot\sum_{n=1,3,5,\ldots}^{\infty}\frac{1}{n^5}tanh(\frac{n\pi t}{2w})\right] \tag{2.12}$$

where w is the short cross-sectional dimension of the bar, and t is the long cross-sectional dimension. Since the goal for these calculations is only a ballpark number, all but the first term of the summation in Equation 2.12 can be discarded. This simplifies the equation for K_{beam} to simply

$$K_{\text{beam}} = \frac{w^3 t}{3}\left[1 - \frac{192}{\pi^5}\frac{w}{t}tanh(\frac{\pi t}{2w})\right] \tag{2.13}$$

Assuming that the torsion beams have a thickness t of 250 µm, a width w of 30 µm, and a length L of 1000 µm, then K_{beam} is approximately 2.08×10^{-18} m^4. This value, used in Equation 2.10, results in an angular stiffness k_ϕ of approximately 2.50×10^{-4} N·m/rad.

To get an approximate idea of the amount of deflection to be expected for this device geometry, assume that the device is placed very close to a wide current carrying trace. As given in Equation 2.5, very close to the trace the field approximates to that given by an infinite sheet current. Assuming that the trace is 6 mm wide, then the magnetic field very close to the trace would be 83 A/m per A. If we assume a magnet that measures 1500 µm X 500 µm X 500 µm and has a remnant flux density of around 0.3 T, a relatively weak permanent magnet, then using equations 2.4, 2.3, then 2.2, the approximate torque on the magnet for a 83 A/m H-field is 9.4×10^{-9} N·m, as long as the external field is perpendicular to the magnet's magnetization direction.

Applying the torque value found above and the previously found angular stiffness k_ϕ to Equation 2.9, we arrive at an estimated angular displacement of approximately 3.75×10^{-5} rad/A. If we assume that the end of the moving silicon platform is 1000 µm from the torsion beam axis, this represents a displacement of 1000 µm$\cdot sin(3.75 \times 10^{-5}) = 37.5$ nm/A. This represents a much more easily sensed displacement, considering that the bottom electrode is spaced only a few tens of microns or less below the moving platform.

A large part of the reason that this design represents such a large improvement over the cantilever design presented first is that the volume of the magnetic material is hugely increased (by a factor of 1250), with a corresponding proportional increase in the magnetic moment and torque. Such a large increase in magnet volume would have been difficult with the cantilever design without causing such a large deflection due to gravity that the device cannot be made practical. This design makes use of such a large mass of magnetic material possible by moving the mass close to the balance point of the torsionally-suspended platform, and by providing the large, torsionally-suspended platform on which the magnet can be mounted.

Figure 2.3: The assemblage of three NdFeB magnets used in the prototype current sensor as compared to a U.S. penny. The magnets each measure 1.6 mm X 1.6 mm X 1.6 mm, with three of them stuck together forming an effective 4.8 mm X 1.6 mm X 1.6 mm magnet magnetized in the long dimension.

2.3 Current Sensor Prototype #1

After the favorable results of the analysis of the torsionally-suspended structure, it was decided to proceed with constructing a prototype. NdFeB magnets were selected due to their wide commercial availability and their very high remnant flux densities (typically greater than or equal to 1.1 T). For the prototype device, three 1.6 mm X 1.6 mm X 1.6 mm NdFeB cube magnets were stuck together to form a single effective magnet 4.8 mm X 1.6 mm X 1.6 mm, magnetized in the long dimension. This assembly is shown compared to a U.S. penny in Figure 2.3.

The silicon component of the prototype device contained a moving platform with roughly the same cross section as the magnet's dimensions (4.8 mm X 1.6 mm), and was fabricated on a 450 µm thick silicon wafer. Photolithography followed by Deep Reactive Ion Etching (DRIE) was used to define the torsion springs and the suspended silicon platform. To give these MEMS components freedom for movement, an additional 150 µm of silicon was etched away from the backside to effectively thin the wafer to 300 µm in the region where the torsion

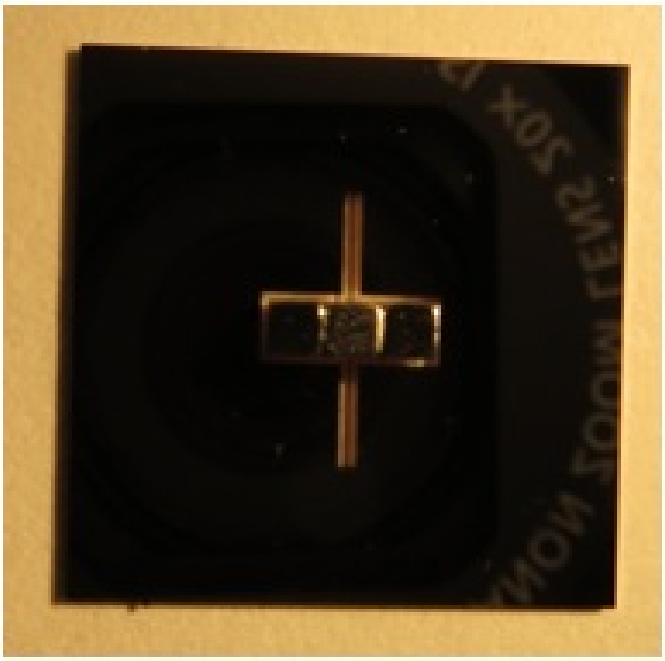

Figure 2.4: An assembled first prototype of the torsionally-suspended MEMS DC current sensor design.

springs and moving platform were defined. The device came in two varieties, one with silicon torsion springs 30 µm wide and another with torsion springs 50 µm wide. On both varieties, the length of the torsion springs was 3200 µm, and the height was the difference between the wafer thickness and the depth of the backside etch, a distance nominally about 300 µm. An example of one of these devices with the magnets attached is shown in Figure 2.4.

When fabrication was complete, the prototype was tested on a PCB with a current trace geometry that creates an H-field of about 100 A/m per A of current at the location of the magnets/MEMS component (calculated using Biot-Savart's law and a script similar to the one given in Appendix C). Using equations 2.2, 2.3, 2.4, 2.9, 2.10, and 2.13, and assuming a remnant flux density in the permanent magnet of 1.1 T, an expected angular displacement of 3.2 mRad (0.18 degrees) per amp of current flowing through the test trace is predicted. To test these predictions against a prototype device, a prototype device with 50 µm wide torsion springs was assembled and a piece of reflective tape was placed on top. A laser beam was reflected off the reflective tape and the position of the reflected spot was measured to

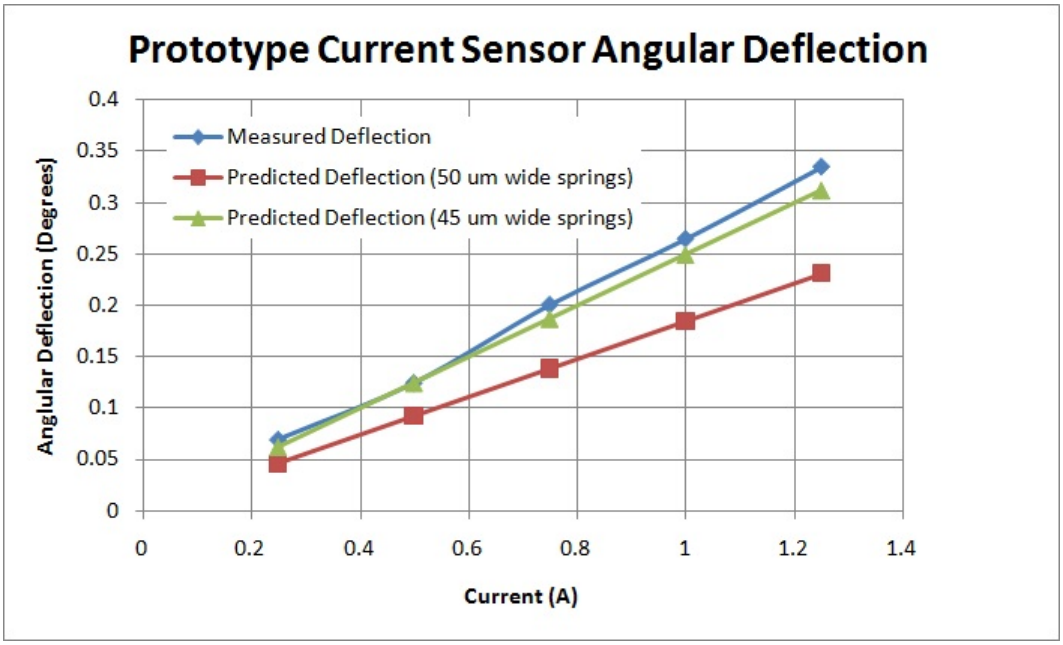

Figure 2.5: Test results from the first current sensor prototype. A laser beam was reflected off the moving components to measure tilt as current was passed through a test trace that produces about 100 A/m at the MEMS component per A of excitation current. Measured results seem to match a device with 45 µm wide torsion springs, rather than the intended 50 µm.

determine the angular deflection as varying currents were passed through the test trace. The results of this experiment are shown in Figure 2.5.

As Figure 2.5 shows, the prototype device deflects a bit more than predicted for having 50 µm wide torsion springs. There are many possible explanations for this. Most likely, the springs were not exactly 300 µm X 50 µm. The DRIE etch process used to fabricate these devices tends to over-etch beyond the nominal boundaries of the pattern, especially as these devices had poor thermal contact to the backing wafer as etching was completing, which allows them to heat up and accelerate the loss of the protective photoresist mask layer. Springs that were supposed to be 50 µm wide could very easily be etched down 45 µm in width. If this were the case, then the angular deflection expected would be very close to the measured values, as shown in Figure 2.5. Additionally of note was that the reflection off the reflective tape was somewhat diffuse, which introduced some measurement error.

Considering all this, the results of the testing of the prototype current sensor were well within expected deviations from the predicted performance of the device. The predictions were primarily to get "ballpark" numbers, and in this respect, they were completely successful. With the success of the prototype device, a second prototype was designed.

2.4 Current Sensor Prototype #2

The primary goal of the second current sensor prototype was to miniaturize the design to a more practical size. A second goal was to provide mechanical stops that prevented the device from being destroyed by over-ranging. Finally, the design was intended to be integrated with a digital differential capacitance measuring integrated circuit, the AD 7152.

The layout and dimensions of the MEMS components of the second prototype DC current sensor design are given in Figure 2.6. The design utilizes a commercially manufactured 1500 µm X 500 µm X 500 µm NdFeB magnet magnetized in the long dimension. These magnets were custom-ordered and manufactured for this project by Amazing Magnets LLC from material "42SH", a sintered NdFeB alloy with a remnant magnetization around 13 kG, a coercivity greater than or equal to 12.4 kOe, an intrinsic coercivity of around 20 kOe, a BHmax product of 40-43 MGOe, and a Curie temperature around 150 C. (Though the magnets purported have a flux density of 1.3 T, 1.1 T will be used in this work for more conservative calculations.) One of these magnets is shown compared to a U.S. penny in Figure 2.7.

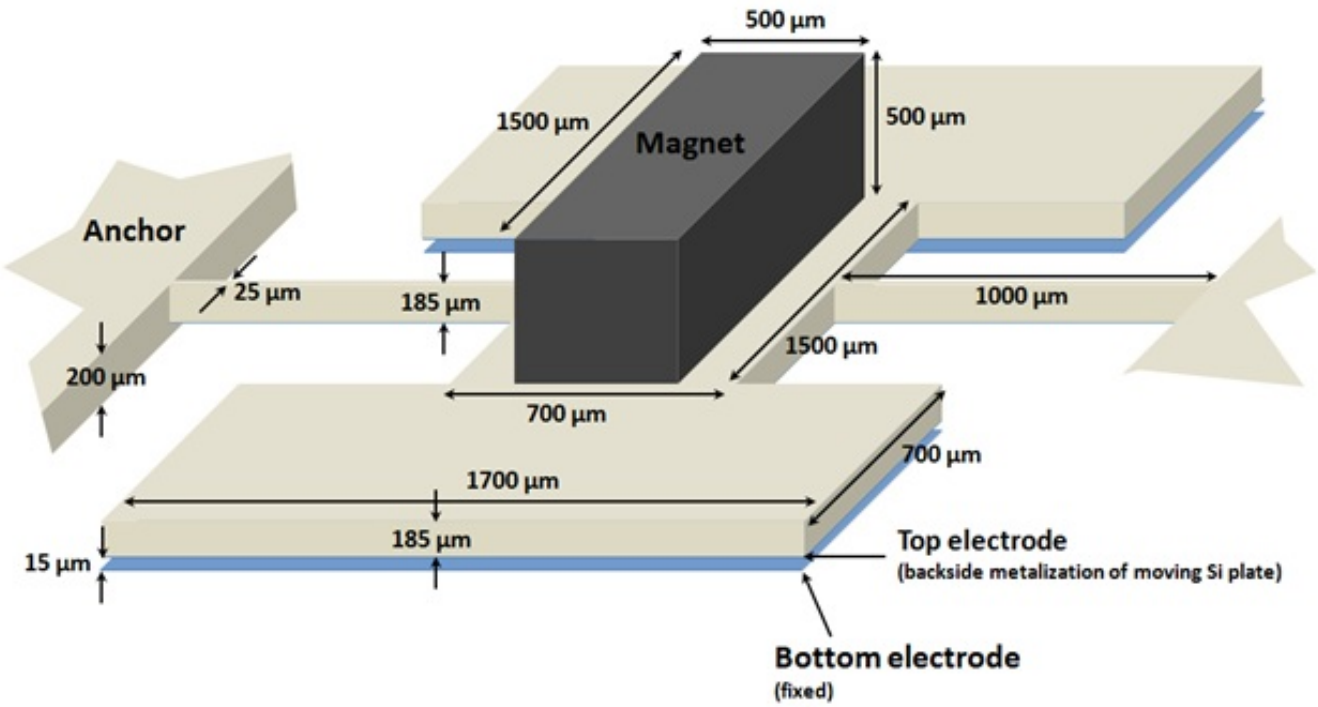

Figure 2.6: Dimensions and layout of the second current sensor prototype.

Figure 2.7: A 1500 µm X 500 µm X 500 µm NdFeB magnet like the ones used in the second MEMS current sensor prototype and the final MEMS current sensor design.

The second current sensor prototype design was fabricated on 100 mm diameter, 250 µm thick, ⟨100⟩ p-type silicon wafers using silicon bulk micromachining techniques. Most of

the fabrication issues encountered and solved were also applicable to the final current sensor design, and so will be discussed in more detail in Chapter 4.

Three different kinds of components were manufactured- the MEMS components on which the magnet is placed, a mechanical stop component that fits over the top of the MEMS component that prevents the torsion springs from over-ranging, and "placer" components that were supposed to allow for easy placement and attachment of the NdFeB magnet on to the suspended MEMS platform. A picture of the front and back of all these components is given in Figure 2.8. An assembled device on a test PCB is shown in Figure 2.9.

Several lessons were learned from the second prototype current sensor. While testing showed that mechanically and magnetically it operated as expected, electrically the capacitance variation was very small, and it was difficult to get the AD7152 capacitance-measuring IC working correctly (largely because the software for communicating with the IC was not compatible with Windows 7). The capacitance between two closely spaced parallel plates is given by

$$C = \frac{\epsilon A}{d} \tag{2.14}$$

where A is the area of the parallel plates, d is the spacing between the parallel plates, and ϵ is the permittivity of the intervening dielectric material (in this case, just air). In the case of this design, each electrode measures 1700 µm X 700 µm and has a nominal gap spacing of 15 µm. This results in a capacitance of just 0.7 pF. This is a small capacitance to be measuring compared to parasitic and gate capacitances which will be on the order of a few pF. Much smaller variable capacitances than this value are routinely measured in commercial MEMS devices, but this is usually done by integrating the measuring electronics (or at least, the front-end part of the measuring electronics) onto the same die as the MEMS device, and this approach was not possible in this case. A larger capacitance would allow a much simpler method of measuring capacitance to be used, allowing for less development time to be spent

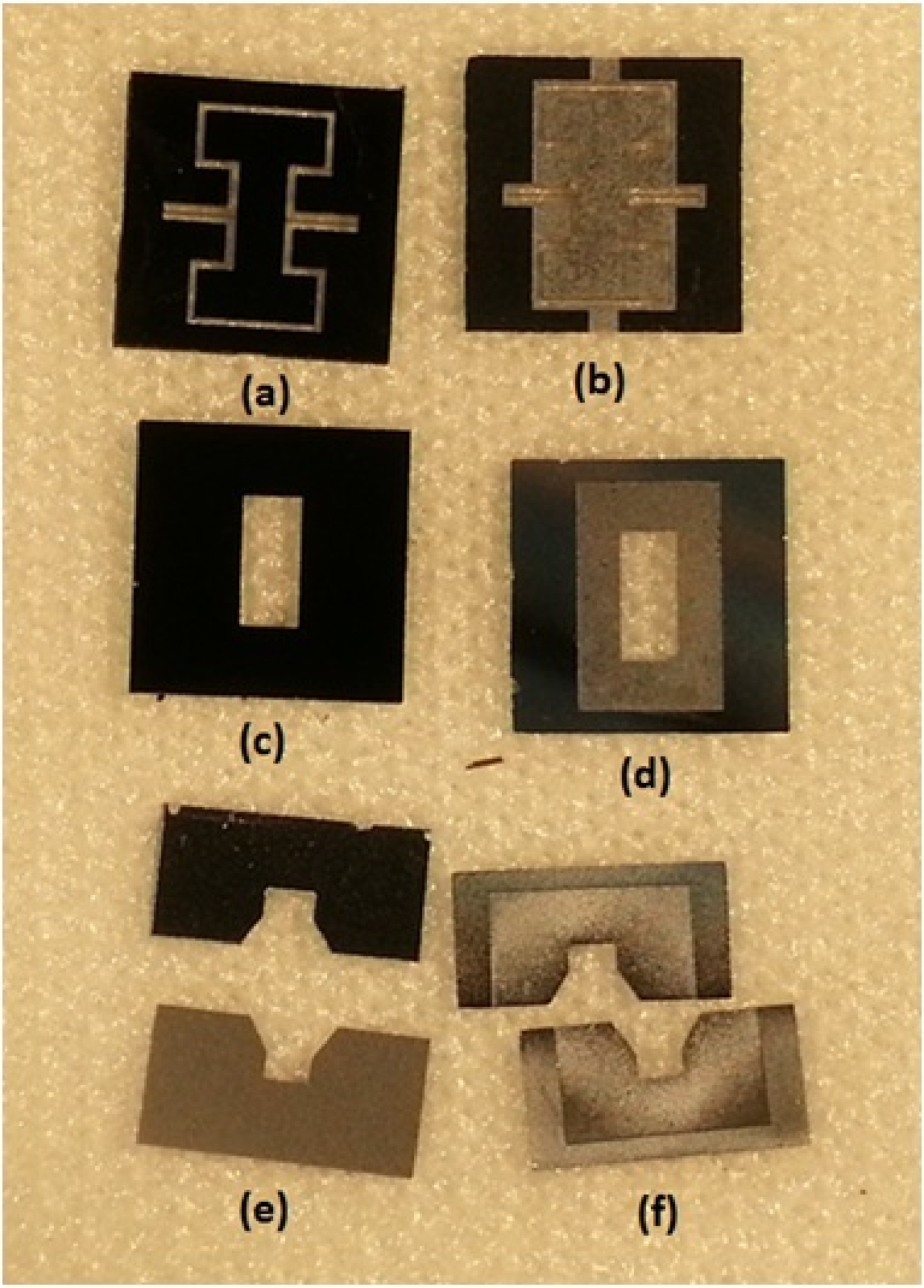

Figure 2.8: Components of the second prototype current sensor. a)Topside of MEMS component. b)Bottomside of MEMS component. c)Top side of mechanical stop component. d)Bottomside of mechanical stop component. e)Topside of "placer" component (X2). f)Bottomside of "placer" component (X2).

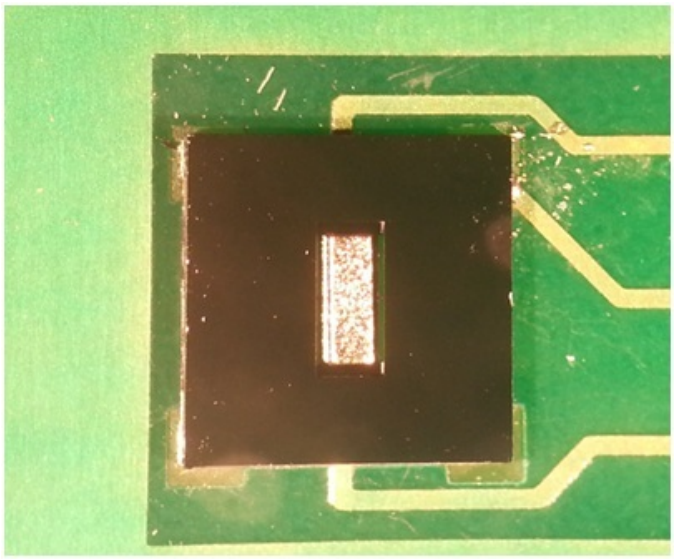

Figure 2.9: A completed second prototype of the MEMS DC current sensor on a test PCB. Note that the MEMS components are mostly hidden under the overlying mechanical stop.

on capacitance read-out circuitry. At the same time, it was recognized that perhaps the sensor was smaller than it really had to be. The overall size of the device could be increased allowing for a larger variable capacitance to be created.

The mechanical stop component proved to be very effective. One motivation for the mechanical stops was a particular instance when an assembled first prototype design, which lacked any kind of mechanical stop, was destroyed when the table it was sitting on was lightly bumped into by a passing student. In contrast, with the mechanical stop attached, no second prototype design was ever destroyed. Additionally, the use of epoxy to attach stacked silicon components was proven to be effective, as long as very small amounts of epoxy were placed with extreme care.

On the other hand, the "placer" components proved to be a failure, and instead, a superior method of manually assembling the components using a microscope, non-magnetic tools, and a small diameter wire was developed. This and other assembly and fabrication issues that were encountered and solved will be presented in the next section.

Finally, the lack of a cap over the device to seal it from the outside environment needed to be addressed. While designing the second prototype, it was still thought that perhaps the

cap would be constructed through CNC machining of metal. However, the success of gluing the mechanical stop on top of the MEMS components showed that a cap could simply be constructed from several stacked silicon components.

Chapter 3

Final Current Sensor Design

3.1 MEMS Components

A final design iteration took place to increase the value of the variable capacitance created by the structure so that it could be sensed easily, and also provide for a cap over the device so that it can be sealed from outside contamination, a necessity for a practical device. The layout of this design is given in Figure 3.1. The outer frame/anchor of the design measures 5.4 mm X 5.4 mm, and can be seen in the photolithography mask layout used for this device, shown in Figure 4.1.

As with the prototype designs detailed earlier, the bottom, fixed electrode in this design's moving parallel plate electrode is realized with a PCB pad. The gap between the moving electrodes, a parameter that in part determines the device's nominal capacitance, range of motion, and sensitivity, is set through the etching of the bottom side of the moving Si platform. Using the same 100 mm diameter, 250 µm thick, $\langle 100 \rangle$, highly-doped p-type, double-side polished silicon wafers ordered for the earlier second prototype design, two batches of devices were prepared. One batch utilized a 15 µm gap and the other had an 8 µm gap. Most of the 15 µm gap devices went unused, and for the following performance calculations, an 8 µm gap is assumed.

Care was taken to balance the device so that the weight of the magnet, and the portion of the moving platform it rests on, exactly counter-balances the weight of the large moving plate portion on the other side of the torsion springs. This was to largely avoid a net torque from being applied to the springs when an out-of-plane acceleration or gravitational force acted on the structure.

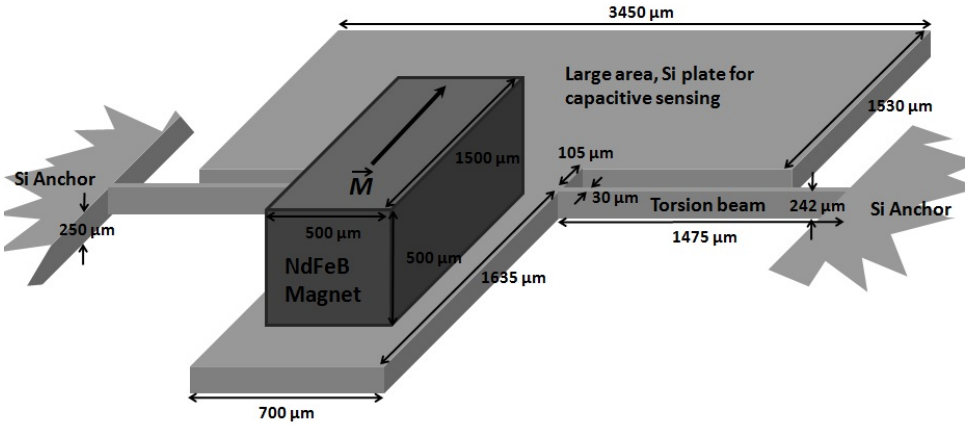

Figure 3.1: Final current sensor design. The MEMS components shown are realized in silicon using bulk micromachining techniques, and are anchored to an outer silicon frame 5.4 mm X 5.4 mm.

As mentioned earlier, a goal of the final design iteration was to provide a larger variable capacitance than the previous prototype designs had provided. The electrode geometry shown in Figure 3.1 is intended to provide a capacitance significantly larger than the gate capacitances of the sensor electronics. With no external field, and a gap width of 8 µm, it provides a nominal capacitance of around 5.8 pF as given by the dimensions shown in Figure 3.1 and Equation 2.14. External fields in the out-of-plane direction will cause this value to either increase or decrease, depending on the external field direction and the orientation of the permanent magnet.

3.1.1 Predicted DC Performance

To find the predicted performance of this design, first apply equations 2.10, and 2.13 for the 30 µm X 242 µm X 1475 µm torsion springs that this device geometry utilizes to find that K_{beam} is approximately 2.01×10^{-18} m^4. This value, used in (2.10), results in an angular stiffness k_ϕ of approximately 1.63×10^{-4} N·m/rad. Next, assume that the device is placed close to a trace so that the trace produces a magnetic field of 41 A/m in device's sense direction (see Section 5 for the layout of the test current trace geometry that yields 41 A/m/A). The same 1500 µm X 500 µm X 500 µm NdFeB magnets used for the second

prototype design are used in this device. Using equations 2.4, 2.3, then 2.2, and the remnant flux density of 1.1 T the magnets possess, the approximate torque on the magnet for a 41 A/m H-field is 1.691×10^{-8} N·m, as long as the external field is perpendicular to the magnet's magnetization direction.

Applying the torque value found above and the previously found angular stiffness k_ϕ to Equation 2.9, we arrive at an estimated angular displacement of approximately 1.035×10^{-4} rad/A. Inspecting Figure 3.1, it is seen that the moving electrode plate begins 120 µm past the pivot point for the torsion springs, and continues an additional 1530 µm. Thus, a 0.126 mrad angular rotation about the torsion springs would yield an out-of-plane displacement at the beginning of the electrode of 120 µm·$sin(1.035 \times 10^{-4}) = 12.4$ nm, and an out of plane displacement at the end of the electrode of 1650 µm·$sin(1.035 \times 10^{-4}) = 170.8$ nm. Thus if the electrode gap was 8 µm, one could expect that the device, under this assumed current trace geometry, could detect currents up to approximately 47 A before coming into contact with the bottom electrode (and upward motion will be limited by approximately the same amount by a mechanical stop, as discussed in Section 3.2).

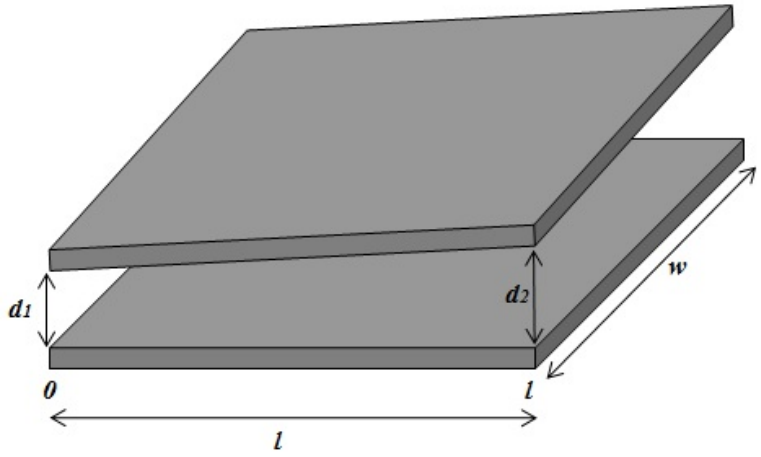

Figure 3.2: A tilted plate capacitor.

To estimate the amount of variation in capacitance this gives, a derivation for the capacitance of a tilted-plate capacitor is found. Assume that an air-gapped, parallel-plate capacitor that is l long and w wide has a small tilt induced on its upper plate as shown in

Figure 3.2. l is given to be in the x direction, and both plates span from $x = 0$ to $x = l$. As shown in Figure 3.2, at $x = 0$, the gap value is d_1, and at $x = l$, the gap value is d_2. Assuming that each plate can be approximated as an infinite sheet charge and that the charge distribution on each plate is uniform and with a given density of ρ_s, then the electric field E between the two plates is given as

$$E = \frac{\rho_s}{\epsilon_o} \tag{3.1}$$

which is double the value of the electric field for an infinite sheet charge in free space because there are two plates, not just one. Assuming the electric field lines are straight, uniform and are roughly normal on each plate surface, and have a magnitude as given in (3.1), then the voltage between the two plates at any point on x between 0 and l is given as

$$V = E \cdot d = \frac{\rho_s}{\epsilon_o}\left(\frac{d_2 - d_1}{l}x + d_1\right) \tag{3.2}$$

Finally, to derive the capacitance, recall that capacitance is given as $C = Q/V$. The amount of differential charge is given as $\rho_s \cdot w \cdot dx$, making the total capacitance

$$\begin{aligned} C = Q/V &= \int_0^l \frac{\rho_s \cdot w}{\frac{\rho_s}{\epsilon_o}\left(\frac{d_2-d_1}{l}x + d_1\right)}dx \\ &= \frac{\epsilon_o w l}{d_2 - d_1} \cdot \ln\left(\frac{d_2 - d_1}{l}x + d_1\right)\Bigg|_{x=0}^{x=l} \\ &= \frac{\epsilon_o w l}{d_2 - d_1} \cdot \ln\left(\frac{d_2}{d_1}\right) \end{aligned} \tag{3.3}$$

The first term in the Taylor expansion of $ln(x)$ is $ln(x) = x - 1$ (when $0 \leq x \leq 2$), so in the limit of $d_2 = d_1$, Equation 3.3 reduces to $C = \frac{\epsilon_o w l}{d_1}$ the expression for a parallel plate capacitor (also given in Equation 2.14). This is a good check on the validity of Equation 3.3.

Returning to displacement of the structure for a current-generated H-field of 41 A/m per amp, recall that the predicted displacement for one amp of current was 12.4 nm at the beginning of the moving electrode and 170.8 nm at the end. Recall that for this design, the moving electrode is 1530 µm in length by 3450 µm in width, with a nominal gap distance of 8 µm. Applying Equation 2.14 to the nominal gap distance gives a capacitance of 5.842 pF, as previously discussed. Assuming that the current-induced displacement occurs in the direction to lessen the gap distance, then applying Equation 3.3 leads to a new capacitance of 5.910 pF.

As will be discussed in Section 3.2, a CMOS relaxation oscillator circuit is used to read out this capacitance and convert it to a frequency. As given by Equation 3.8 in that section, the nominal operating frequency for the read-out circuit is approximately 29.01 kHz for a 5.842 pF variable MEMS capacitance and a 2 pF parasitic capacitance. Therefore, from the application of a 41 A/m H-field causing the MEMS capacitance to increase to 5.910 pF, one could expect a new output frequency of approximately 28.76 kHz with a total change of about 250 Hz; in other words, the devices are predicted to have a current responsivity of about 250 Hz/A on the 41 A/m/A test trace.

A MATLAB script that solves all the equations in this section and predicts device behavior is given in Appendix B.

3.1.2 Predicted AC Performance

Even though the device was originally intended for sensing DC fields, it is still necessary to predict the harmonic response of the system. The transfer function of the system should resemble the torsional equivalent of the traditional force-actuated spring-mass-damper system:

$$\frac{\Theta(s)}{T(s)} = \frac{1}{Is^2 + cs + k_\phi} \tag{3.4}$$

where $T(s)$ is the torque, I is the moment of inertia, and c is a term representing damping. The system thus has a natural frequency given by

$$f_o = \frac{1}{2\pi}\sqrt{\frac{k_\phi}{I}} \tag{3.5}$$

The moment of inertia about the centroid of a rectangular prism is given by

$$I = \frac{1}{12} m \left(l^2 + h^2\right) \tag{3.6}$$

where l and h represent the dimensions perpendicular to the axis of rotation, and m is the mass of the rectangular prism. When the axis of rotation is parallel to this axis but displaced in the perpendicular dimensions, the parallel axis theorem gives the moment of inertia at the new axis as

$$I = I_o + mr^2 \tag{3.7}$$

where I_o is the moment of inertia through an axis, m is the mass of the object, and r is the radial distance from the old axis to the new axis. The structure given in Figure 3.1 can be decomposed into three rectangular prisms about the torsion spring axis- two of silicon, one for each width of the moving platform, and one of NdFeB. Assuming the density of silicon to be 2330 kg/m^3 and the density of NdFeB to be 7400 kg/m^3, then using equations 3.6 and 3.7 the moment of inertia can be found to be 6.04×10^{-12} kg·m^2. Applying this value for I and the value of k_ϕ previously found for 30 µm-wide torsion springs to Equation 3.4, and assuming a (mostly arbitrary) damping coefficient, c, of 1×10^{-9} N·m/rad/s, then plots of the transfer function magnitude, real part, and phase are shown in figures 3.3, 3.4, and 3.5.

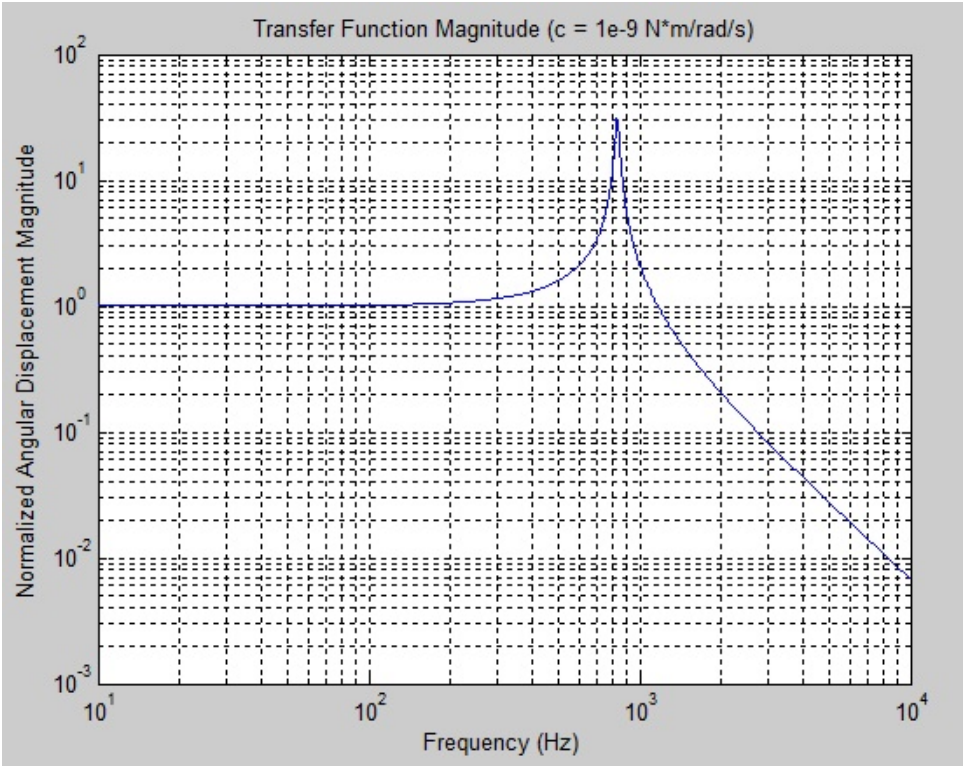

Figure 3.3: Predicted transfer function magnitude (arbitrary units) for $k_\phi = 1.63 \times 10^{-4}$ N·m/rad, $c = 1 \times 10^{-9}$ N·m/rad/s, and $I = 6.04 \times 10^{-12}$ kg·m.

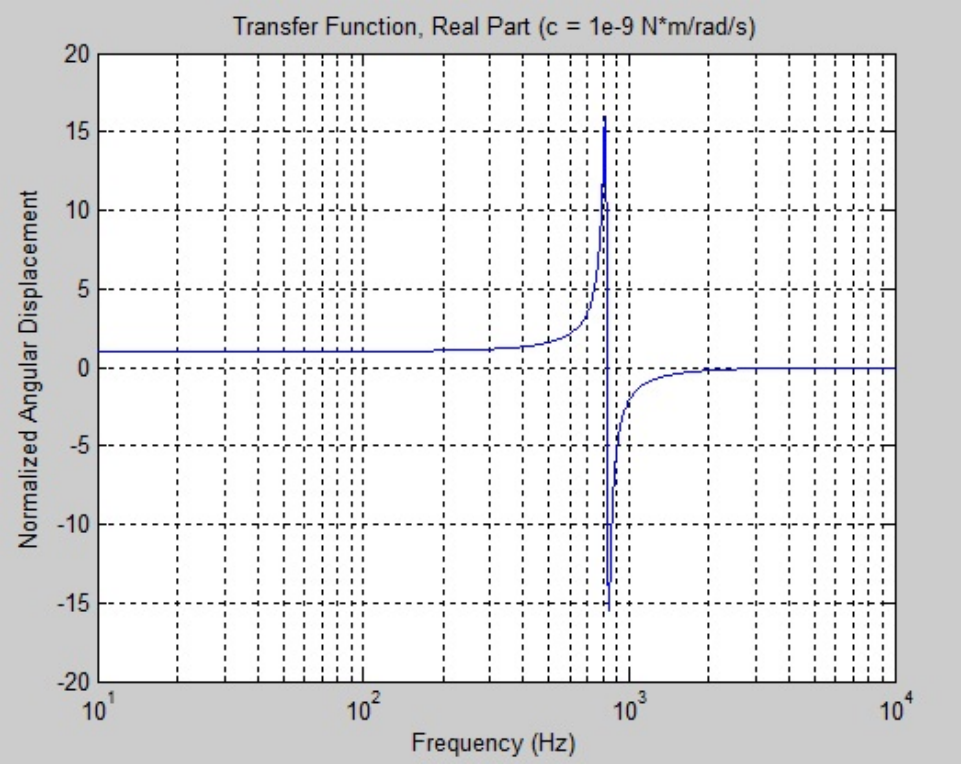

Figure 3.4: Predicted transfer function real part (arbitrary units) for $k_\phi = 1.63 \times 10^{-4}$ N·m/rad, $c = 1 \times 10^{-9}$ N·m/rad/s, and $I = 6.04 \times 10^{-12}$ kg·m.

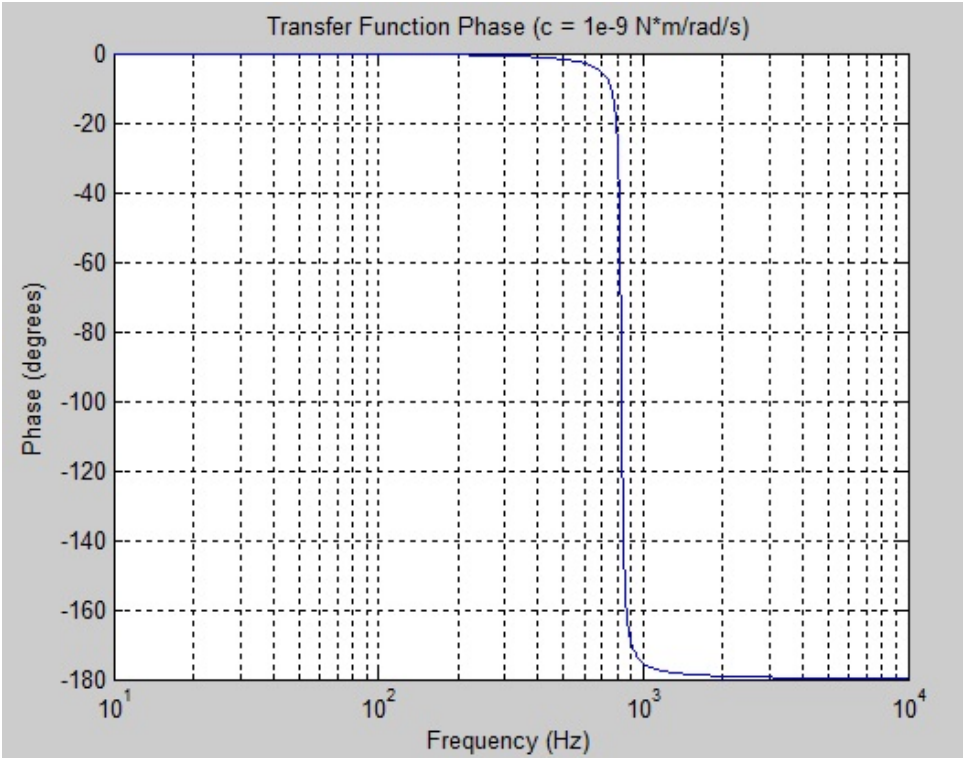

Figure 3.5: Predicted transfer function phase for $k_\phi = 1.63 \times 10^{-4}$ N·m/rad, $c = 1 \times 10^{-9}$ N·m/rad/s, and $I = 6.04 \times 10^{-12}$ kg·m.

As shown in Figures 3.3 and as predicted by Equation 3.5 a natural frequency of about 828 Hz is predicted for the 30 µm-wide springs. Reducing the spring width to 20 µm, as can happen through over-etching during the fabrication process, reduces the predicted natural frequency to 457 Hz. Past the natural frequency, the system's response is expected to fall off at -40 dB/decade. However, this analysis assumes low damping. The response of an overdamped system will decrease well before the natural frequency is reached, and no harmonic peak will be exhibited. As will be shown later, test results indicate that this is in fact the case for this design when sealed under atmosphere. A MATLAB script that solves all the equations in this section and predicts device behavior is given in Appendix B.

3.1.3 ANSYS Mechanical Analysis

In addition to analytical calcuations in MATLAB, predictions of device behavior was made using an ANSYS 15.0 mechanical model. The device geometry was defined in ANSYS

Design Modeler. The silicon components were defined to have a Young's Modulus of 150 GPa, Poisson's ratio of 0.25, a shear modulus of elasticity of 60 GPa, and a density of 2330 kg/m^3. The NdFeB components were defined to have a density of 7400 kg/m^3 (the other attributes do not matter as the NdFeB components do not undergo strain). As in the previous calculations, the mass of the glue holding the NdFeB magnet to the moving platform was neglected. The entire volume of the torsion springs were meshed into 5 µm side-length cubes, while all other portions of the structure (which do not undergo strain and thus do not need to be finely meshed) were left on the, larger, default mesh size.

Recall that in Section 3.1.1, it was predicted that a field of 41 A/m directed in the device's out-of-plane direction should produce a torque of 1.691×10^{-8} N·m about the torsion springs. (This number comes from a current trace geometry used in device testing that produces about 41 A/m per A of excitation current; see Chapter 5.) A "Static Structural" analysis was done on the structure, with the ends of the torsion beams fixed and a torque of 1.691×10^{-8} N·m applied to the magnet, and the results are shown in Figure 3.6. As Figure 3.6 shows, ANSYS predicts that for the applied torque, the structure should displace 11.57 nm at the beginning of the moving plate and 159.1 nm at the end. This is in close agreement with the respective values of 12.4 nm and 170.8 for this displacement predicted analytically in Section 3.1.1 using torsion beam properties.

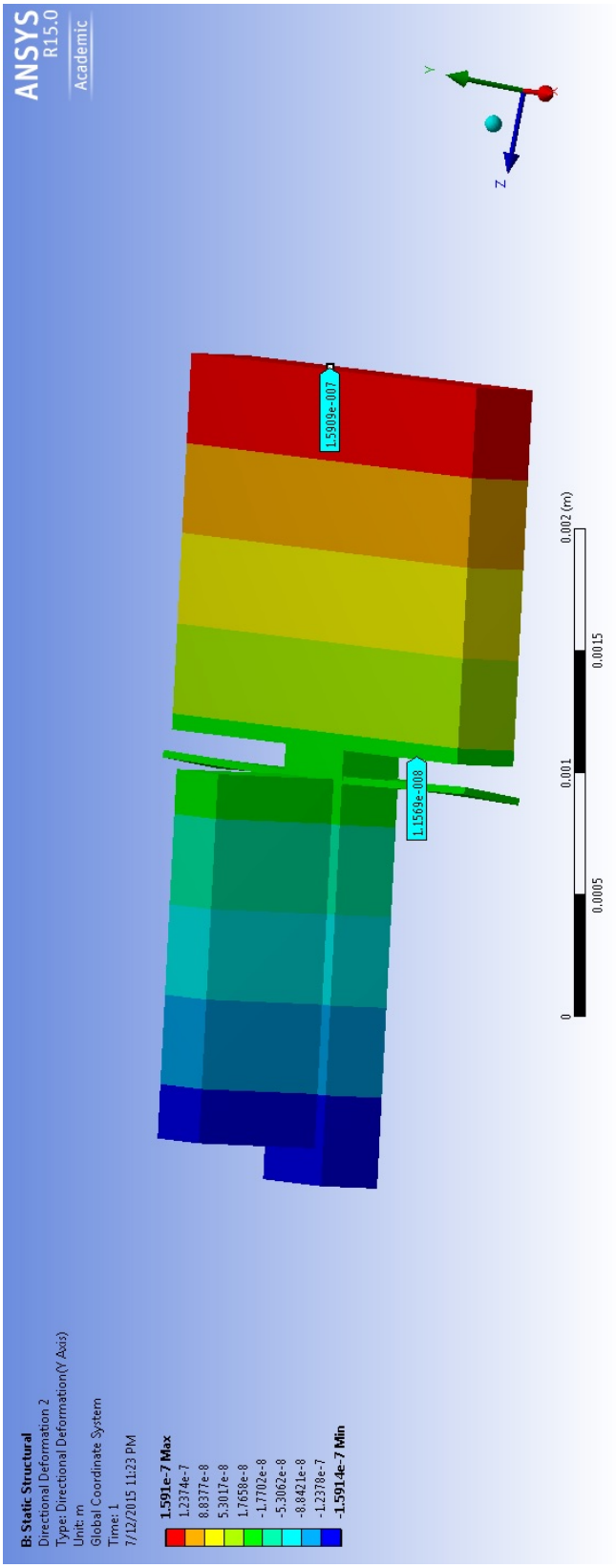

Figure 3.6: ANSYS Static Structural analysis of the current sensor with a torque of 1.691×10^{-8} N·m (the torque produced by a 41 A/m external field) applied.

In addition to a Static Structural analysis, an ANSYS modal analysis was done on the structure using the same material properties and mesh settings previously described. The first five modes are shown in Figures 3.7 - 3.11.

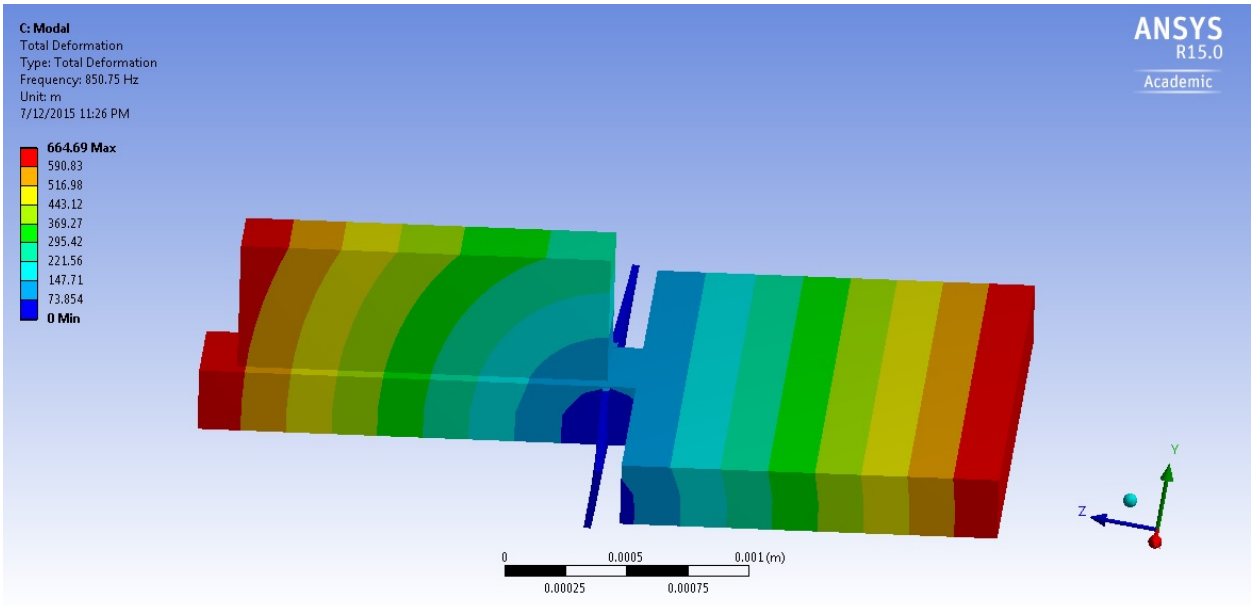

Figure 3.7: The first mode of the device predicted by ANSYS modal analysis. The predicted natural frequency of this mode is 850.75 Hz, closely matching previous calculations.

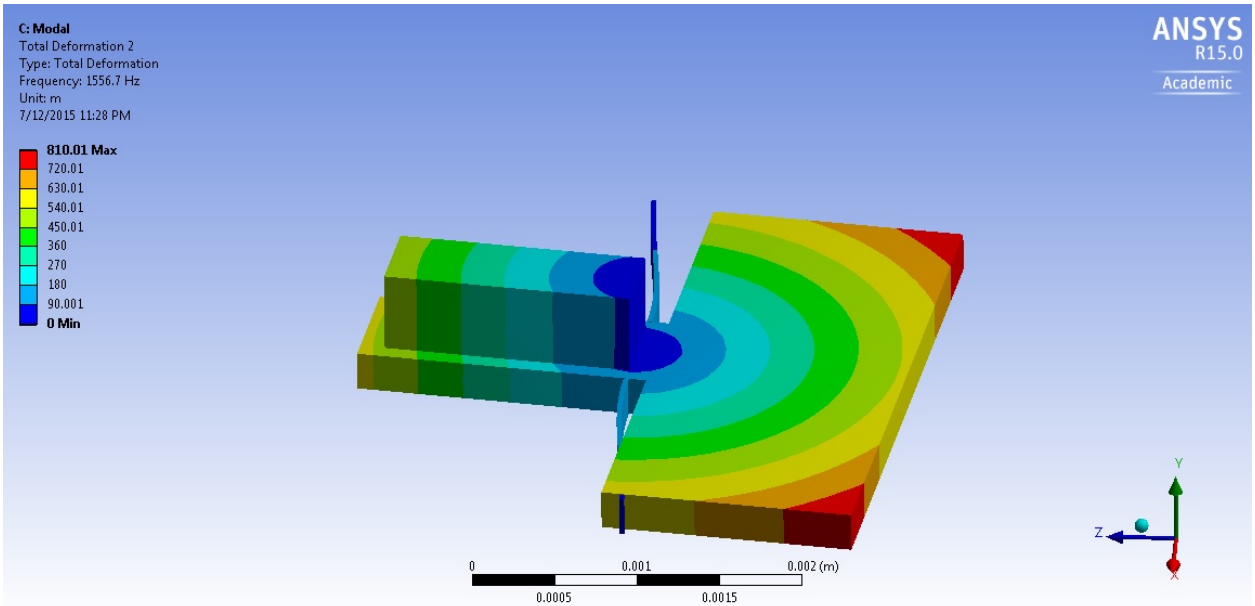

Figure 3.8: The second mode of the device predicted by ANSYS modal analysis. The predicted natural frequency of this mode is 1556.7 Hz.

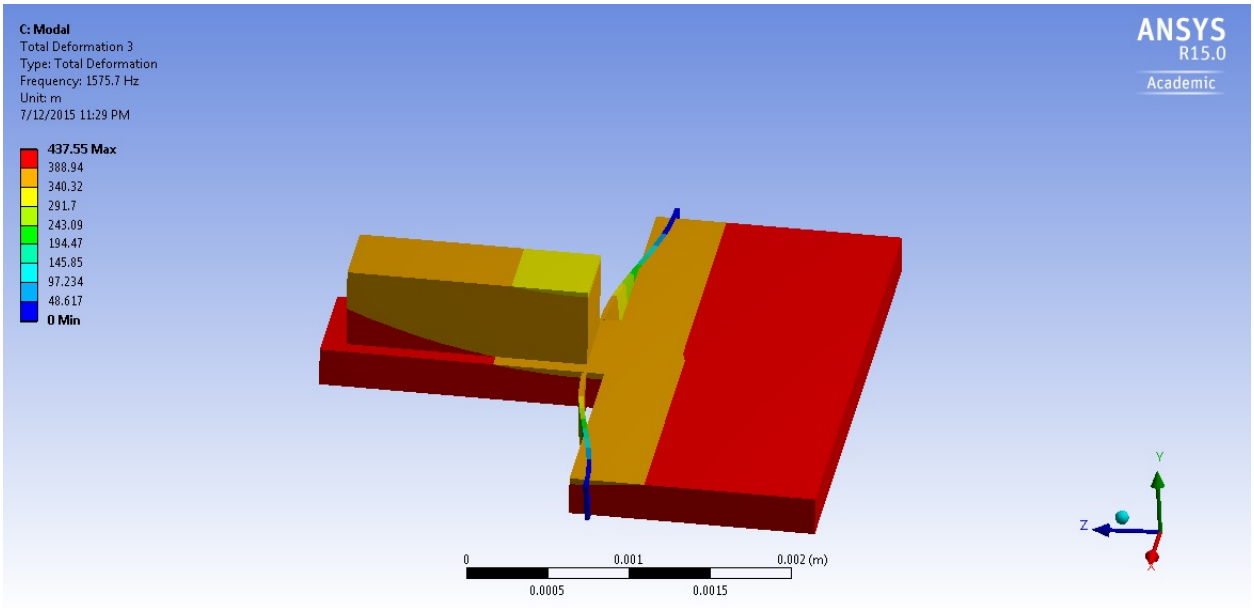

Figure 3.9: The third mode of the device predicted by ANSYS modal analysis. The predicted natural frequency of this mode is 1575.7 Hz.

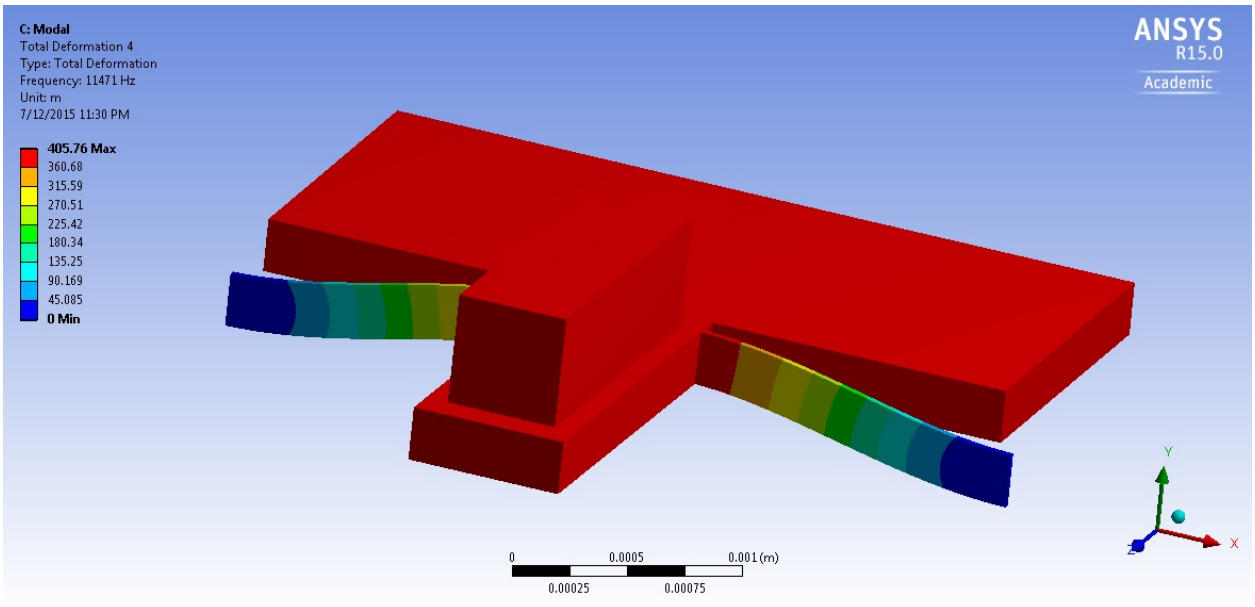

Figure 3.10: The fourth mode of the device predicted by ANSYS modal analysis. The predicted natural frequency of this mode is 11471 Hz, so it is unlikely to be a excited in actual operation.

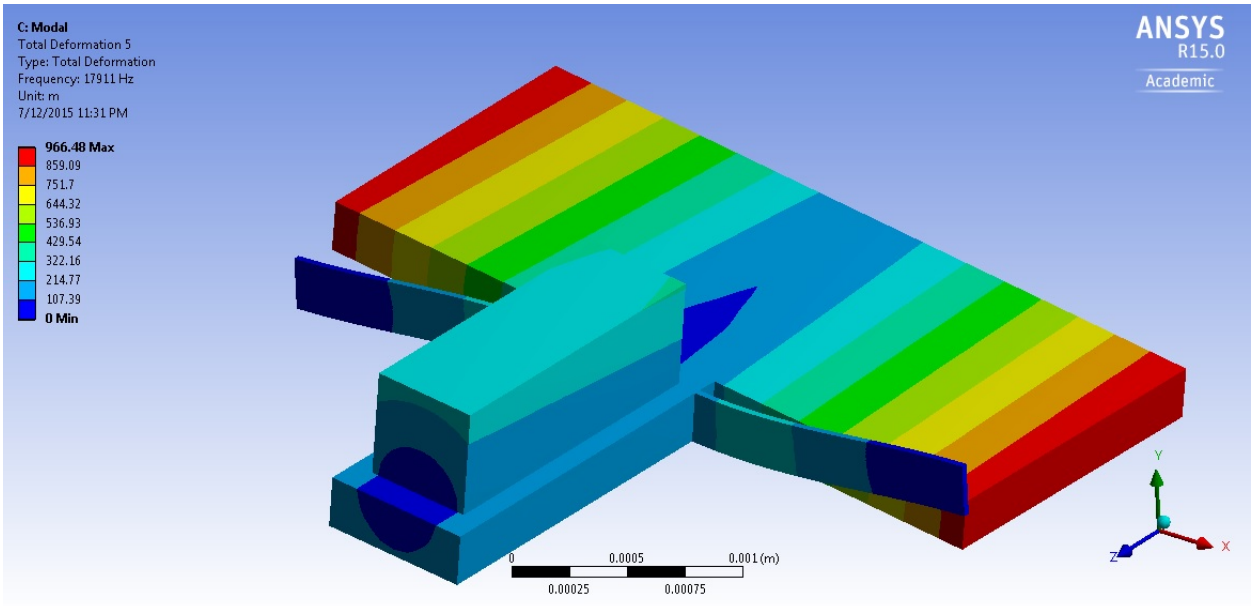

Figure 3.11: The fifth mode of the device predicted by ANSYS modal analysis. The predicted natural frequency of this mode is 17911 Hz, so it is unlikely to be a excited in actual operation.

The first mode predicted by ANSYS occurs at 850.75 Hz, and manifests as resonant motion about the torsion spring axis. This is the same mode described in Section 3.1.2, where it is predicted to occur at 828 Hz. Therefore, like the Static Structural Analysis, the ANSYS modal analysis predictions for the first mode are in close agreement with the theoretical calculations.

Figures 3.8 and 3.9 show the predictions for the second and third modes of the structure, which occur as cantilever motion by the torsion springs. These modes were not predicted by theoretical calculations, so the ANSYS results for these modes are of particular interest. Both of these modes occur at a low enough frequency (1556.7 Hz and 1575.7 Hz) to possibly be excited rather easily by ambient vibrations or off-sense-axis magnetic fields. However, as mentioned, a strength of this design is that planar motion of the torsionally-suspended plate should not significantly affect the output of the device, as planar motion does not change the capacitively-sensed gap between the torsionally-suspended top plate and the fixed bottom electrode.

Figures 3.10 and 3.11 show the fourth and fifth predicted modes of the structure. Both of these modes occur at a high enough frequency (11471 Hz and 17911 Hz, respectively) that they should not realistically affect the device's performance.

Overall, the results of the ANSYS analyses are in close agreement with the theoretical predictions made in sections 3.1.1 and 3.1.2, greatly increasing the confidence of these predictions. As the results of device testing presented in Chapter 5 show, the actual device performance departs significantly from predictions, so this increased confidence in device predictions is particularly helpful later in suggesting that the anomalous behavior of the actual devices is not due to inaccurate modeling of device behavior.

3.2 Additional Components

Besides the MEMS component shown in figures 3.1 and 4.1, the device required additional components to be a usable device. First, there had to be a bottom electrode for the variable, parallel plate capacitor, and something to electrically connect the device to the sensor electronics. These needs were met by bonding the MEMS device to the PCB pad pictured in Figure 3.12. The silicon MEMS device makes contact with the outer PCB pad, connecting it electrically with the sensor interface electronics. The inner PCB pad serves as the fixed electrode for the moving parallel plate electrode structure. The first batches of the devices constructed had the bottom side of the MEMS device metalized with copper on top of a titanium adhesion layer to decrease resistance and to form an ohmic contact to the silicon. However, it was later found that (liquid at room temperature) gallium-indium-tin solder was by itself sufficient for making an electrical contact between the silicon and the PCB pad. Additionally, highly doped p-type silicon was used for the device to help avoid forming a Schottky diode at the metal/silicon interface.

Additional silicon components are also required. Like the second prototype, a mechanical stop component was included to restrict the motion of the moving silicon plate in the presence of high external field strengths or high accelerations. Also as previously mentioned,

a cap is required to seal the device against external contaminants. To realize these components, three other types of silicon components were manufactured on the same wafer as the MEMS component. These other components are:

- A "mechanical stop" component, which prevents the torsion springs from over-ranging and being damaged when exposed to high field strengths or accelerations (the photolithography mask for this device is shown in Figure 3.13;
- A "spacer" component, two of which form the sidewalls of the cap over the device, and which is just a square piece of silicon with a rectangular hole where the NdFeB magnet will reside;
- A "cap" component, which is just a square piece of silicon that forms the roof of the cap.

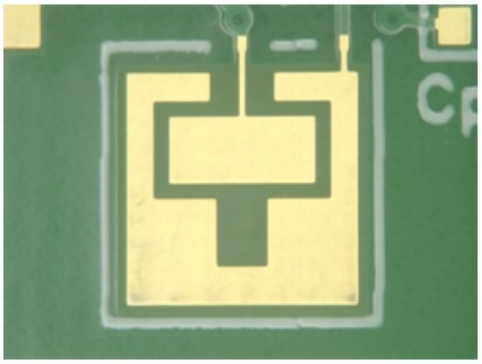

Figure 3.12: PCB pad that the MEMS device is bonded to.

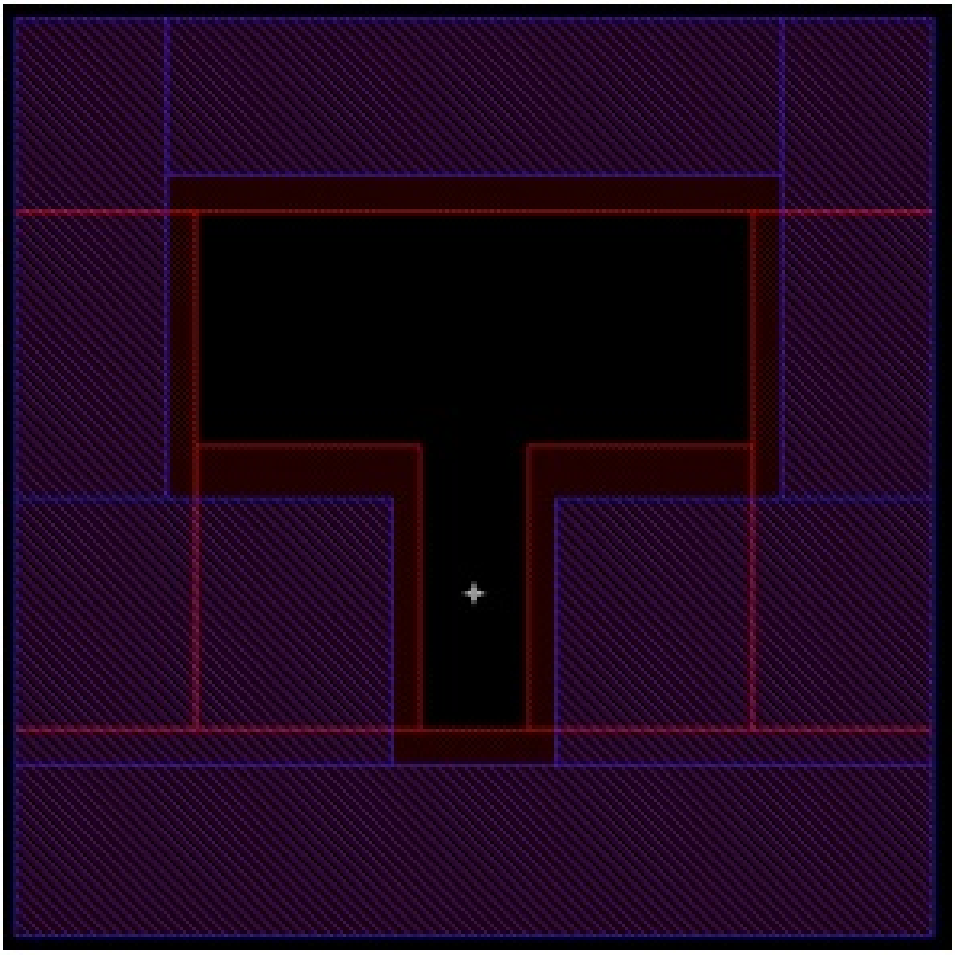

Figure 3.13: Photolithography mask layout for the Si mechanical stop component. Red (unhashed) are areas covered by the frontside mask and blue (hashed) are areas covered by the backside mask. Areas not covered by the backside mask are etched 5 µm - 15 µm. Areas not covered by the frontside mask are etched all the way through the wafer.

These components were stacked on top of the MEMS device, and bonded using epoxy. A cross-sectional illustration of the entire device, including all these components and the magnet, is shown in Figure 3.14. Note that as the magnet is approximately 500 µm tall, and the additional components were manufactured on the same 250 µm thick wafer as the MEMS component, then two "spacer" components are required to ensure that the magnet is fully free to move.

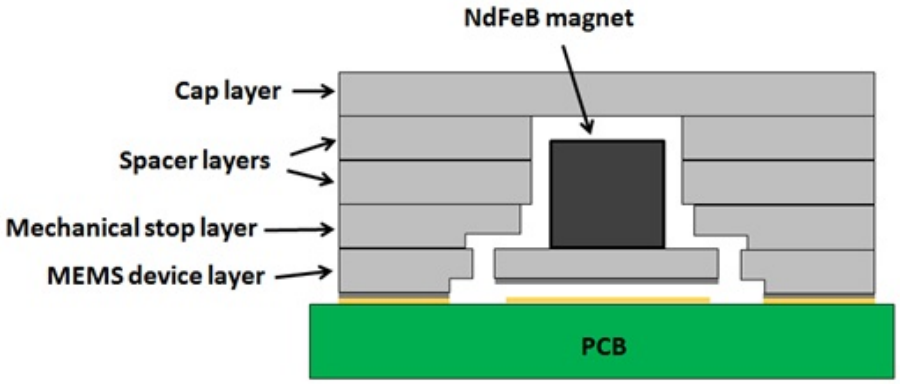

Figure 3.14: Cross section of a current sensor device.

The sensor electronics included on the PCB convert the variable parallel plate capacitance of the device into a variable frequency via a three-inverter, CMOS relaxation oscillator circuit. A circuit diagram is shown in Figure 3.15. The theoretical frequency of oscillation is given by

$$f = \frac{0.455}{R(C_v + C_p)} \tag{3.8}$$

where R is the value of the resistors used, C_v is the value of the variable capacitance, and C_p is the value of any capacitances (parasitic, gate, intentionally introduced, etc.) in parallel with the variable capacitance. A surface mount NC7NZ14 CMOS inverter IC containing three inverter circuits was used on each PCB. As mentioned earlier, the variable capacitance has a nominal value of 5.842 pF. Using a value of 2 MΩ for R, 5.842 pF for C_v, and 2 pF for C_p (2 pF is the specified gate capacitance of the NC7NZ14), then a predicted oscillation frequency of 29.01 kHz is obtained. Indeed, as shown later, most constructed devices have oscillation frequencies around 30 kHz.

The relaxation oscillator's output voltage is TTL compatible, and can be rapidly sampled by a microcontroller to determine the circuit's output frequency. If necessary, the

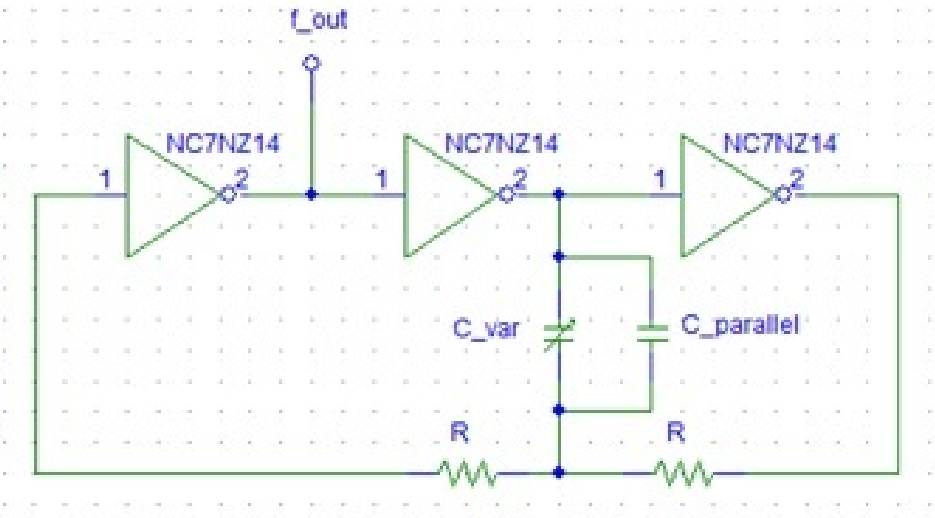

Figure 3.15: Circuit diagram of the relaxation oscillator circuit used to convert the variable capacitance of the MEMS components into a variable frequency voltage square wave signal. The three NC7NZ14 CMOS inverters are supplied on a single, surface mount integrated circuit.

oscillation frequency can be further reduced, either through additional ICs that provide frequency division/counters, or through increasing the resistance.

Chapter 4

Fabrication

4.1 Silicon Microfabrication

The silicon components were manufactured on 100 mm wide, 250 µm thick, ⟨100⟩, highly doped, p-type silicon wafers using surface micromachining techniques. The photolithography mask used for the MEMS components is shown in Figure 4.1.

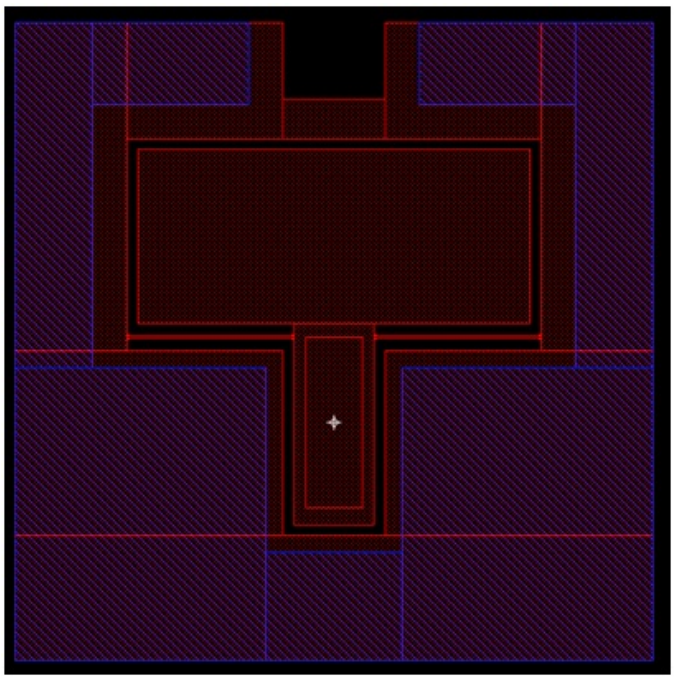

Figure 4.1: Photolithography mask layout for the MEMS components. Red (unhashed) are areas covered by the frontside mask and blue (hashed) are areas covered by the backside mask. Areas not covered by the backside mask were etched 8 µm in one batch and 15 µm in another batch. Areas not covered by the frontside mask are etched all the way through the wafer. The red rectangle centered on the crosshairs is not part of the pattern; it marks the location where the 1.5 mm X 0.5 mm X 0.5 mm NdFeB magnet is ultimately attached.

While fabricating the second prototype design, a problem was discovered with obtaining flat etched surfaces using the DRIE etch process. For the initial batches of second prototype

parts, DRIE was used for both the frontside and backside etches. While the high-aspect-ratio DRIE process was necessary for the small surface area, deep frontside etch, it was found that contamination from an unknown source was depositing small, scattered areas of etch-inhibiting substances and causing many small unetched areas to form on the large surface area, shallow backside etch. Figure 4.2 shows an example of this problem. These unetched areas are particularly troublesome because the backside etch is used to form the gap of the parallel plate, variable capacitance structure, and just one of these small, flat-topped unetched areas will render the device unusable, as it will short the parallel plates together and impede the motion of the MEMS structure.

The "problem" of high aspect ratio structures forming on the silicon surface during DRIE etching is a well-studied area [40, 41], and this roughness is frequently referred to as "grass" due to its very high aspect ratio (however, the defects produced in this device's case tended to approximate the shape of a mesa more than grass). The creation of this roughness has even been utilized as a beneficial effect for the creation of low-reflectivity silicon ("black silicon") for photovoltaic cells [42, 43] or for superhydrophobic surfaces [44, 45].

In an attempt to eliminate this problem, the DRIE etching machine was put through a conditioning and cleaning process. This significantly reduced the number of unetched areas, but enough remained to still render many devices (50% or more) unusable. Furthermore, according to [41], even in a fully cleaned chamber, sputtering of the walls and possibly ceramic wafer-gripping fingers may contribute significant amounts of etch-inhibitor contamination to the substrate surface. Therefore, significant changes to the etch process were required.

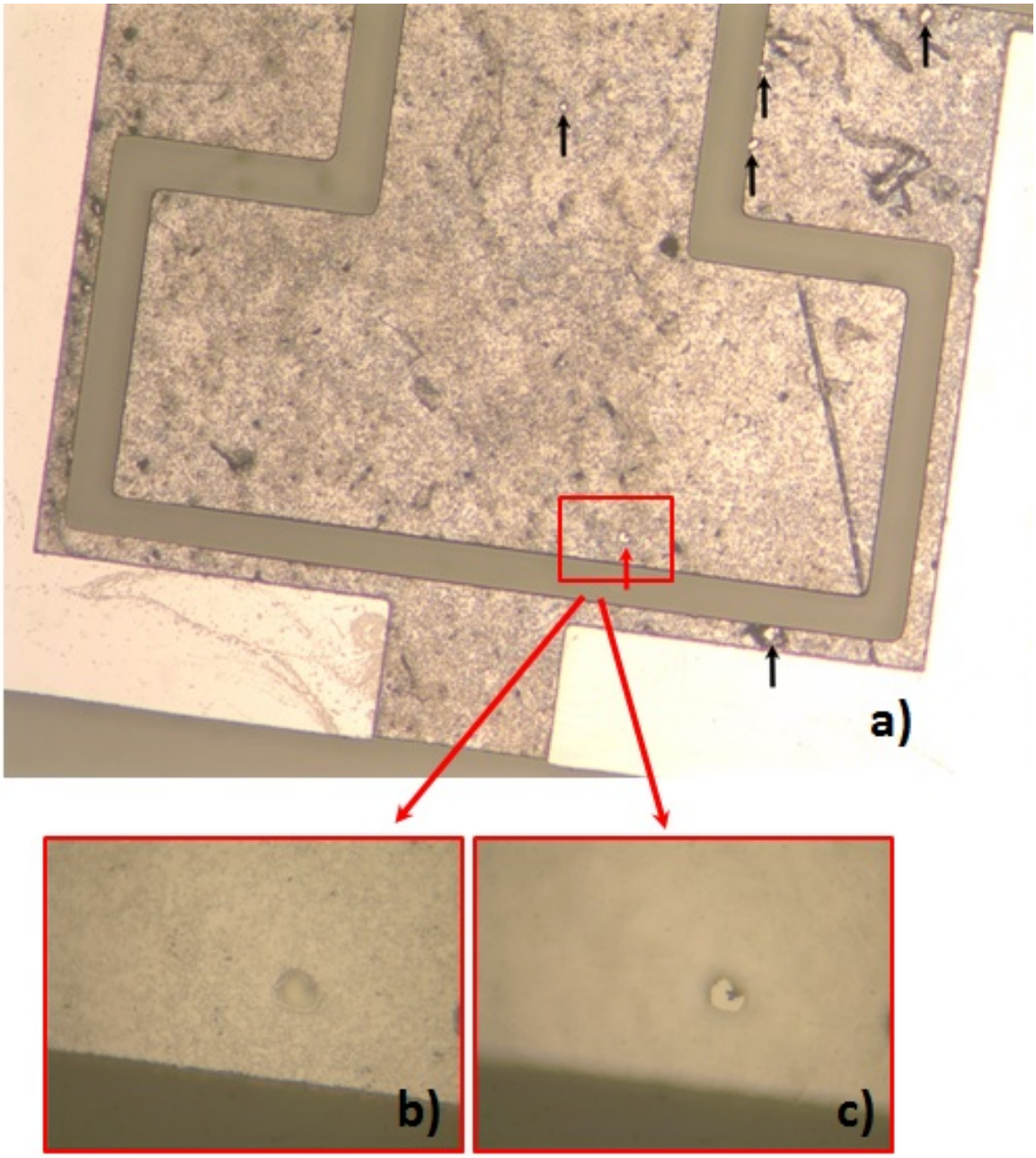

Figure 4.2: Unetched areas on the backside of a second prototype MEMS component. **a)** Small, flat-topped unetched areas are marked with arrows. **b)**Higher magnification view of the unetched area boxed and arrowed in red in a), with backside of the moving platform in focus. **c)** Same view as in b), but with the flot top of the unetched area in focus. The large amount of focus travel between the b) and c) demonstrates that this is a very tall feature.

The next step taken in an attempt to eliminate these high aspect ratio "mesas" or "grass" was to adjust the etch process the DRIE machine was using so that the passivation

step for the backside etch was eliminated (essentially transforming the etch into a pure SF_6 etch). It was thought that since these unetched areas had very high aspect ratios, and removing the passivation step should yield a nearly isotropic etch, doing so should rapidly eliminate the mesas in just a few etch cycles. This step occurred after the wafer had already been cleaned and stripped of photoresist, so the etch was applied to the entire backside surface. However, surprisingly, this proved to be only partially effective. (The DRIE etch machine does, in fact, have a program specifically for a pure SF_6 etch, but it was not discovered until much later.)

With it proving difficult to form large, uniformly etched areas for the backside etch with our DRIE etch machine, a wet, potassium hydroxide (KOH) etching process was tried instead. To form a mask for the KOH etch, the wafers were oxidized in a wet oxidation oven to form a nominally 0.7 µm mask oxide layer. The mask oxide was patterned, and the underlying silicon etched to a 5 µm - 15 µm depth, depending on the specific batch. With this etch complete, the mask oxide was stripped from both sides of the wafer. The results of this process were very satisfactory, with the highest defects on the backside etch being only on the order of about 1 µm. The defects that were present were usually square-shaped pits, aligned with the crystal plane due to KOH's affinity for etching the $\langle 100 \rangle$ silicon plane. These are inverted versions of the well-knock "hillocks" or "pyramids" that KOH etching is known to frequently produce on the silicon $\langle 100 \rangle$ crystal plane [46–48]. As these pits were at most about 1 µm deep, they did not interfere with the functioning of the device. Due to the success of this process, KOH etching was used for all subsequent batches (including the batches of the final design). The backside of a second prototype MEMS component that was etched with KOH is shown in Figure 4.3.

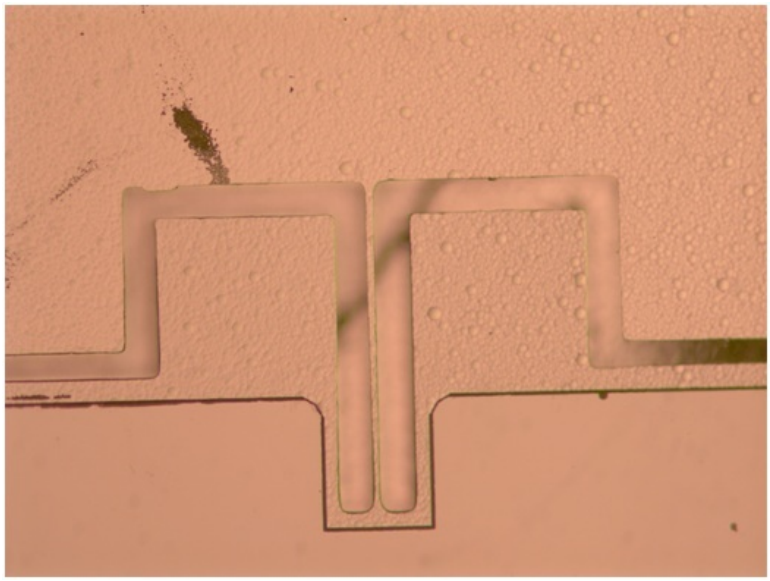

Figure 4.3: The backside of a second prototype design that was etched using KOH. Note the pitted surface; the pits are only on the order of a micron deep or less, and thus do not interfere with the functioning of the device.

An additional issue was encountered during the etch process. As the backside etch had to be done first, a 5 µm - 15 µm gap existed beneath each MEMS device as the topside etch was performed. As the topside etch nears completion, the torsion springs are left without good thermal contact to the backing wafer, allowing them to heat up, causing the photoresist mask protecting the top of the springs to rapidly etch away. As a result, despite a mask width of 30 µm, most of the torsion springs had final widths around 20 µm or less, with the springs on many of the MEMS components being lost entirely after only five or ten DRIE cycles of over-etching. However, most MEMS components were recoverable, though there was significant variation in torsion spring widths, and some torsion springs had defects that locally thinned them even further (down to as little as 10 µm). If there had been the opportunity to create any additional batches of devices, the oxide layer grown as a mask for the KOH etching would have been retained and used as an additional, hard mask layer during the frontside etch in an attempt to provide the torsion springs more protection against over-etching.

A more detailed listing of the silicon microfabrication steps used to fabricate the MEMS components for the current sensors is given in Appendix A. As the goal of providing these microfacation steps is to assist in the fabrication of any future device batches, this list of microfabrication steps includes the hard mask layer over the torsion springs, which was never used in any actual fabricated devices.

To provide a ohmic contact between the silicon and the agent electrically connecting the device to the PCB pad, the backside of the first several finished MEMS devices were metalized with 1000 Å of titanium followed by 4000 Å of copper. However, later experimentation showed that this metal layer was not necessary when using room-temperature-liquid Ga-In-Sn solder to form an electrical connection to the PCB pad.

4.2 Assembly

Once all the silicon components were manufactured, they had to be assembled into a working device. First, the MEMS component must be attached to the PCB pad, and a good electrical connection must be ensured. Several methods were tried for this. An important requirement for consideration was minimizing the distance that was added to the gap between the moving electrodes by layer width of the conductive material that was being used to electrically connect the MEMS component to the outer PCB pad. Any added gap distance will reduce the sensitivity and nominal capacitance of the device, and variations in this layer width will cause significant differences in device characteristics between different devices. To help minimize these issues, only very small amounts of this bonding/connecting material could be applied.

Solder paste was the first bonding and connecting material investigated. Very small amounts of solder paste were melted on the outer PCB pad. A device was placed on the pad, a small weight was placed on the device, and the structure was re-heated to reflow the solder and form both mechanical and electrical connections. It was quickly noticed that when the device was returned to room temperature, significant strains were exhibited by

the torsion springs. This was most likely due to the fact that the bond formed by the solder occurred around 150 °C, and at room temperature the stresses applied by differing coefficients of thermal expansion (CTE) between FR4 and silicon were enough to create a significant strain on the torsion springs.

The failure of solder paste forced alternative, lower-temperature techniques to be examined. Test devices were constructed using conductive silver epoxy and the previously-mentioned Ga-In-Sn solder alloy that is liquid at room temperature. The Ga-In-Sn liquid solder proved to be superior, as the conductive epoxy still had to be cured at 120 °C. To connect and bond a MEMS component with the Ga-In-Sn solder, very small amounts of the solder were placed on the PCB pad. The component was then carefully placed on the pad. To provide a mechanical bond to the PCB, small beads of a slow-curing epoxy were applied from the corners of the component to the PCB using a small diameter wire. The wire was then used to press the device firmly down to the pad, minimizing the gap distance, and the epoxy was then allowed to cure.

To complete assembly of the device, additional slow-curing epoxy was used to attach the magnet and silicon mechanical stop, spacer, and cap components. The second prototype design had shown that the magnet could be most easily attached by assembling the device under a widefield microscope using a small diameter wire. For example, to attach the magnet, the small diameter wire would be used to apply a tiny bead of epoxy on the moving silicon platform, and then be used to carefully push the NdFeB magnet into the correct position. The additional silicon dies/components were attached in a similar manner. The presence of the miniature NdFeB magnet required that non-magnetic tools be used. Once the cap over the device was in place, a thick bead of epoxy was applied around the perimeter to fully seal it from the environment. Figure 4.4 shows the various steps of device assembly.

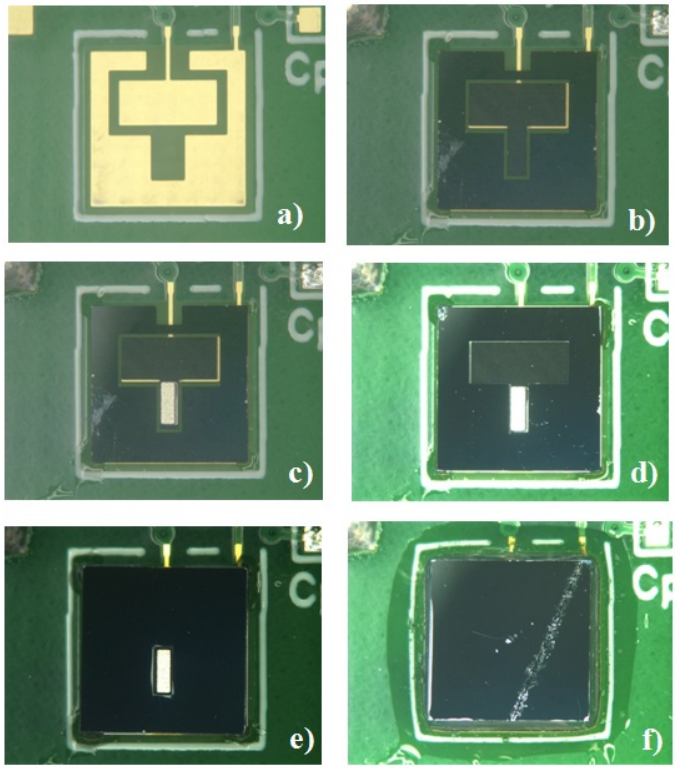

Figure 4.4: Assembling a current sensor device. a) The bare PCB pad. b) A MEMS component is connected and bonded to the pad. c) The miniature NdFeB magnet is epoxied to the moving MEMS plate. d) A mechanical stop component is added. e) Two spacer components are added. f) The cap component is added, and epoxy is applied around the perimeter of the device to environmentally seal it.

Chapter 5

Current Sensor Testing

Ten final design devices were constructed and tested. Most of the devices were constructed on a PCB that included two test traces for current to be passed through. A Lua script was written which utilizes Biot-Savart's law to calculate the magnetic field produced by a current trace (see Appendix C). Using this script, it was estimated that the top-most of the two test traces should yield an H-field at the device of approximately 41 A/m per A in the device's out-of-plane, sense direction. This trace was used in both DC and AC response tests. The layout of this PCB is shown in Figure 5.1.

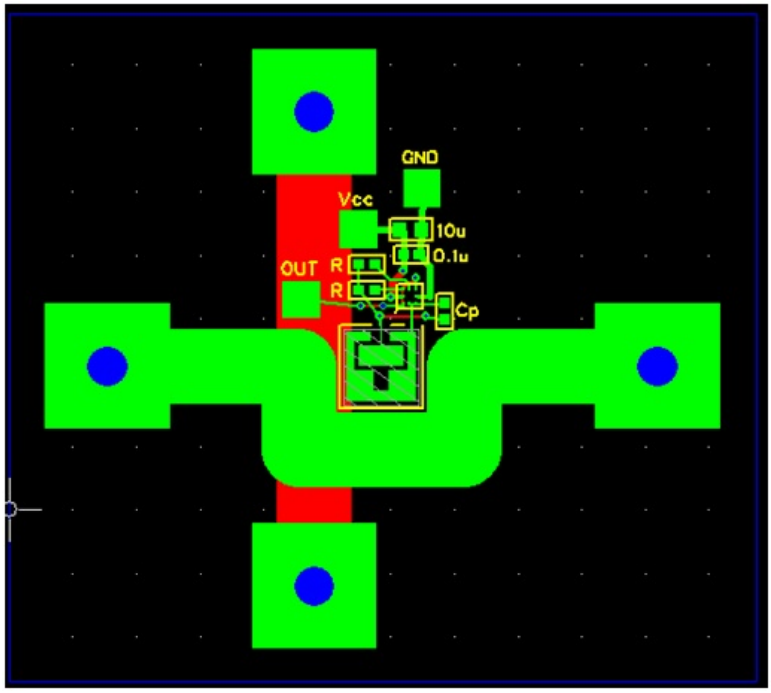

Figure 5.1: Layout of the PCB used in DC and AC response testing. The top trace (the one that forms a U-shape around the device) provides an H-field at the device of about about 41 A/m per A of excitation current, and was used in DC and AC response tests.

5.1 DC Test Results

The first devices assembled used solder paste to bond the MEMS device to the PCB, leading to the large differential CTE strains previously mentioned. These devices functioned, but the large strain on the torsion springs led to unreliable test results. Three devices with 8 µm nominal gaps proved suitable for testing, "Device #3", "Device #4", and "Device #7". While Device #3 was constructed with solder paste bonding, the strain on its torsion beams was low enough to allow DC response testing. Both Device #4 and Device #7 were constructed with the liquid Ga-In-Sn solder method, and provided reliable test results for both AC and DC testing.

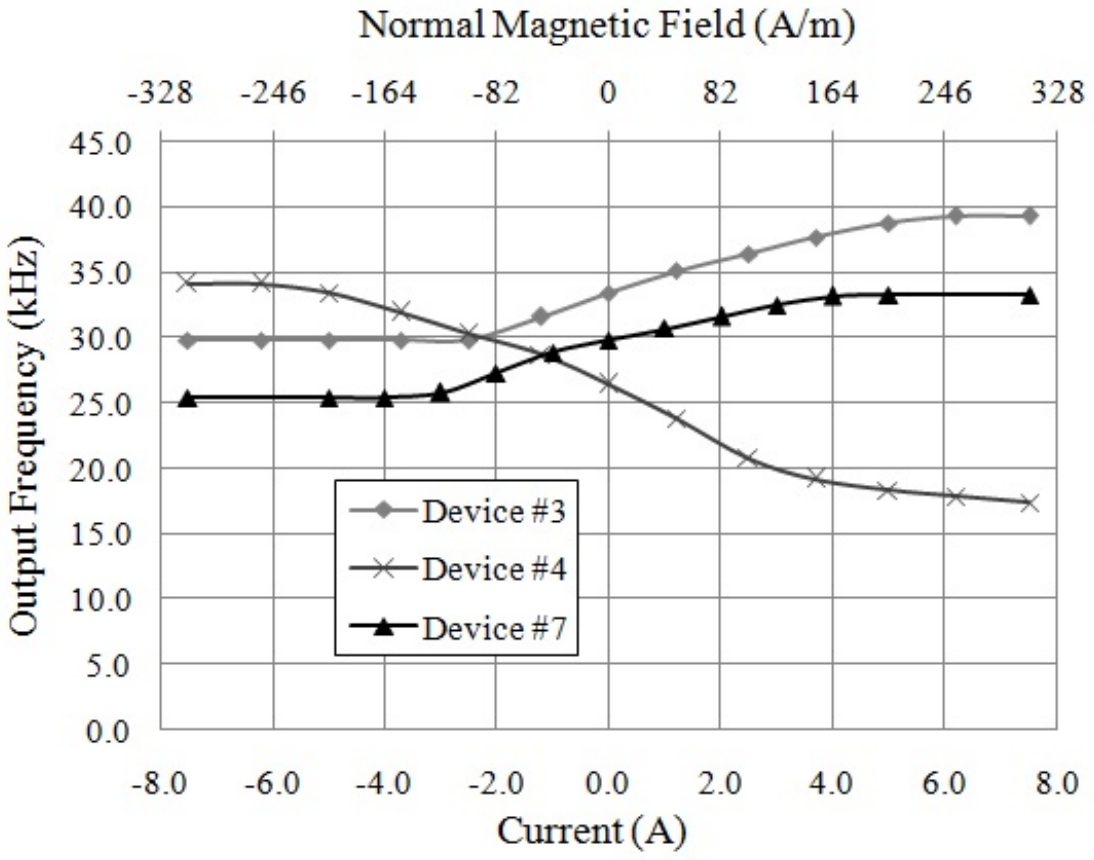

Figure 5.2: DC response of three current sensor devices. Device #4 exhibits a negative slope on its response curve because its NdFeB magnet was oriented in the opposite direction.

Two different responsivity metrics will be briefly discussed. "Current responsivity" will be defined as

$$r = \frac{dF}{dI} \tag{5.1}$$

while "normalized current responsivity" will be defined as

$$R = \frac{1}{F_o}\frac{dF}{dI} \tag{5.2}$$

where F is the relaxation oscillator output frequency, I is the current through the test trace (that produces about 41 A/m/A at the device under test), and F_o is the relaxation oscillator output frequency when zero current is applied to the test trace (the "nominal" frequency). From the data given in Figure 5.2, for devices #3, #4, and #7, the current responsivities are 1460 Hz/A, -2040 Hz/A, and 900 Hz/A, respectively, and the normalized current responsitivities are 0.044/A, -0.077/A, and 0.030/A, respectively. Device #4 had its magnet oriented in an opposite direction from the other devices, which is why its response curve has an opposite slope from the others.

Comparing Figure 5.2 and the responsivity of these devices to the predictions made in Section 3.1.1 shows that device behavior departs very significantly from predictions. Recall that in Section 3.1.1, the current responsivity of the devices was predicted to be about 250 Hz/A; the actual device current responsivity is between four and eight times this predicted value. Also note that all of the devices come into contact with the mechanical stop or the bottom electrode at an H-field value of around 150 to 250 A/m (or approximately 3.5 A - 6 A). Recall from Section 3.1.1, it was predicted that for an 8 µm-gap device positioned near a test trace producing 41 A/m/A, a current of 47 A (corresponding to an H-field of around 1900 A/m) would be required to bring the device into contact with the stops. Thus, assuming no contaminants are impeding the motion of the MEMS components, and that the width of the electrical contact layer (which would add to the gap distance) is negligible,

then the MEMS components are achieving about 8 µm of motion with about ten times less H-field than predicted.

As discussed in Section 4.1, the torsion springs were considerably over-etched, reducing their widths from 30 µm down to approximately 20 µm - though there was considerable variation from device-to-device. As the torsion spring constant is proportional to the width of the torsion spring cubed, springs 20 µm wide are about 3.4 times more compliant than those that are 30 µm wide. Therefore, over-etching can account for much of the higher-than-expected responsivity of the tested devices. Torsion springs that were 15 µm wide, and therefore eight times more compliant than 30 µm wide springs, would be able to account for all of the higher-than-predicted responsivity; however, no devices with springs that thin were measured (but that said, not all devices had their springs measured before construction).

One alternate explanation that might be proposed for at least some of the devices' over-sensitivity compared to predictions could be that an incorrect value for the shear modulus of silicon was used during theoretical predictions. Within the $\langle 100 \rangle$ crystal plane, silicon's shear modulus varies from between about 50 GPa and 80 GPa [49]. However, as 60 GPa was used during calculations, then the maximum deviation from predictions that could be expected from an incorrect value of shear modulus would be about 25%.

Also of note in the DC testing results is the large variation between different devices; Device #4 is over twice as responsive as Device #7, with Device #3 falling in-between. Perhaps this large variation could be expected due to both the imprecise nature of manual assembly, an electrical contact layer of non-negligible width between the MEMS component and the PCB, and by varying torsion spring widths between different devices. Recall that not all torsion springs were over-etched by the same amount, and a few had additional defects that locally thinned their springs by even more. It might also be possible that the remnant magnetization between the individual magnets varied significantly, however, there was no reason to suspect this was the case.

While the DC testing does reveal some variability among the devices, it also shows that the devices function correctly and the theoretical predictions made of their performance were close enough to enable the proper selection of design parameters for a practical device. While the devices are more sensitive than predicted, it is important to remember that the location of the devices on the 12 V - 1 V POL converter was never determined, and therefore, the actual sensitivity that would be required was never ascertained.

5.2 AC Test Results

While these devices were intended to be DC current sensors, it is still important to know their response time and cutoff frequency. After DC testing was completed, three more devices were constructed. While these devices lacked backside metallization, with electrical contact between the PCB pad and the silicon MEMS component being made entirely through Ga-In-Sn solder, this did not in any way appear to affect their performance.

To test their AC response, a Darlington pair BJT NPN power transistor was obtained and used in the common-emitter configuration to create a voltage-to-current amplifier. A circuit diagram is shown in Figure 5.3. The Darlington pair converts a very small base current into a very high collector current through the multiplication of the β's of the two internally-connected BJTs. Ignoring the voltage drop across the base resistor (which should be negligible with a very high effective β and low enough base resistance), the voltage on the emitter is approximately the voltage output by the signal generator minus two base-emitter voltages, about 1.4 volts. This voltage is dropped across the low emitter resistance to transform it into a high current, and the test trace shown in Figure 5.1 is connected to the collector. A low output impedance voltage source is used to supply high current to the circuit. In most tests, the signal generator was adjusted so that the current waveform would assume a trapezoidal shape, which simplified frequency measurements of the relaxation oscillator's output and did not produce noticeably different results than if a sinusoidal (or

even square) current waveform was used. The response was determined by comparing the high-current output frequency with the low-current output frequency.

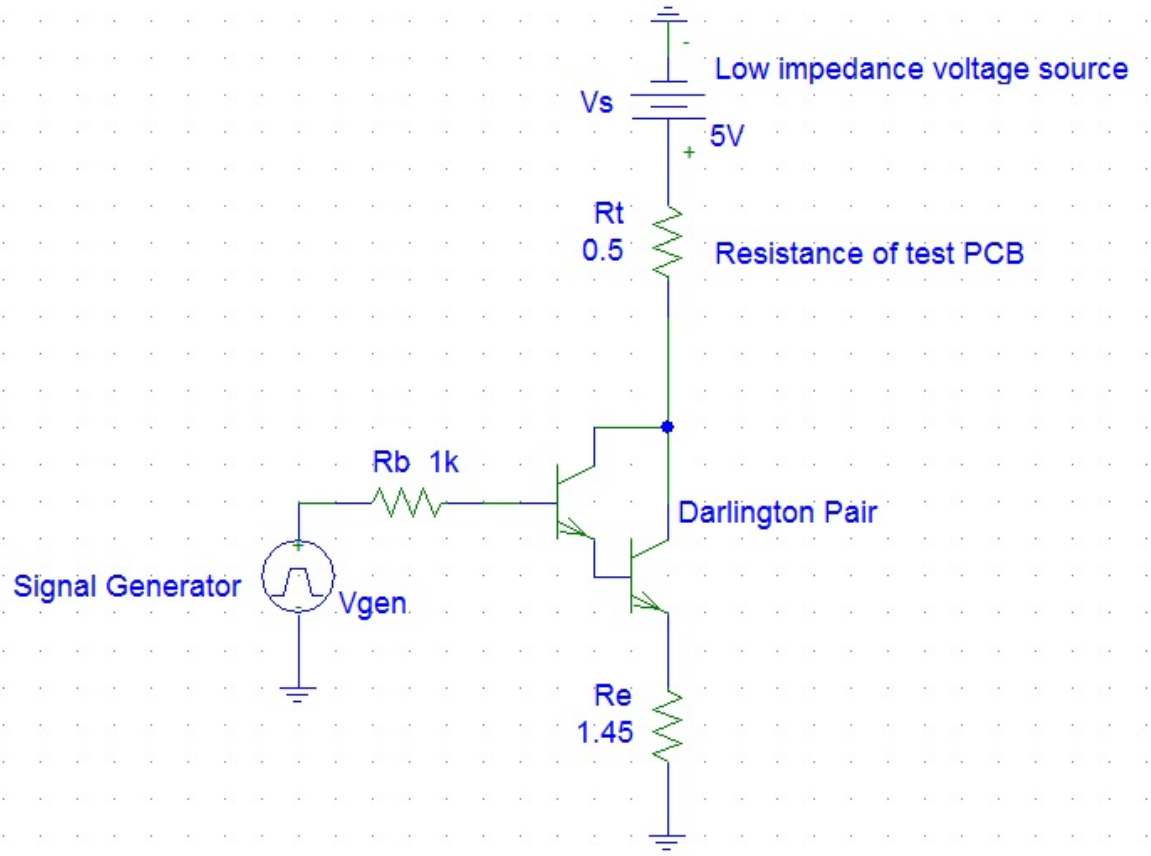

Figure 5.3: Circuit used to test the AC response of the devices. The test PCB is connected to the collector of the Darlington pair.

To further assist in frequency measurements of the relaxation oscillator's output, the output of the relaxation oscillator was fed into a 4 bit binary counter IC. This effectively divided the frequency by either two, four, eight, or sixteen, depending on the place value of the binary counter bit that was being viewed on the oscilloscope. This was especially useful when very low current frequencies were being tested due to the fact that the waveforms of both the relaxation oscillator's divided frequency output and the excitation current were being viewed on an oscilloscope simultaneously, which limited the precision with which the oscilloscope could measure the higher frequency signal.

One downside of this configuration is that it is not bidirectional; current can only flow into the collector of the Darlington pair. However, this merely applies a DC offset to the varying magnetic fields produced. While this is not optimal, this DC offset deflection of the torsion springs should not be large enough to significantly affect the characterization of their AC response.

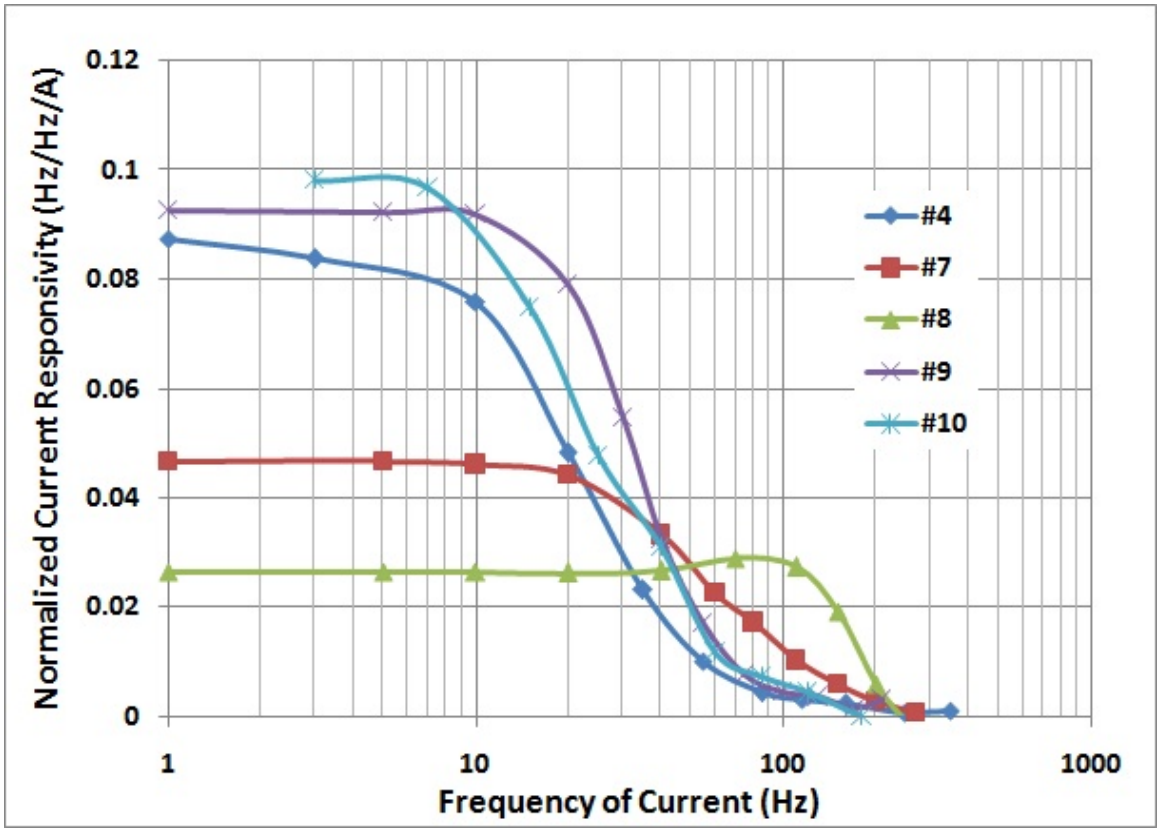

Figure 5.4: AC response of five devices. Determined by dividing the difference between the maximum and minimum oscillating frequency by the nominal oscillating frequency and dividing by the peak current.

A total of five DC current sensors had their AC characteristics measured in the manner described above. These measurements are presented in Figure 5.4. Like the DC test results, the devices did not have uniform and consistent comparative performance, as a very large variation in cutoff frequency between different devices is readily apparent. The lowest frequency cutoff is for Device #10, which cuts off around 10 Hz, while Device #8 has the highest-frequency cutoff, near 150 Hz. A large variation in DC sensitivity is also seen, with

Device #8 being the least sensitive and Device #10 being the most sensitive. Again, it seems logical to attribute this to the imprecise nature of hand assembly and variable electrical contact layer and torsion spring widths. Variable NdFeB magnet strengths does not seem like a likely explanation, though it should be noted that the strengths of the NdFeB magnets were never directly tested.

As detailed in Section 3.1.2, a simple treatment of the device as a torsional spring-mass-damper system suggests a natural frequency of around 400-800 Hz, and after the natural frequency, the device output should decrease at the rate of -40 dB/decade. However, much lower cutoff frequencies are observed in actual testing. That said, a rough correlation between sensitivity and cutoff frequency is observed in that more sensitive devices (which should have thinner, more compliant torsion springs) do tend to have lower frequency cutoffs than less sensitive devices. Additionally, of significant note is that very little or no resonant peak is observed, though Device #8 does appear to have a slight rise in its normalized current responsivity at around 80 Hz. Both the low frequency cutoffs and the apparent lack of a resonant peak suggests that the devices may be heavily over-damped and not correctly represented by a simple spring-mass-damper system. A likely cause of this damping is air resistance; the large moving flap on the torsionally-suspended platform must displace a large volume of air when it's in motion, and there is limited space within the device itself for that air to move. As additional testing in Section 5.3 shows, it does indeed appear to be the case that these devices are over-damped by trapped air.

While the AC test results show a large variability between individual devices, they also demonstrate that the devices have a high enough cutoff frequency to serve as suitable DC current sensors. The variability in test results likely results from different torsion spring widths and possibly by variations inherent in the imprecise nature of hand assembly of the devices' components. Changes to fabrication and/or assembly, such as using an additional oxide hard mask layer to protect the torsion springs during DRIE etching, could possibly address these issues and lead to more consistent device performance. Regardless, both the

DC and AC tests demonstrate the the devices successfully meet the requirement of a non-invasive, efficient, and miniature MEMS DC current sensor.

5.3 Magnetometer Testing

An investigation of the current sensor's operation as a magnetometer was undertaken. To evaluate the current sensor's responsiveness to static magnetic fields, a three-turn, square coil was created with a side length of 100 cm. The magnetic flux density created at the center of the coil by a current flowing through the wire for this geometry is known analytically to be

$$B = 60\sqrt{2}\frac{\mu_o I}{\pi} \tag{5.3}$$

where I is the current in amps, μ_o is the free-space permeability, and B is the flux density in Teslas. The coil was placed on a plastic stand (a 4" silicon wafer holder) to elevate it above any ferromagnetic objects that might couple into the flux paths, and a device was placed in the center of the coil. The coil was excited with a DC current and precise measurements were made of the output frequency of the current sensor under test using a BK 1823A frequency counter. It was immediately noticed that moisture on the PCB caused a very large variation in output frequency of the device, possibly due allowing the conduction of currents along the surface of the PCB or perhaps though changing the permittivity along the surface. Additionally, just standing near the test setup changed the output frequency, probably due to electric fringing fields coupling to the human body. In order to further isolate the device under test, a copper box was fashioned out of thick copper foil, placed around the device and coil, and grounded. This prevented fringing field effects from affecting the results (the copper box was thicker than the skin depth of the operating frequency of the current sensor's relaxation oscillator output), but a slow-varying change in the frequency remained, possibly due to moisture on the board. To try to remove this last source of variation, the test setup

was moved into a vacuum chamber and the pressure was reduced to <0.1 Torr. This test setup is shown in Figure 5.5.

After one to two hours under vacuum, the output frequency of the device under test would stabilize. The BK1823A frequency counter was set to update/refresh the measured frequency at a rate of 10 Hz, and five devices were tested in this configuration, as shown in Figure 5.6. The tests results demonstrate that the devices are highly responsive to external magnetic fields, and that the frequency variation is linear about the zero-field point. The nominal frequency for the relaxation oscillator varies from device to device, but is typically around 30 kHz. The magnetic responsivities of the devices range 14.7 Hz/μT for the least responsive, Device #8, to 46.1 Hz/μT for the most responsive, Device #9. While the level of frequency jitter on the output was not precisely recorded, it was visually estimated to be between 0.5 Hz and 1 Hz. Obviously this is not an accurate method for estimating frequency jitter (and the bandwidth of the jitter measured by the frequency counter is not known), but it is probably not off by more than a factor of two or so, meaning that the noise floor of the devices was probably less than 20 nT for the most responsive devices in this experimental setup. Even though these devices were not optimized for the magnetometer application, a noise floor of less than 20 nT is already significantly better than the noise floor of many commercially-available Hall-effect magnetometers [50, 51].

For devices with torsion springs 15 μm wide, the compliance of which the more flexible of these torsion springs appeared to mimic (such as Device #9 and Device #10), an external field of 20 nT leads to a displacement at the end of the suspended plate of about 5.1 angstroms and an output frequency change of 0.74 Hz, which is consistent with the amount of jitter seen on the output frequency.

As the devices were sensitive to sub-micro-Tesla fields, special care had to be taken that the elevator in the building was on a specific floor when the test was undertaken. The elevator was located roughly 8 meters away from testing location, and when it was on the same floor as the testing location, a 300-400 nT field change was detected. Additionally,

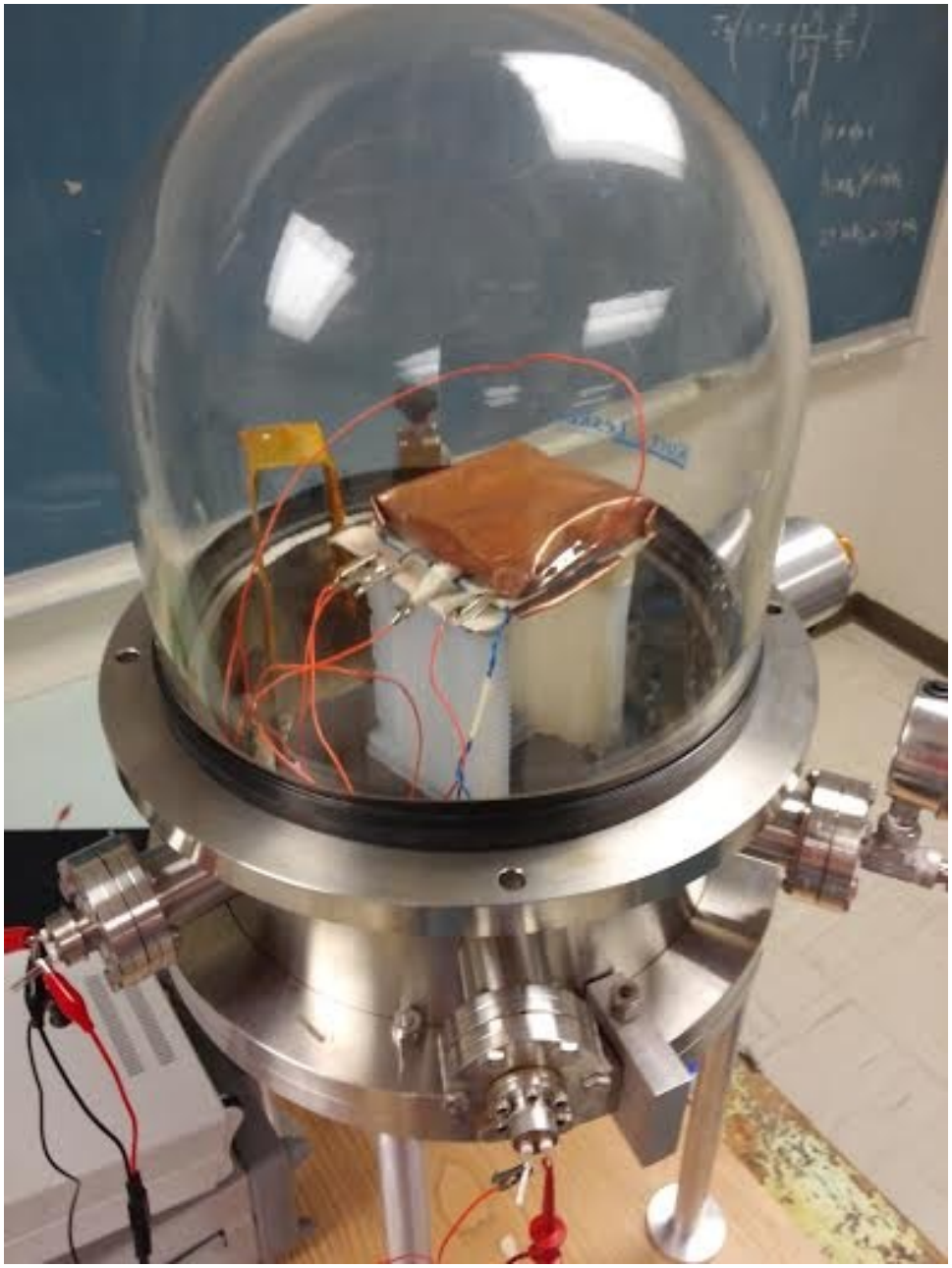

Figure 5.5: The vacuum chamber set up to test the current sensor's operation as a magnetometer. The 4" three-turn square coil and magnetometer is underneath the grounded copper shield on top.

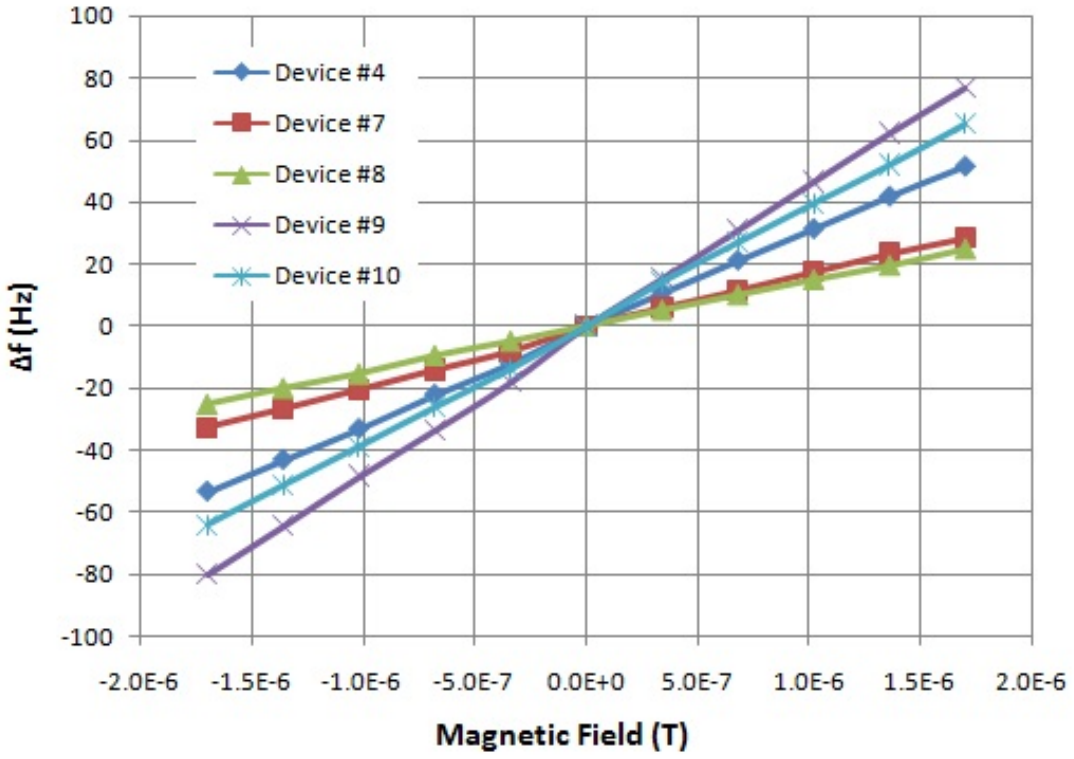

Figure 5.6: The change in the relaxation oscillator output of five devices in response to a DC magnetic field.

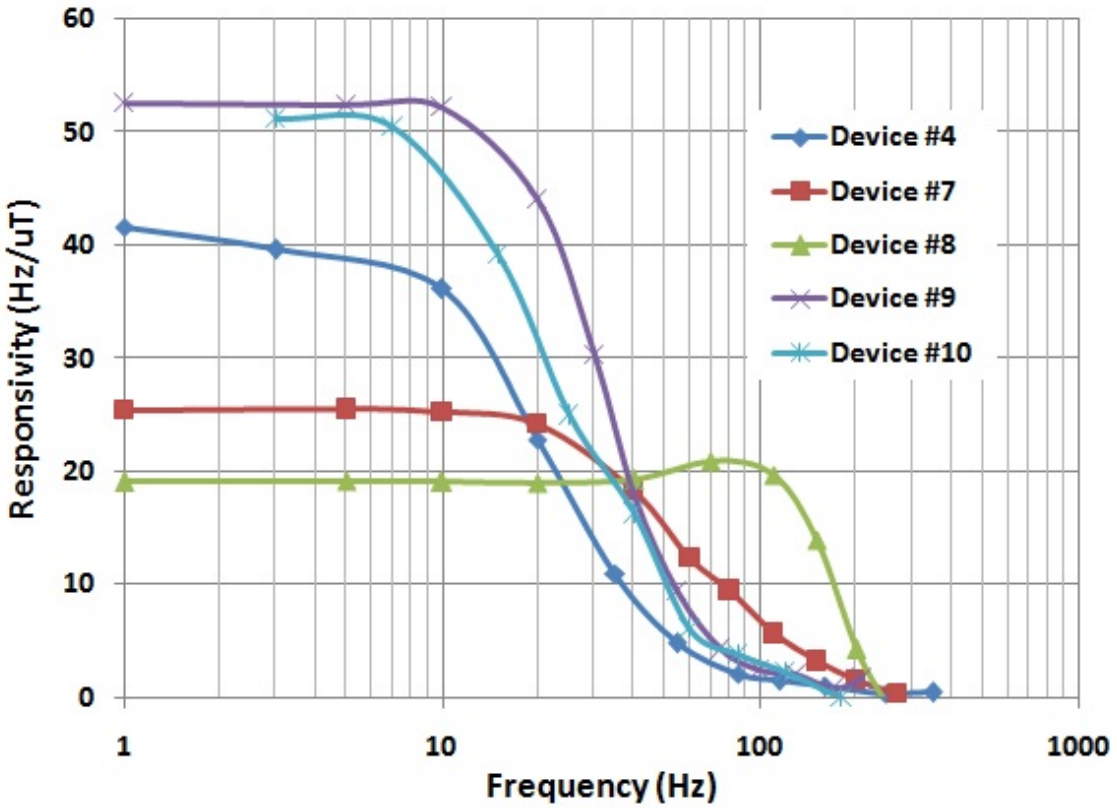

Figure 5.7: The responsivity of five devices excited by an AC magnetic field.

the elevator door being open vs. closed appeared to create a change in field of perhaps about 15-30 nT, though this signal was almost buried in the noise and only seen on the most sensitive devices.

While the devices display good responsivity to magnetic fields, they vary greatly in their individual performance. This is likely due to varying torsion spring widths caused by varying levels of over-etching, as well as the imprecision inherent in manual microassembly.

Additionally, the AC response of the devices as magnetometers was captured when the devices were tested as current sensors as described in Section 5.2. This data is re-graphed as a magnetometer AC response and is shown in Figure 5.7.

Again, these results demonstrate that the cutoff frequencies exhibited by the devices varies greatly among the five devices tested, and fall within the range of 20-150 Hz, well below the predicted value of 830 Hz for 30 µm wide torsion springs, and even below the 457

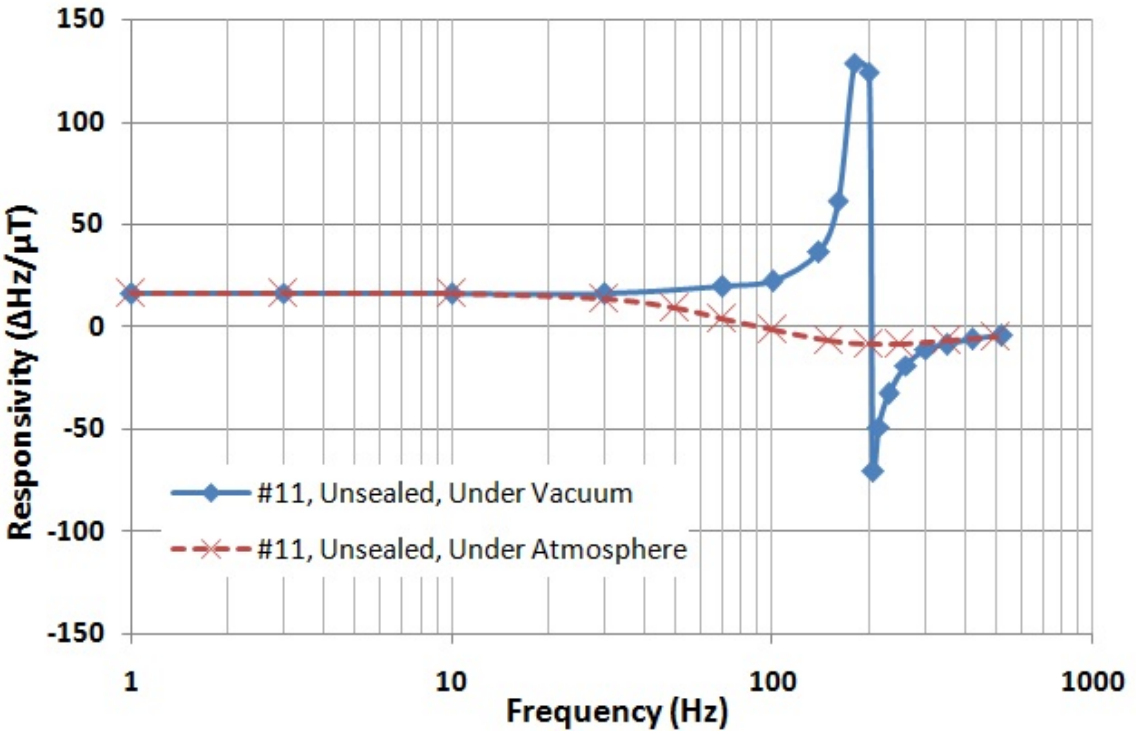

Figure 5.8: The responsivity of Device #11 under vacuum and under atmospheric pressure.

Hz predicted for 20 µm wide springs. However, the frequency responses of the devices also lack a resonant peak, indicating that the system is critically damped or over-damped. As previously mentioned, a likely culprit for damping is the air trapped inside the package. To verify this, two devices, both with for 20 µm-wide springs, were assembled without the final ring of epoxy applied around the device edge that normally would seal air inside it, leaving the internal spaces of the devices open to the vacuum. The frequency responses of these two unsealed device ("Device #11" and "Device #12") were measured under vacuum and under one atmosphere using the square coil test setup previously used for the DC magnetometer testing. These results are shown in Figure 5.8 and 5.9.

It is important to remember that the data taken in Figures 5.8 and 5.9 was taken at a specific phase of the current sensor's response. As said earlier, the response is determined by comparing the frequency output of the device under test at the time when it is subjected to peak field and minimum field. Thus, the device's response is measured at 0 degrees of phase, implying that only the real part of the response is measured. Comparing the measured

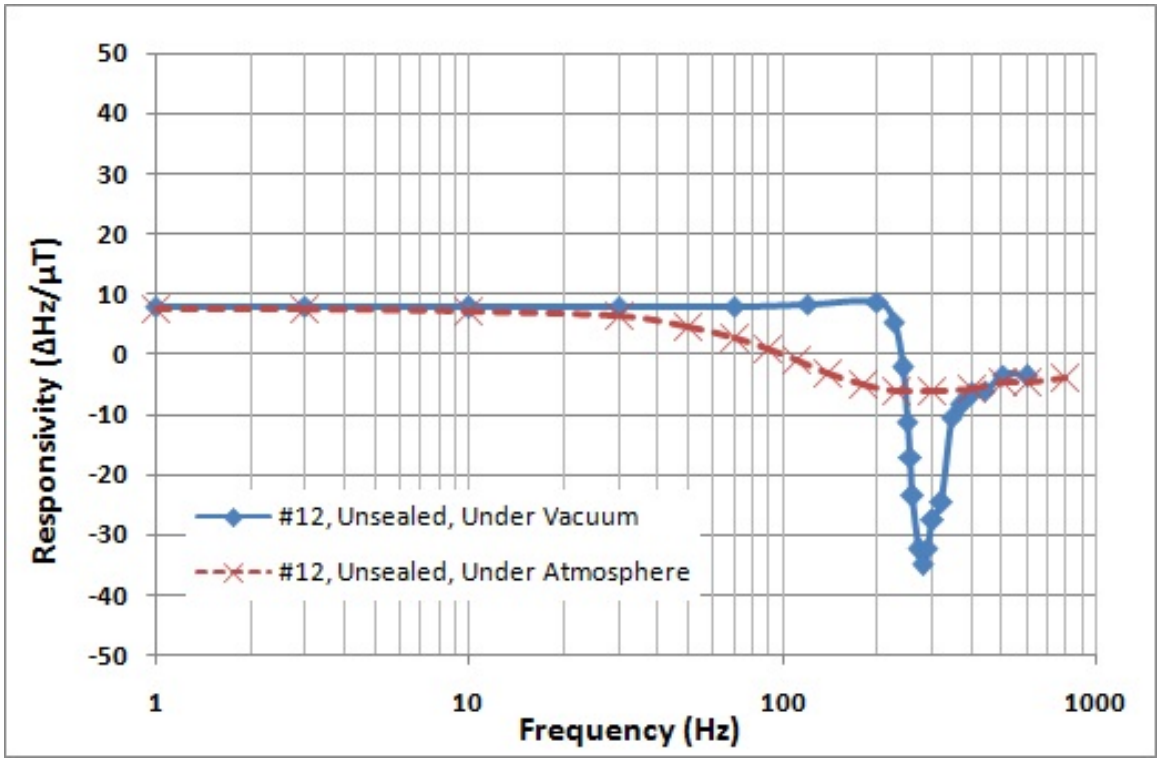

Figure 5.9: The responsivity of Device #12 under vacuum and under atmospheric pressure.

devices' behavior under vacuum to Figure 3.4, the real part of the simple torsional SMD transfer function, shows a strong resemblance, especially for Device #11. However, the observed natural frequency of both devices tested is much lower than the predicted 457 Hz for 20 µm-wide springs. Additionally, when tested under atmosphere, both devices behaved similarly to devices sealed under atmosphere. However, the 180 degree phase change at the natural frequency was observed in the unsealed devices, which was NOT observed in the devices sealed under atmosphere. This is curious, and it is perhaps due to the fact that as the unsealed devices force the movement of air within their packages, that moving air is not, in fact, enclosed and trapped within the package, and is free to escape and radiate acoustically. No sound was heard radiating from the devices under test, however.

Figure 5.10 shows that Device #11 closely resembles the response of the real part of a torsional SMD assuming that $k_\phi = 1 \times 10^{-5}$ N·m/rad, $c = 7 \times 10^{-10}$ N·m/rad/s, and $I = 6.04 \times 10^{-12}$ kg·m. However, the value of k_ϕ required to match the response is much

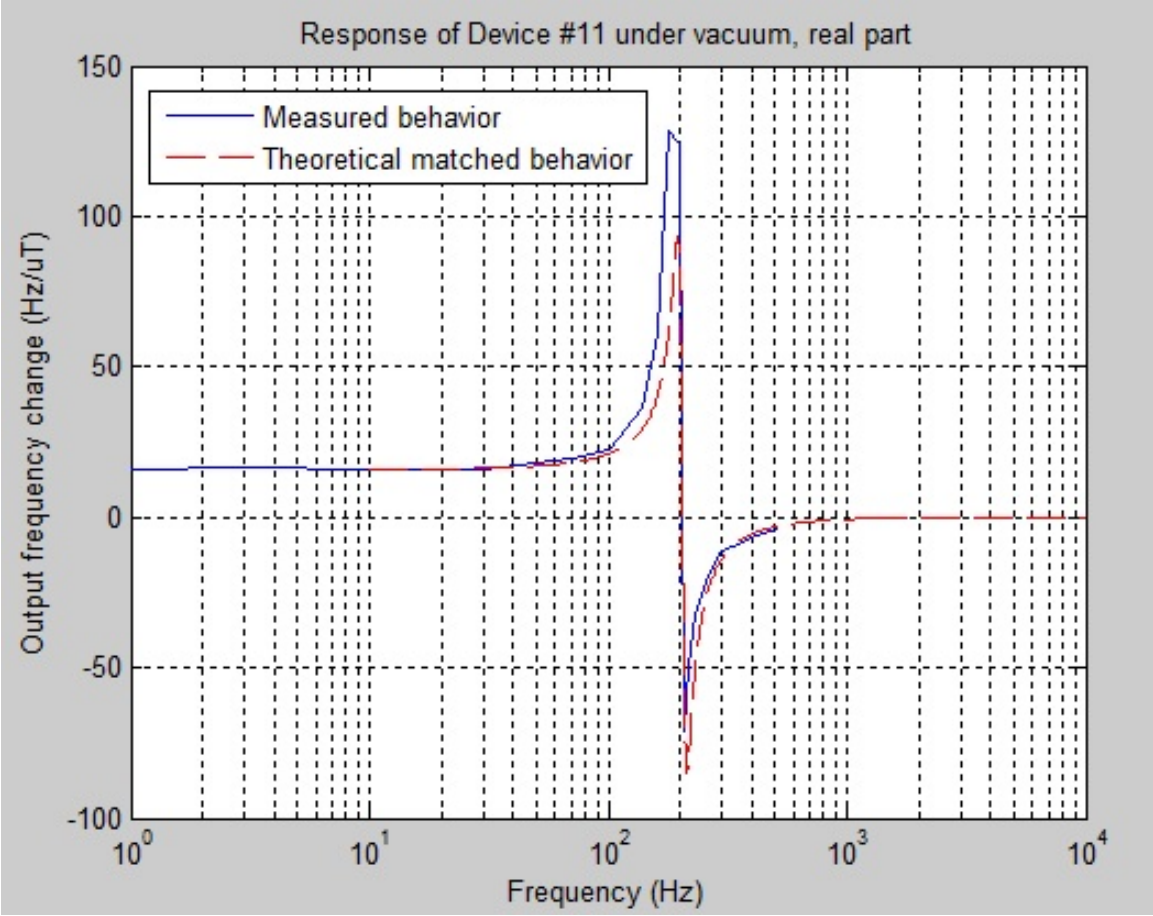

Figure 5.10: The responsivity of Device #11 under vacuum, compared with the real part of a torsional spring-mass-damper with $k_\phi = 1 \times 10^{-5}$ N·m/rad, $c = 7 \times 10^{-10}$ N·m/rad/s, and $I = 6.04 \times 10^{-12}$ kg·m

lower than the value of 4.98×10^{-5} N·m/rad that is predicted for 20 µm-wide springs. While the springs are far more compliant than predicted, this is consistent with the other tests conducted on the devices.

Chapter 6

Conclusion and Future Work

6.1 Conclusion

A MEMS DC current sensor was developed to sense phase currents in a 12 V - 1 V DC POL converter. The current sensor utilizes a NdFeB magnet attached to a torsionally-suspended silicon platform, as detailed in Chapter 3.1, which displaces about the torsion beam axis when an out-of-plane external magnetic field is applied. As discussed in Chapter 5, the current sensor operates in the manner expected, but has a much higher sensitivity and much lower cutoff frequency than predicted. The current sensor is also shown to perform well as a sensitive magnetometer. However, a large variation in current sensor responsivity is observed, with the most likely cause for this variability being imprecise fabrication (such as variations in torsion beam width) and assembly.

Unfortunately, funding for the 12 V - 1 V POL voltage converter ended in December 2013, before the current sensor could be integrated into the voltage converter phases. While the current sensor as constructed was more sensitive than planned, it was unknown what the actual sensitivity needed to be. As the voltage converter stages were a work in progress, the actual values of the magnetic field created by current flowing through the converter were never measured or modeled; it was expected that a never-realized final round of design and fabrication would have been required to "tune" the current sensors to the correct full scale range (it would be desired that the current sensors hit the mechanical stops at a current just higher than the maximum phase current). However, it is also possible that the fabricated current sensors could already have been within the desired range of responsivity and full scale range.

6.2 Decreasing Inertial Sensitivity

While the current sensor has been designed to minimize its sensitivity to inertial effects, it can still be affected strongly. Angular acceleration about the torsion spring axis will cause the parallel plates to widen or close, mimicking a change in magnetic field. Additionally, in the in-plane direction that is perpendicular with the torsion spring axis (the long direction of the magnet), the center of mass of the suspended structure does not align with the torsion spring axis, so linear accelerations in this direction will also apply a torque and change the output frequency of the device. This torque is given by

$$T = a \cdot V \cdot \rho \cdot d \tag{6.1}$$

where a is the acceleration in the same direction as the magnet's long direction, V is the volume of the magnet, ρ is the density of the magnet, and d is the distance between the magnet's center of mass and the torsion spring axis (as viewed from the magnet's long direction). As an example, assuming a density of 7400 kg/m^3 for NdFeB and a 1 g acceleration in the magnet's long direction, a torque of 1.01×10^{-8} $N \cdot m$ will be produced about the torsion spring axis of the final current sensor design. This may sound small, but it is about 60% of the torque produced by a 1 A current (assuming that one amp of current produces 41 A/m of out-of-plane H-field as discussed in Chapter 5). This may not be a problem in a stationary DC POL voltage converter, as to the microcontroller monitoring the phases of the converter, this torque just represents a DC offset that can be automatically calibrated away by observing the output frequency of the current sensor when zero output is commanded on the phase. However, for any environment where significant inertial vibrations are expected up to a few hundred Hz, this sensitivity to acceleration and angular acceleration may be unacceptable.

In order to remove this sensitivity to inertial forces, the system shown in Figure 6.1 is proposed. In this design, two identical torsionally-suspended silicon structures are fabricated

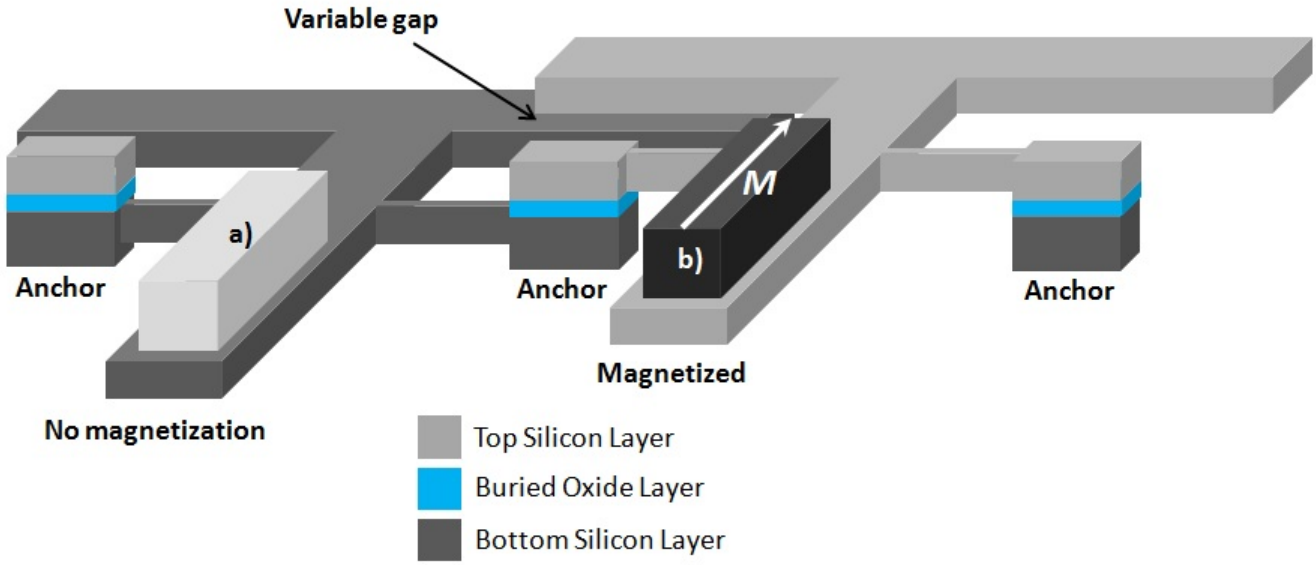

Figure 6.1: Conceptual design for a current sensor/magnetometer insensitive to inertial forces. Two equal masses are attached to two identical torsionally-suspended silicon structures. Mass a) is not magnetized while mass b) is.

on an SOI (silicon-on-insulator) wafer. One structure is fabricated on the top (device) layer while one is fabricated on the bottom (handle) layer. Part of the each structure's large moving plate overlaps the plate of the other, and the gap between them is set by the thickness of the buried oxide layer, which is etched away through release holes in each structure's moving plate (not shown). Attached to each of the suspended structures would be a mass that counter-balances the weight of the plate. Each mass would have the same location of its center of gravity (with respect to the structure it's attached to), but only one of the masses would be magnetized, as shown in Figure 6.1. When this device is subjected to inertial motions, both torsionally-suspended structures respond equally and the gap between the overlapping moving plates does not change. However, when the device is subjected to an out-of-plane external magnetic field, a torque is exerted only on the structure with the magnetized mass, which causes the gap between the two overlapping moving plates to narrow or widen. The gap between the overlapping suspended plates is sensed by measuring the capacitance between the two structures.

The proposed system has a few drawbacks, however. To keep parasitic capacitance low, care would have to be taken to minimize the area where the top silicon layer is attached to the bottom layer through the oxide. Additionally, the system would probably need to be damped strongly to prevent harmonic motion from being induced on each suspended structure, as there is nothing to necessarily prevent the devices from vibrating out-of-phase with each other (which would cause a sinusoidally-varying change in gap distance). Finally, fabrication may prove challenging, as the two torsion springs must have almost exactly the same spring constant. As detailed in Chapter 5, a wide variability in fabricated current sensor behavior was noticed, so obtaining nearly exactly-matched spring constants could prove very difficult.

6.3 Tilt-Mirror

Another potential use for torsionally suspended, magnetically actuated devices such as these is as a current-actuated tilt micro-mirror. The test results given earlier for the first prototype current sensor (Figure 2.5) demonstrate the viability of this idea, as the actuated angle was used to gauge the device's sensitivity to the applied current. Magnetic actuation for micro-mirrors has been studied before [39,52–54], as magnetic actuation allows relatively large forces and low voltages as compared to electrostatic actuation (while requiring larger power). The application of this work towards current-controlled micro-mirrors has been presented in [55], and future work could focus on developing a specialized, torsionally-suspended micro-mirror from this work.

Bibliography

[1] W. Zhang, Y. Long, Z. Zhang, F. Wang, L. Tolbert, B. Blalock, S. Henning, C. Wilson, and R. Dean, "Evaluation and comparison of silicon and gallium nitride power transistors in LLC resonant converter," in *2012 IEEE Energy Conversion Congress and Exposition (ECCE)*, Sep. 2012, pp. 1362–1366.

[2] C. Wilson, J. Hung, and R. Dean, "A sliding mode controller for two-phase synchronous buck converters," in *IECON 2012 - 38th Annual Conference on IEEE Industrial Electronics Society*, Oct. 2012, pp. 2150–2155.

[3] W. Zhang, Y. Long, Y. Cui, F. Wang, L. Tolbert, B. Blalock, S. Henning, J. Moses, and R. Dean, "Impact of planar transformer winding capacitance on Si-based and GaN-based LLC resonant converter," in *2013 Twenty-Eighth Annual IEEE Applied Power Electronics Conference and Exposition (APEC)*, Mar. 2013, pp. 1668–1674.

[4] W. Abell, J. Aggas, L. Jenkins, C. Wilson, and R. Dean, "The change in on-resistance in GaN HEMTs operating in a buck configuration," in *2013 IEEE Workshop on Wide Bandgap Power Devices and Applications (WiPDA)*, Oct. 2013, pp. 166–169.

[5] J. Aggas, L. Jenkins, C. Wilson, J. Moses, W. Abell, B. Rhea, and R. Dean, "A cross batch characterization of GaN HEMT devices for power electronics applications," in *2013 IEEE Workshop on Wide Bandgap Power Devices and Applications (WiPDA)*, Oct. 2013, pp. 170–173.

[6] L. Jenkins, C. Wilson, J. Moses, J. Aggas, and R. Dean, "A reliable and cost-effective assembly process for quick prototyping with GaN FETs and other flip-chip packages," in *2013 IEEE Workshop on Wide Bandgap Power Devices and Applications (WiPDA)*, Oct. 2013, pp. 84–87.

[7] L. Jenkins, C. Wilson, J. Moses, J. Aggas, B. Rhea, and R. Dean, "The impact of parallel GaN HEMTs on efficiency of a 12-to-1 V buck converter," in *2013 IEEE Workshop on Wide Bandgap Power Devices and Applications (WiPDA)*, Oct. 2013, pp. 197–200.

[8] B. Rhea, C. Wilson, L. Jenkins, and R. Dean, "The impact of inductor selection on a 12-1 V GaN POL converter with over 94% peak efficiency and higher load optimization," in *2013 IEEE Workshop on Wide Bandgap Power Devices and Applications (WiPDA)*, Oct. 2013, pp. 28–31.

[9] C. Wilson, L. Jenkins, J. Moses, J. Aggas, and R. Dean, "Hard switching speed improvements in GaN-based synchronous buck converters," in *2013 IEEE Workshop on Wide Bandgap Power Devices and Applications (WiPDA)*, Oct. 2013, pp. 194–196.

[10] Y. Cui, F. Xu, W. Zhang, B. Guo, L. Tolbert, F. Wang, B. Blalock, L. Jenkins, C. Wilson, J. Aggas, B. Rhea, J. Moses, and R. Dean, "High efficiency data center power supply using wide band gap power devices," in *2014 Twenty-Ninth Annual IEEE Applied Power Electronics Conference and Exposition (APEC)*, Mar. 2014, pp. 3437–3442.

[11] L. Jenkins, C. Wilson, J. Moses, J. Aggas, B. Rhea, and R. Dean, "Optimization of a 96% efficient 12 #x2013;1 V Gallium Nitride based point of load converter," in *2014 Twenty-Ninth Annual IEEE Applied Power Electronics Conference and Exposition (APEC)*, Mar. 2014, pp. 2098–2104.

[12] L. Jenkins, B. Rhea, W. Abell, F. Werner, C. Wilson, R. Dean, and D. Harris, "125 W multiphase GaN/Si hybrid point of load converter for improved high load efficiency," in *2014 IEEE Workshop on Wide Bandgap Power Devices and Applications (WiPDA)*, Oct. 2014, pp. 127–132.

[13] B. Rhea, L. Jenkins, W. Abell, F. Werner, C. Wilson, R. Dean, and D. Harris, "A 12 to 1 V five phase interleaving GaN POL converter for high current low voltage applications," in *2014 IEEE Workshop on Wide Bandgap Power Devices and Applications (WiPDA)*, Oct. 2014, pp. 155–158.

[14] L. Jenkins, J. Aggas, B. Rhea, W. Abell, C. Wilson, and R. Dean, "Design and implementation of planar inductors for low voltage GaN-based power converters," in *2015 IEEE Applied Power Electronics Conference and Exposition (APEC)*, Mar. 2015, pp. 1381–1387.

[15] H. Forghani-zadeh and G. Rincon-Mora, "Current-sensing techniques for DC-DC converters," in *The 2002 45th Midwest Symposium on Circuits and Systems, 2002. MWSCAS-2002*, vol. 2, Aug. 2002, pp. II–577–II–580 vol.2.

[16] S. Ziegler, R. C. Woodward, H. H.-C. Iu, and L. J. Borle, "Current Sensing Techniques: A Review," *IEEE Sensors Journal*, vol. 9, no. 4, pp. 354–376, Apr. 2009. [Online]. Available: http://ieeexplore.ieee.org/lpdocs/epic03/wrapper.htm?arnumber=4797906

[17] E. Dallago, M. Passoni, and G. Sassone, "Lossless current sensing in low-voltage high-current DC/DC modular supplies," *IEEE Transactions on Industrial Electronics*, vol. 47, no. 6, pp. 1249–1252, Dec. 2000.

[18] F. Semiconductor and R. Lenk, "Application Bulletin AB-20: Optimum Current Sensing Techniques in CPU Converters," Jan. 1999.

[19] Melexis, "MLX91205 IMC-Hall Current Sensor (Triaxis Technology)," Jun. 2013.

[20] S. Yuvarajan and L. Wang, "Power conversion and control using a current sensing power MOSFET," in *34th Midwest Symposium on Circuits and Systems*, vol. 1. Monterey, CA: IEEE, May 1991, pp. 166–169.

[21] ——, "Performance analysis and signal processing in a current sensing power MOSFET (SENSEFET)," in *Conference Record of the 1991 IEEE*, vol. 2, 1991, pp. 1445–1450.

[22] D. Niarchos, "Magnetic MEMS: key issues and some applications," *Sensors and Actuators A: Physical*, vol. 109, no. 12, pp. 166–173, Dec. 2003. [Online]. Available: http://www.sciencedirect.com/science/article/pii/S0924424703004400

[23] B. Vikramaditya, B. J. Nelson, G. Yang, and E. T. Enikov, "Microassembly of hybrid magnetic MEMS," *Journal of Micromechatronics*, vol. 1, no. 2, pp. 99–116, 2001.

[24] A. L. Herrera-May, P. J. Garca-Ramrez, L. A. Aguilera-Corts, J. Martnez-Castillo, A. Sauceda-Carvajal, L. Garca-Gonzlez, and E. Figueras-Costa, "A resonant magnetic field microsensor with high quality factor at atmospheric pressure," *Journal of Micromechanics and Microengineering*, vol. 19, no. 1, p. 015016, Jan. 2009. [Online]. Available: http://iopscience.iop.org/0960-1317/19/1/015016

[25] G. Du and X. Chen, "MEMS magnetometer based on magnetorheological elastomer," *Measurement*, vol. 45, no. 1, pp. 54–58, Jan. 2012. [Online]. Available: http://www.sciencedirect.com/science/article/pii/S0263224111003484

[26] H. H. Yang, N. V. Myung, J. Yee, D. Y. Park, B. Y. Yoo, M. Schwartz, K. Nobe, and J. W. Judy, "Ferromagnetic micromechanical magnetometer," *Sensors and Actuators A: Physical*, vol. 9798, pp. 88–97, Apr. 2002. [Online]. Available: http://www.sciencedirect.com/science/article/pii/S0924424701008093

[27] N. Wang and D. P. Arnold, "Fully batch-fabricated MEMS magnetic vibrational energy harvesters," *Proc. Power-MEMS*, pp. 348–351, 2009.

[28] S. P. Beeby, R. N. Torah, M. J. Tudor, P. Glynne-Jones, T. O'Donnell, C. R. Saha, and S. Roy, "A micro electromagnetic generator for vibration energy harvesting," *Journal of Micromechanics and Microengineering*, vol. 17, no. 7, p. 1257, Jul. 2007. [Online]. Available: http://iopscience.iop.org/0960-1317/17/7/007

[29] S. Guan, B. J. Nelson, and K. Vollmers, "Electrochemical Codeposition of Magnetic Particle-Ferromagnetic Matrix Composites for Magnetic MEMS Actuator Applications," *Journal of The Electrochemical Society*, vol. 151, no. 9, pp. C545–C549, Sep. 2004. [Online]. Available: http://jes.ecsdl.org/content/151/9/C545

[30] Y. Jiang, S. Masaoka, T. Fujita, M. Uehara, T. Toyonaga, K. Fujii, K. Higuchi, and K. Maenaka, "Fabrication of a vibration-driven electromagnetic energy harvester with integrated NdFeB/Ta multilayered micro-magnets," *Journal of Micromechanics and Microengineering*, vol. 21, no. 9, p. 095014, Sep. 2011. [Online]. Available: http://iopscience.iop.org/0960-1317/21/9/095014

[31] N. Dempsey, A. Walther, F. May, D. Givord, K. Khlopkov, and O. Gutfleisch, "High performance hard magnetic NdFeB thick films for integration into micro-electro-mechanical systems," *Applied Physics Letters*, vol. 90, no. 9, pp. 092 509–092 509–3, Feb. 2007.

[32] L. Lagorce, O. Brand, and M. Allen, "Magnetic microactuators based on polymer magnets," *Journal of Microelectromechanical Systems*, vol. 8, no. 1, pp. 2–9, Mar. 1999.

[33] S. Guan and B. J. Nelson, "Fabrication of hard magnetic microarrays by electroless codeposition for MEMS actuators," *Sensors and Actuators A: Physical*, vol. 118, no. 2, pp. 307–312, Feb. 2005. [Online]. Available: http://www.sciencedirect.com/science/article/pii/S0924424704006387

[34] B. Y. Yoo, S. C. Hernandez, D. Y. Park, and N. V. Myung, "Electrodeposition of FeCoNi thin films for magnetic-MEMS devices," *Electrochimica Acta*, vol. 51, no. 28, pp. 6346–6352, Sep. 2006. [Online]. Available: http://www.sciencedirect.com/science/article/pii/S001346860600483X

[35] L. Vieux-Rochaz, C. Dieppedale, B. Desloges, D. Gamet, C. Barragatti, H. Rostaing, and J. Meunier-Carus, "Electrodeposition of hard magnetic CoPtP material and integration into magnetic MEMS," *Journal of Micromechanics and Microengineering*, vol. 16, no. 2, p. 219, Feb. 2006. [Online]. Available: http://iopscience.iop.org/0960-1317/16/2/005

[36] S. Guan and B. J. Nelson, "Electrodeposition of low residual stress CoNiMnP hard magnetic thin films for magnetic MEMS actuators," *Journal of Magnetism and Magnetic Materials*, vol. 292, pp. 49–58, Apr. 2005. [Online]. Available: http://www.sciencedirect.com/science/article/pii/S0304885304011849

[37] Y. Sverdlov, Y. Rosenberg, Y. I. Rozenberg, R. Zmood, R. Erlich, S. Natan, and Y. Shacham-Diamand, "The electrodeposition of cobaltnickeliron high aspect ratio thick film structures for magnetic MEMS applications," *Microelectronic Engineering*, vol. 76, no. 14, pp. 258–265, Oct. 2004. [Online]. Available: http://www.sciencedirect.com/science/article/pii/S0167931704003880

[38] N. Wang and D. Arnold, "Thick Electroplated Co-Rich Co-Pt Micromagnet Arrays for Magnetic MEMS," *IEEE Transactions on Magnetics*, vol. 44, no. 11, pp. 3969–3972, Nov. 2008.

[39] J. Judy and R. Muller, "Magnetically actuated, addressable microstructures," *Journal of Microelectromechanical Systems*, vol. 6, no. 3, pp. 249–256, Sep. 1997.

[40] H. Jansen, M. d. Boer, R. Legtenberg, and M. Elwenspoek, "The black silicon method: a universal method for determining the parameter setting of a fluorine-based reactive ion etcher in deep silicon trench etching with profile control," *Journal of Micromechanics and Microengineering*, vol. 5, no. 2, p. 115, Jun. 1995. [Online]. Available: http://iopscience.iop.org/0960-1317/5/2/015

[41] E. Gogolides, V. Constantoudis, G. Kokkoris, D. Kontziampasis, K. Tsougeni, G. Boulousis, M. Vlachopoulou, and A. Tserepi, "Controlling roughness: from etching to nanotexturing and plasma-directed organization on organic and inorganic materials," *Journal of Physics D: Applied Physics*, vol. 44, no. 17, p. 174021, May 2011. [Online]. Available: http://iopscience.iop.org/0022-3727/44/17/174021

[42] J. S. Yoo, I. O. Parm, U. Gangopadhyay, K. Kim, S. K. Dhungel, D. Mangalaraj, and J. Yi, "Black silicon layer formation for application in solar cells," *Solar Energy*

Materials and Solar Cells, vol. 90, no. 1819, pp. 3085–3093, Nov. 2006. [Online]. Available: http://www.sciencedirect.com/science/article/pii/S0927024806002212

[43] J. Oh, H.-C. Yuan, and H. M. Branz, "An 18.2%-efficient black-silicon solar cell achieved through control of carrier recombination in nanostructures," *Nature Nanotechnology*, vol. 7, no. 11, pp. 743–748, Nov. 2012. [Online]. Available: http://www.nature.com.spot.lib.auburn.edu/nnano/journal/v7/n11/full/nnano.2012.166.html

[44] S. J. Cho, T. An, J. Y. Kim, J. Sung, and G. Lim, "Superhydrophobic nanostructured silicon surfaces with controllable broadband reflectance," *Chemical Communications*, vol. 47, no. 21, pp. 6108–6110, May 2011.

[45] Y. He, C. Jiang, H. Yin, J. Chen, and W. Yuan, "Superhydrophobic silicon surfaces with micronano hierarchical structures via deep reactive ion etching and galvanic etching," *Journal of Colloid & Interface Science*, vol. 364, no. 1, pp. 219–229, Dec. 2011.

[46] S.-S. Tan, H. Han, R. Boudreau, and M. Reed, "Process induced hillock defects on anisotropically etched silicon," in *IEEE Workshop on Micro Electro Mechanical Systems, 1994, MEMS '94, Proceedings*, 1994, pp. 229–234.

[47] H. Schrder, E. Obermeier, and A. Steckenborn, "Micropyramidal hillocks on KOH etched {100} silicon surfaces: formation, prevention and removal," *Journal of Micromechanics and Microengineering*, vol. 9, no. 2, p. 139, Jun. 1999. [Online]. Available: http://iopscience.iop.org/0960-1317/9/2/309

[48] Y. Fan, P. Han, P. Liang, Y. Xing, Z. Ye, and S. Hu, "Differences in etching characteristics of TMAH and KOH on preparing inverted pyramids for silicon solar cells," *Applied Surface Science*, vol. 264, pp. 761–766, Jan. 2013. [Online]. Available: http://www.sciencedirect.com/science/article/pii/S0169433212018582

[49] J. J. Wortman and R. A. Evans, "Young's Modulus, Shear Modulus, and Poisson's Ratio in Silicon and Germanium," *Journal of Applied Physics*, vol. 36, no. 1, pp. 153–156, Jan. 1965. [Online]. Available: http://scitation.aip.org/content/aip/journal/jap/36/1/10.1063/1.1713863

[50] F. Semiconductor, "Xtrinsic MAG3110 Three-Axis, Digital Magnetometer," Feb. 2013.

[51] STMicroelectronics, "LIS3mdl, Digital output magnetic sensor: ultra-low-power, high-performance 3-axis magnetometer," Jan. 2015.

[52] C.-H. Ji, Y. Yee, J. Choi, S.-H. Kim, and J.-U. Bu, "Electromagnetic 2 times;2 MEMS optical switch," *IEEE Journal of Selected Topics in Quantum Electronics*, vol. 10, no. 3, pp. 545–550, May 2004.

[53] C. Ji, Y. Yee, J. Choi, H. Oh, and J.-U. Bu, "Latchable electromagnetic 2 times;2 MEMS optical switch," in *IEEE The Sixteenth Annual International Conference on Micro Electro Mechanical Systems, 2003. MEMS-03 Kyoto*, Jan. 2003, pp. 239–242.

[54] I.-J. Cho, K.-S. Yun, H.-K. Lee, J.-B. Yoon, and E. Yoon, "A low-voltage two-axis electromagnetically actuated micromirror with bulk silicon mirror plates and torsion bars," in *The Fifteenth IEEE International Conference on Micro Electro Mechanical Systems, 2002*, Jan. 2002, pp. 540–543.

[55] R. N. Dean, C. B. Stevens, and J. J. Tatarchuk, "A current-controlled PCB integrated MEMS tilt mirror," in *Proceedings of the IMAPS 46th International Symposium on Microelectronics*, Orlando, FL, Oct. 2013, pp. 700–704.

Appendices

Appendix A

Silicon Microfabrication Recipe for Current Sensor MEMS Components

The following contains the process steps used to fabricate the silicon MEMS devices. Note that a hard mask of oxide is retained during DRIE etching to help maintain the width of the torsion springs (this step was never done during any of the actual fabrication batches, it was only later that it was realized that a hard mask was absolutely necessary).

Starting material: silicon wafers, 100 mm diameter, $\langle 100 \rangle$ orientation, 225-275 µm thick, p-type (resistivity 1-10 Ω-cm), double-side polished. A lower resistivity/higher doping can be used if desired (in fact, it is recommended).

Process flow:

1. Clean Wafer

   (a) Degrease wafer: Wash in acetone, followed by methanol, followed by a DI water rinse (X2). Finish cleaning in spin-rinse dryer, (rinse for 100 s, dry for 120 s)

   (b) Piranha etch: Submerse wafer in concentrated sulfuric acid. Slowly (over about a minute) add hydrogen peroxide until steam is rising from the solution or the sulfuric acid:hydrogen peroxide ratio is about 3:1. Let wafer sit for 30 minutes in mixture. More hydrogen peroxide can be added to restart the reaction if needed.

2. Oxidation

   (a) Set oxidation oven for a 1 hour wet oxidation at 1050 °C; insert the wafer(s) (it is probably a good idea to oxidize several wafers simultaneously) when the oven is below 600 °C

   (b) When oven is back below 600 °C, slowly remove the wafer(s).

3. Backside Patterning (there should now be about 0.5 µm - 1 µm of oxide on the wafer).

   (a) Degrease wafer (skip this step if the wafer has just come out of the oxidation oven): Wash in acetone, followed by methanol, followed by a DI water rinse (X2). Finish cleaning in spin-rinse dryer, (rinse for 100 s, dry for 180 s).

   (b) Dehydrobake (skip this step if the wafer has just come out of the oxidation oven): Bake wafer at 120 °C for 15 minutes.

   (c) HMDS: Put 8-12 drops of HMDS into bell jar, insert wafer, close bell jar, and let sit for 5 minutes (HMDS promotes photoresist adhesion).

   (d) Frontside photoresist: Spin on AZ4620 photoresist on one side of wafer (make sure to keep opposite side of wafer clean!); spin for 45 seconds at 3500 RPM. Bake photoresist for 5 minutes at 105 °C.

   (e) HMDS: Let wafer cool, then put 8-12 drops of HMDS into bell jar, insert wafer, close bell jar, and let sit for 5 minutes.

   (f) Backside photoresist: Spin on AZ4620 photoresist on the other side of the wafer; spin for 45 seconds at 3500 RPM. Bake photoresist for 5 minutes at 105 °C.

   (g) Backside patterning: Load the backside mask into the mask aligner, roughly align the wafer to the mask, and expose photoresist; 5 cycles of 6 second exposures each (30 seconds total) is probably good for the thick AZ4620 photoresist.

   (h) Develop: Develop pattern in a 3:1 mixture of DI water:AZ400K developer (150 mL DI water, 50 mL AZ400K) for about 3 minutes. Rinse and dry wafer in the spin-rinse dryer (100 s rinse, 180 s dry) or by hand. Inspect pattern to ensure that no photoresist remains in backside exposed areas.

   (i) Etch oxide: Insert wafer into buffered oxide etch (BOE) bath until backside exposed areas have been COMPLETELY stripped of oxide (this might take up to 10 minutes, BOE etches oxide at about 100 nm/min). Do not be afraid of over-etching, it is not possible on this step.

(j) Strip PR: Wash in acetone, followed by methanol, followed by a DI water rinse (X3). Finish cleaning in spin-rinse dryer, (rinse for 100 s, dry for 120 s).

4. KOH Etch (there should now be patterned oxide on one side (the backside) and unpatterned oxide on the other).

   (a) Prepare KOH solution: Heat a solution of 30% KOH to approximately 60 °C

   (b) Etch silicon: Submerse wafer in KOH solution. After about a minute, remove the wafer and measure the etch depth with the profilometer to establish the etch rate. Return wafer to solution and continue etching and checking depth until the desired backside etch depth is reached (typically 5 µm - 15 µm.

   (c) Rinse wafer: Rinse and dry wafer in the spin-rinse dryer (100 s rinse, 180 s dry)

5. Frontside Patterning (the wafer should now have unpatterned oxide on the frontside, and a patterned oxide on the backside, with the exposed silicon etched down 5 µm - 15 µm).

   (a) Degrease wafer (skip this step if the wafer has just come out of the KOH solution): Wash in acetone, followed by methanol, followed by a DI water rinse (X2). Finish cleaning in spin-rinse dryer, (rinse for 100 s, dry for 180 s).

   (b) Dehydrobake: Bake wafer at 120 °C for 15 minutes.

   (c) HMDS: Put 8-12 drops of HMDS into bell jar, insert wafer, close bell jar, and let sit for 5 minutes (HMDS promotes photoresist adhesion).

   (d) Frontside photoresist: Spin on AZ4620 photoresist on the unpatterned frontside; spin for 45 seconds at 3500 RPM. Bake photoresist for 5 minutes at 105 °C.

   (e) Frontside patterning: Load the frontside mask (the one that defines the torsion springs) into the mask aligner. Align the frontside mask alignment marks to the backside alignment marks. Expose photoresist; 5 cycles of 6 second exposures (for a total of 30 seconds) is probably good for thick AZ 4620 photoresist.

(f) Develop: Develop pattern in a 3:1 mixture of DI water:AZ400K developer (150 mL DI water, 50 mL AZ400K) for about 2.5 minutes. Rinse and dry wafer in the spin-rinse dryer (100 s rinse, 180 s dry) or by hand. Inspect pattern to ensure that no photoresist remains in the frontside exposed areas, and that the pattern transferred correctly to the photoresist.

(g) Etch oxide: Insert wafer into buffered oxide etch (BOE) bath until the frontside exposed areas have been completely stripped of oxide. BOE etches oxide at about 100 nm/min. The exposed backside oxide can be used to help determine when the front oxide is gone; the backside should become hydrophobic after all the oxide is gone. Once this is observed, etch the wafer just a little longer to be certain that all oxide areas are gone. It is difficult to over-etch the oxide as the rate that the pattern is undercut (100 nm/min) is very slow compared to the pattern width (30 µm).

(h) Rinse wafer: Rinse and dry wafer in the spin-rinse dryer (100 s rinse, 180 s dry).

6. Backing Wafer (the wafer should now have patterned oxide on the frontside defining the torsion springs and moving platform outline, and bare, patterned silicon on the backside, with the pattern defined by the µm - 15 µm backside KOH step done previously).

(a) Degrease backing wafer: Wash a separate BACKING WAFER in acetone, followed by methanol, followed by a DI water rinse (X2). Finish cleaning in spin-rinse dryer, (rinse for 100 s, dry for 180 s).

(b) Dehydrobake: Bake backing wafer at 120 °C for 15 minutes.

(c) HMDS: Put 8-12 drops of HMDS into bell jar, insert wafer, close bell jar, and let sit for 5 minutes (HMDS promotes photoresist adhesion).

(d) "Glue" device wafer onto backing wafer with photoresist: Spin AZ5214 photoresist onto backing wafer (1500 RPM for 10 seconds is good). Quickly, before the

photoresist can dry, place the device wafer down on the backing wafer BACKSIDE DOWN (so that the patterned side is facing up). Bake the wafer stack at 105 °C for at least 10 minutes. An overnight soft-bake at 80 °C - 90 °C can help.

7. DRIE Etch (no additional process steps were done to the wafer, is now just attached to a backing wafer for mechanical support during the upcoming DRIE step).

   (a) Blow wafer: Prior to every time the wafer is inserted into the DRIE etch machine, it is advisable to blow the wafer with nitrogen to help remove any contaminants (unless the devices are beginning to separate).

   (b) Etch wafer: Insert the wafer into the DRIE etch machine. Use recipe "Morgan-SOI" (it uses an etch time of 13 seconds and a passivation time of 7 seconds). The DRIE etch machine etches silicon at approximately 1 µm/cycle (with each cycle lasting 13 + 7 = 20 seconds); do a short etch of 20-50 cycles and measure the etch depth to determine the exact etch rate. Continue etching until the device wafer has been etched all the way through. It may be necessary to remove some devices that finish before others. Be careful not to over-etch! As the torsion springs are less thick than the bulk wafer by the backside etch depth, the torsion springs will etch through first. It is not strictly necessary to keep etching until the devices become completely loose, doing so could over-etch the springs. The last bit of silicon attaching the devices to each other can be broken easily.

8. Clean Devices (the devices are now finished with silicon microfabrication and are sitting on the backing wafer).

   (a) Separate from backing wafer: Soak devices and backing wafer in acetone until the devices become loose from the backing wafer.

   (b) Clean devices in acetone: Let the devices soak in acetone for 15 minutes to an hour.

(c) Piranha etch: Pick the devices out of the acetone, wash quickly in water (acetone reacts violently with sulfuric acid), then place the devices in concentrated sulfuric acid. Once all the devices are in the sulfuric acid, slowly (over a minute or so) add hydrogen peroxide until steam is rising from the solution or the sulfuric acid:hydrogen peroxide ratio is about 3:1. More hydrogen peroxide can be added to restart the reaction if needed. Let the devices sit in the solution for 30-45 min.

(d) Inspect devices: If the devices are not completely clean, then repeat the piranha etch.

(e) Return to acetone: Remove the devices from the piranha etch mixture using an acid-resistant set of tweezers. Wash the devices quickly in water before placing them back in a new acetone bath.

(f) Prepare hotplate: Place a clean sheet of aluminum foil over a hotplate and set the hotplate to a high temperature (the hot plates in the lab do not have an accurate temperature gauge...).

(g) Exchange acetone with methanol: Using pipettes, begin removing the acetone from the dish/pan the devices are in. Once almost all the acetone is gone, fill the dish with methanol. Now, remove the methanol with pipettes. Once almost all the methanol is gone, refill the dish with methanol.

(h) Dry devices: Using a pair of metal tweezers, remove the devices one-by-one from the methanol and hold them on the hot plate surface. The methanol will quickly boil away and (hopefully!) leave behind a streak-free silicon surface. Once all the methanol is gone, let each device cool before placing it into a clean petri dish.

Appendix B

MATLAB Script for Predicting Current Sensor Behavior

```
%M file for calculating MEMS current sensor characteristics
'New calculations follow...'
clear all
%Permanent magnet size
mag_l = 1500e-6;
mag_w = 500e-6;
mag_h = 500e-6;

mag_dens = 7400; %NdFeB density
si_dens = 2330; %Silicon density

%Permanent magnet Br
Br = 1.1; %T

%External magnetic field, A/m per A
Hext = 41; %A/m

%Current
I = 1; %A

%Torsion spring characteristics
TS_l = 1475e-6;
TS_w = 30e-6;
```

```
TS_h = 242e-6;

%Moving electrode characteristics
ME_l = 1530e-6;
ME_w = 3450e-6;
ME_gap = 8e-6; %Nominal gap
ME_da = 120e-6; %The distance from the axis of rotation to the edge of the moving
    electrode

%Silicon, Young's modulus-
E_Si = 150e9; %GPa

%Silicon, Poisson's ratio-
Nu_Si = 0.25;



%-------------------------------------------------------
%Calculations
%Magnet magnetic moment, verify-
m_m = Br*mag_l*mag_w*mag_h/(4*pi*1e-7);

%Torque, if external field out-of-plane-
T_m = m_m*Hext*I*4*pi*1e-7

w = TS_w;
t = TS_h;

Kbeam = ((w^3*t)/3)*(1 - (192/pi^5)*(w/t)*( (1/1^5)*tanh(1*pi*t/(2*w)) ))
%Silicon Shear Modulus of Elasticity
```

```
G_Si = E_Si/(2*(1 + Nu_Si))


Kphi = 2*Kbeam*G_Si/TS_l
%Angular Rotation of torsion spring-
%theta_TS = T_m*TS_l/(J_Pmi*G_Si);
theta_TS = T_m/Kphi


thetaDeg = theta_TS*360/(2*pi)


%Starting gap width (at beginning of platform)
cgs = sin(theta_TS)*ME_da
g_w1 = ME_gap - cgs;


%Final gap width (at end of platform)
cge = sin(theta_TS)*(ME_da + ME_l)
g_w2 = ME_gap - cge;


g_w2
'Change in gap distance:'
delta = sin(theta_TS)*(ME_da + ME_l) %Change in gap distance
if g_w2 < 0
    'Warning! Sensor bottomed out.'
else
    %Predicted initial capacitance-
    C_nom = 8.854e-12*ME_w*ME_l/ME_gap


    %Predicted new capacitance-
    Cnew = 8.854e-12*ME_w*ME_l*log(g_w2/g_w1)/(g_w1*(g_w2/g_w1 - 1))
```

```
    fnom = 0.455/(2e6*(C_nom + 2e-12))

    fnew = 0.455/(2e6*(Cnew + 2e-12))

    deltaF = fnew - fnom; %change in frequency of relaxation oscillator
    currentResponsivity = deltaF/I
    'Hz/A'
    fieldResponsivity = deltaF/(Hext*I*4*pi*1e-7) %In Hz/Tesla
    'Hz/T'
end

%---------------------------------
%Analysis of gravitational effect
Mm = mag_l*mag_w*mag_h*mag_dens; %mass of magnet

a = 9.81; %acceleration
Ta = a*Mm*(mag_h/2+TS_h/2) %Torque due to gravity
theta_grav = Ta/Kphi %rotataion due to gravity
theta_grav/theta_TS %rotataion due to gravity


%-------------------------------------
%Analysis of natural frequency

%Three rectangular prisms-
%Wide segment of silicon platform
SiR1_l = 1530e-6;
SiR1_h = 242e-6;
SiR1_d = 3450e-6;
```

```
SiR1_m = SiR1_l*SiR1_h*SiR1_d*si_dens;
SiR1_cenI = (1/12)*SiR1_m*(SiR1_l^2 + SiR1_h^2); %Centroid moment of inertia
SiR1_dist = 120e-6 + SiR1_l/2; %distance from centroid to axis of rotation
SiR1_I = SiR1_cenI + SiR1_m*SiR1_dist^2; %Parallel axis theorem

%Narrow segment of silicon platform
SiR2_l = 1770e-6;
SiR2_h = 242e-6;
SiR2_d = 700e-6;
SiR2_m = SiR2_l*SiR2_h*SiR2_d*si_dens;
SiR2_cenI = (1/12)*SiR2_m*(SiR2_l^2 + SiR2_h^2); %Centroid moment of inertia
SiR2_dist = SiR2_l/2 - 120e-6; %distance from centroid to axis of rotation
SiR2_I = SiR2_cenI + SiR2_m*SiR2_dist^2; %Parallel axis theorem

%NdFeB Magnet
MM_l = 1500e-6;
MM_h = 500e-6;
MM_d = 500e-6;
MM_m = MM_l*MM_h*MM_d*mag_dens;
MM_cenI = (1/12)*MM_m*(MM_l^2 + MM_h^2); %Centroid moment of inertia
MM_dist = ((MM_l/2)^2 + (MM_h/2 + SiR1_h/2)^2)^0.5; %distance from centroid to
    axis of rotation
MM_I = MM_cenI + MM_m*MM_dist^2; %Parallel axis theorem

tot_I = SiR1_I + SiR2_I + MM_I
f_nat = (Kphi/tot_I)^0.5/(2*pi)
```

Appendix C

Lua Script for Predicting H-field Produced From a Current Trace Geometry

```
--[[Uses Biot-Savart's law to compute magnetic field produced by current flowing
   through a trace.]]
--Define project:
-- Traces are defined from center end to center end. Current travels along long
   dimension.
--[[ for both traces and elbows: can use either points to define, or can use this
   :
 a line trace:
              [1] = {
                     type = 'line',
                     start = {x = 0.01, y = 0.01, z = 0},
                     stop = {x = 0.05, y = 0.01, z = 0},
                     width = 0.006,
              },


       an elbow trace:
              [3] = {
                     type = 'elbow',
                     start = {x = 0.05, y = 0.01, z = 0},
                     stop = {x = 0.053, y = 0.007, z = 0},
                     arc = math.pi/2 -- can be positive or negative
              }
```

```
]]
project = {
        traces = {
                [1] = { -- line 7.14mm long, 6 mm wide
                        type = 'line',
                        start = {x = 0, y = 0, z = 0},
                        stop = {x = 7.14e-3, y = 0, z = 0},
                        width = 6e-3,
                },

                [2] = { -- CW elbow on 6mm trace
                        type = 'elbow',
                        start = {x = 7.14e-3, y = 0e-3, z = 0},
                        stop = {x = 10.14e-3, y = -3e-3, z = 0},
                        arc = -math.pi/2
                },
                [3] = { -- line 500 um long, 6 mm wide
                        type = 'line',
                        start = {x = 10.14e-3, y = -3.00e-3, z = 0},
                        stop = {x = 10.14e-3, y = -3.5e-3, z = 0},
                        width = 6e-3,
                },
                [4] = { -- CCW elbow on 6mm trace
                        type = 'elbow',
                        start = {x = 10.14e-3, y = -3.5e-3, z = 0},
                        stop = {x = 13.14e-3, y = -6.5e-3, z = 0},
                        arc = math.pi/2
                },
                [5] = { -- line 7.25 mm long, 6 mm wide
```

```
        type = 'line',
        start = {x = 13.14e-3, y = -6.5e-3, z = 0},
        stop = {x = 20.39e-3, y = -6.5e-3, z = 0},
        width = 6e-3,
},
[6] = { -- CCW elbow on 6mm trace
        type = 'elbow',
        start = {x = 20.39e-3, y = -6.5e-3, z = 0},
        stop = {x = 23.39e-3, y = -3.5e-3, z = 0},
        arc = math.pi/2
},
[7] = { -- line 500 um long, 6 mm wide
        type = 'line',
        start = {x = 23.39e-3, y = -3.5e-3, z = 0},
        stop = {x = 23.39e-3, y = -3e-3, z = 0},
        width = 6e-3,
},
[8] = { -- CW elbow on 6mm trace
        type = 'elbow',
        start = {x = 23.39e-3, y = -3e-3, z = 0},
        stop = {x = 26.39e-3, y = 0e-3, z = 0},
        arc = -math.pi/2
},
[9] = { -- line 7.14 um long, 6 mm wide
        type = 'line',
        start = {x = 26.39e-3, y = 0e-3, z = 0},
        stop = {x = 33.53e-3, y = 0e-3, z = 0},
        width = 6e-3,
},
```

```
	},

	current = 1,

	obsPoints = {
		[1] = {x = 16.765e-3, y = -0.21e-3, z = 0.5e-3},
		[2] = {x = 16.765e-3, y = -0.71e-3, z = 0.5e-3},
		[3] = {x = 16.765e-3, y = -1.21e-3, z = 0.5e-3},
	},

	res = 1.2e-5, --

}




-----------------------------------------------------------------
function deepCopy(object)
	local lookup_table = {}
	local function _copy(object)
		if type(object) ~= "table" then
			return object
		elseif lookup_table[object] then
			return lookup_table[object]
		end
		local new_table = {}
```

```
                lookup_table[object] = new_table
                for index, value in pairs(object) do
                        new_table[_copy(index)] = _copy(value)
                end
                return setmetatable(new_table, getmetatable(object))
        end
        return _copy(object)
end

function pointInPolygon(point, poly) --raycasting point in polygon. Code adapted
    from http://softsurfer.com/Archive/algorithm_0103/algorithm_0103.htm
        local px = point.x
        local py = point.y
        local cn = 0
        local newpoly = deepCopy(poly)

        local polysize = #newpoly
        newpoly[#newpoly + 1] = newpoly[1]

        for k = 1, polysize do
                if ((newpoly[k].y <= py) and (newpoly[k+1].y > py)) or ((newpoly[k
                    ].y > py) and (newpoly[k+1].y <= py)) then
                        local vt = (py - newpoly[k].y) / (newpoly[k+1].y - newpoly[k
                            ].y)
                        if (px < newpoly[k].x + vt*(newpoly[k+1].x - newpoly[k].x))
                            then
                           cn = cn + 1
                        end
                end
```

```
        end

        return cn%2 == 1

end

-------------------------------------------------------------------------------------------

--3D Vector manipulation
vec = {}

vec.add = function(vec1, vec2)
        return {x = vec1.x + vec2.x, y = vec1.y + vec2.y, z = vec1.z + vec2.z}
end

vec.sub = function(vec1, vec2)
        return {x = vec1.x - vec2.x, y = vec1.y - vec2.y, z = vec1.z - vec2.z}
end

vec.scalarMult = function(vec, mult)
        return {x = vec.x*mult, y = vec.y*mult, z = vec.z*mult}
end

vec.dp = function(vec1, vec2)
        return vec1.x*vec2.x + vec1.y*vec2.y + vec1.z*vec2.z
end

vec.cp = function(vec1, vec2)
```

```
	return { x = vec1.y*vec2.z - vec1.z*vec2.y, y = vec1.z*vec2.x - vec1.x*
	    vec2.z, z = vec1.x*vec2.y - vec1.y*vec2.x}
end

vec.mag = function(vec)
	return (vec.x^2 + vec.y^2 + vec.z^2)^0.5
end

vec.getUnitVec = function(Vec)
	local mag = vec.mag(Vec)
	return { x = Vec.x/mag, y = Vec.y/mag, z = Vec.z/mag }
end

vec.rotateVec2 = function(vec2, theta)
	return { x = vec2.x*math.cos(theta) - vec2.y*math.sin(theta), y = vec2.x*
	    math.sin(theta) + vec2.y*math.cos(theta)}
end
-----------------------------------------------

do
	local currents = {}

	local function findLimits(points)
		local xmax, xmin, ymax, ymin = -math.huge, math.huge, -math.huge,
		    math.huge
		for ind, point in pairs(points) do
			if point.x > xmax then
				xmax = point.x
			end
```

```
                if point.x < xmin then
                        xmin = point.x
                end
                if point.y > ymax then
                        ymax = point.y
                end
                if point.y < ymin then
                        ymin = point.y
                end
        end
        return xmax, xmin, ymax, ymin
end

--Now, generate the current trace matrix
for ind, trace in pairs(project.traces) do

        local Js
        local dir = vec.getUnitVec(vec.sub(trace.stop, trace.start))
        if trace.width then
                Js = project.current/trace.width
        end

        local points = {}
        if trace.type == 'line' then
                if trace.points then
                        points = trace.points
                else
                        points = {
```

```
[1] = {
        x = trace.start.x + vec.rotateVec2(dir
            , math.pi/2).x*trace.width/2,
        y = trace.start.y + vec.rotateVec2(dir
            , math.pi/2).y*trace.width/2,
        z = trace.start.z
},

[2] = {
        x = trace.stop.x + vec.rotateVec2(dir,
             math.pi/2).x*trace.width/2,
        y = trace.stop.y + vec.rotateVec2(dir,
             math.pi/2).y*trace.width/2,
        z = trace.stop.z
},

[3] = {
        x = trace.stop.x + vec.rotateVec2(dir,
             -math.pi/2).x*trace.width/2,
        y = trace.stop.y + vec.rotateVec2(dir,
             -math.pi/2).y*trace.width/2,
        z = trace.stop.z
},

[4] = {
        x = trace.start.x + vec.rotateVec2(dir
            , -math.pi/2).x*trace.width/2,
        y = trace.start.y + vec.rotateVec2(dir
            , -math.pi/2).y*trace.width/2,
```

```
                        z = trace.start.z
                },


        }
    end
    print('line segment:')
    print('point 1: x = ' .. points[1].x .. ', y = ' .. points
        [1].y .. ', z = ' .. points[1].z)
    print('point 2: x = ' .. points[2].x .. ', y = ' .. points
        [2].y .. ', z = ' .. points[2].z)
    print('point 3: x = ' .. points[3].x .. ', y = ' .. points
        [3].y .. ', z = ' .. points[3].z)
    print('point 4: x = ' .. points[4].x .. ', y = ' .. points
        [4].y .. ', z = ' .. points[4].z)
    print('current density: ' .. Js)

elseif trace.type == 'elbow' then
    if trace.points then
        points = trace.points
    else


        local len = vec.mag(vec.sub(trace.stop, trace.start)
            )
        local hyp = math.abs(len/(math.sin(trace.arc/2)))
        local base = len*2
        local height = math.cos(trace.arc/2)*hyp
        Js = project.current/height


        local rot1 = (math.pi - math.abs(trace.arc))/2
```

```
local rot2 = math.pi - rot1


if trace.arc < 0 then
       rot1 = rot1*-1
end


if trace.arc > 0 then
       rot2 = rot2*-1
end


points[1] = {
       x = trace.start.x + vec.rotateVec2(dir, rot1)
           .x*hyp/2,
       y = trace.start.y + vec.rotateVec2(dir, rot1)
           .y*hyp/2,
       z = trace.start.z
}



points[2] = {
       x = trace.start.x + vec.rotateVec2(dir, rot2)
           .x*hyp/2,
       y = trace.start.y + vec.rotateVec2(dir, rot2)
           .y*hyp/2,
       z = trace.start.z
}


points[3] = {
       x = points[2].x + dir.x*base,
```

```
                    y = points[2].y + dir.y*base,
                    z = points[2].z + trace.start.z
                }
        end

        print('elbow joint:')
        print('point 1: x = ' .. points[1].x .. ', y = ' .. points
            [1].y .. ', z = ' .. points[1].z)
        print('point 2: x = ' .. points[2].x .. ', y = ' .. points
            [2].y .. ', z = ' .. points[2].z)
        print('point 3: x = ' .. points[3].x .. ', y = ' .. points
            [3].y .. ', z = ' .. points[3].z)
        print('current density: ' .. Js)
end

--Now, draw a box around each trace, do point in polygon

local xmax, xmin, ymax, ymin = findLimits(points)

local xSams = math.floor((xmax-xmin)/project.res) + 1
local ySams = math.floor((ymax-ymin)/project.res) + 1

local xp = xmin
local yp = ymin
-- build currents

print('Buiding currents for trace ' .. ind .. '...')
local elemCurrent = Js*project.res^2 -- total amount of current
    inside each element
```

```
        for xInd = 1, xSams do
                xp = xmin + xInd*project.res
                for yInd = 1, ySams do
                        yp = ymin + yInd*project.res

                        if pointInPolygon({x = xp, y = yp}, points) then --
                            add this current element.
                                --print('in here: xInd = ' .. xInd .. ' yInd
                                    = ' ..yInd)
                                currents[#currents + 1] = {
                                        loc = { x = xp, y = yp, z = points[1].
                                            z},
                                        cur = vec.scalarMult(dir, elemCurrent)
                                }

                        end

                end
        end
        print('currents for trace ' .. ind .. ' completed')
end

print('current building completed. ' .. #currents .. ' current elements.')

print('Computing H field at points....')

Hfields = {}
for obsInd = 1, #project.obsPoints do
        local hp = {x = 0, y = 0, z = 0}
```

```
            obsPoint = project.obsPoints[obsInd]

            for curInd = 1, #currents do
                local curEl = currents[curInd]

                local r = vec.sub(obsPoint, curEl.loc)
                local rU = vec.getUnitVec(r)

                local hEl = vec.scalarMult(vec.cp(curEl.cur, rU), 1/(4*math.
                    pi*(vec.mag(r)^2)))

                hp = vec.add(hp, hEl)
            end

            Hfields[obsInd] = hp

            print('Hfields[' .. obsInd .. '] = {x = ' .. hp.x .. ', y = ' .. hp
                .y .. ', z = ' .. hp.z .. '}')
            print('Magnitude: ' .. vec.mag(hp) .. '\n')
        end
end
```